

# NAVAL POSTGRADUATE SCHOOL MONTEREY, CALIFORNIA



## THESIS

**A COMPARISON OF FLIGHT INPUT  
TECHNIQUES FOR  
PARAMETER ESTIMATION OF  
HIGHLY-AUGMENTED AIRCRAFT**

by

Russell John Gates

September, 1995

Thesis Advisor:  
Co-Advisor:

D. J. Collins  
R.M. Howard

Approved for public release; distribution is unlimited.

19960305 107

DTIC QUALITY INSPECTED 1

# DISCLAIMER NOTICE



THIS DOCUMENT IS BEST  
QUALITY AVAILABLE. THE  
COPY FURNISHED TO DTIC  
CONTAINED A SIGNIFICANT  
NUMBER OF PAGES WHICH DO  
NOT REPRODUCE LEGIBLY.

## REPORT DOCUMENTATION PAGE

Form Approved OMB No. 0704-0188

Public reporting burden for this collection of information is estimated to average 1 hour per response, including the time for reviewing instruction, searching existing data sources, gathering and maintaining the data needed, and completing and reviewing the collection of information. Send comments regarding this burden estimate or any other aspect of this collection of information, including suggestions for reducing this burden, to Washington Headquarters Services, Directorate for Information Operations and Reports, 1215 Jefferson Davis Highway, Suite 1204, Arlington, VA 22202-4302, and to the Office of Management and Budget, Paperwork Reduction Project (0704-0188) Washington DC 20503.

1. AGENCY USE ONLY <i>(Leave blank)</i>			2. REPORT DATE 1995 September		3. REPORT TYPE AND DATES COVERED Master's Thesis		
4. TITLE AND SUBTITLE <b>A Comparison of Flight Input Techniques for Parameter Estimation of Highly-Augmented Aircraft</b>			5. FUNDING NUMBERS				
6. AUTHOR(S) Gates, Russell John							
7. PERFORMING ORGANIZATION NAME(S) AND ADDRESS(ES) Naval Postgraduate School Monterey CA 93943-5000			8. PERFORMING ORGANIZATION REPORT NUMBER				
9. SPONSORING/MONITORING AGENCY NAME(S) AND ADDRESS(ES)			10. SPONSORING/MONITORING AGENCY REPORT NUMBER				
11. SUPPLEMENTARY NOTES The views expressed in this thesis are those of the author and do not reflect the official policy or position of the Department of Defense or the U.S. Government.							
12a. DISTRIBUTION/AVAILABILITY STATEMENT Approved for public release; distribution is unlimited.				12b. DISTRIBUTION CODE			
13. ABSTRACT <i>(maximum 200 words)</i> Parameter estimation is an inverse process in which stability derivatives are determined from time history flight data by matching the aircraft mathematical model's computed response with the measured response of the aircraft. Accurate parameter estimation depends mainly on instrumentation and input technique. Input technique is the focus of this thesis in which both classical inputs and optimal inputs were applied under the same flight conditions to the High Angle of Attack Research Vehicle (HARV) at NASA Dryden Flight Research Center. Post flight parameter estimation was conducted in all cases using a maximum likelihood technique to determine estimated of stability and control derivatives and their respective Cramer-Rao bounds. The Cramer-Rao bound is the most useful measure of estimate accuracy when comparing results from different input techniques assuming the same mathematical model and minimization technique were used for the parameter estimates. Comparison of the Cramer-Rao bounds showed that of the four input techniques used for determining parameter estimates, the Dryden single-surface input technique yielded the most accurate parameters for 75 percent of the estimates in all cases. Application of these conclusions in further research can save time and costs.							
14. SUBJECT TERMS Parameter Estimation, Input Technique, Cramer-Rao Bound					15. NUMBER OF PAGES 118		
					16. PRICE CODE		
17. SECURITY CLASSIFICATION OF REPORT Unclassified		18. SECURITY CLASSIFICATION OF THIS PAGE Unclassified		19. SECURITY CLASSIFICATION OF ABSTRACT Unclassified		20. LIMITATION OF ABSTRACT UL	



Approved for public release; distribution is unlimited.

A COMPARISON OF FLIGHT INPUT TECHNIQUES FOR  
PARAMETER ESTIMATION OF  
HIGHLY-AUGMENTED AIRCRAFT

Russell J. Gates  
Lieutenant, United States Navy  
B.S.A.A.E., Purdue University, 1985

Submitted in partial fulfillment  
of the requirements for the degree of

MASTER OF SCIENCE IN AERONAUTICAL ENGINEERING  
from the  
NAVAL POSTGRADUATE SCHOOL  
September 1995

Author:

Russell J. Gates

Russell J. Gates

Approved by:

Daniel J. Collins

Daniel J. Collins, Thesis Advisor

Richard M. Howard

Richard M. Howard, Co-Advisor

Albion H. Bowers

Albion H. Bowers, Second Reader

Daniel J. Collins

Daniel J. Collins, Chairman

Department of Aeronautics and Astronautics



## ABSTRACT

Parameter estimation is an inverse process in which stability derivatives are determined from time history flight data by matching the aircraft mathematical model's computed response with the measured response of the aircraft. Accurate parameter estimation depends mainly on instrumentation and input technique. Input technique is the focus of this thesis in which both classical inputs and optimal inputs were applied under the same flight conditions to the High Angle of Attack Research Vehicle (HARV) at NASA Dryden Flight Research Center. Post flight parameter estimation was conducted in all cases using a maximum likelihood technique to determine estimated of stability and control derivatives and their respective Cramer-Rao bounds. The Cramer-Rao bound is the most useful measure of estimate accuracy when comparing results from different input techniques assuming the same mathematical model and minimization technique were used for the parameter estimates. Comparison of the Cramer-Rao bounds showed that of the four input techniques used for determining parameter estimates, the Dryden single-surface input technique yielded the most accurate parameters for 75 percent of the estimates in all cases. Application of these conclusions in further research can save time and costs.



## TABLE OF CONTENTS

I.	INTRODUCTION .....	1
A.	BACKGROUND .....	1
B.	PURPOSE .....	4
II.	MAXIMUM LIKELIHOOD ESTIMATOR .....	5
A.	PARAMETER ESTIMATION PROGRAM (pEst) .....	6
B.	MATHEMATICAL MODEL .....	8
1.	Control Surfaces Used in the Model .....	8
2.	Convergence Criteria .....	11
3.	Output Weightings .....	12
4.	A Priori Information .....	13
C.	MINIMIZATION TECHNIQUE .....	13
D.	MEASURES OF ACCURACY .....	15
1.	Insensitivity .....	15
2.	Cramer-Rao Bound .....	16
E.	CORRELATION .....	18
III.	INPUT TECHNIQUES .....	23
A.	SINE WAVES .....	23
B.	DOUBLETS .....	24
C.	DRYDEN SINGLE-SURFACE INPUTS (SSI/OBES) .....	25
D.	OPTIMAL INPUTS .....	28
1.	Klein Targeted Optimal Input Maneuvers .....	29
2.	Morelli Optimal Input Maneuvers .....	31
E.	3211 DOUBLETS .....	33
IV.	COMPUTER ANALYSIS SOFTWARE .....	35
A.	FLIGHT TEST DATA .....	35
1.	GetFdas .....	35
2.	GetData .....	35
B.	pEst .....	36
C.	UTILITY PLOTTING PROGRAM (XPlot) .....	37

D. CRAMER RAO COMPARISONS .....	38
E. CORRELATION MATRIX .....	39
V. RESULTS AND DISCUSSION .....	41
A. LONGITUDINAL PARAMETERS .....	42
1. X-Force (axial) .....	43
a. Results for 20 and 25 Degrees Angle of Attack .....	43
b. Results for 30 Degrees Angle of Attack .....	46
2. Z-Force (normal) .....	48
a. Results for 20 and 25 Degrees Angle of Attack .....	48
b. Results for 30 Degrees Angle of Attack .....	52
3. m-Moment (pitch) .....	54
a. Results for 20 and 25 Degrees Angle of Attack .....	54
b. Results for 30 Degrees Angle of Attack .....	57
4. Longitudinal Parameters Summary .....	58
B. LATERAL-DIRECTIONAL PARAMETERS .....	59
1. Y-Force (side force) .....	60
a. Results for 20 and 25 Degrees Angle of Attack .....	60
b. Results for 30 Degrees Angle of Attack .....	63
2. l-Moment (roll) .....	65
a. Results for 20 and 25 Degrees Angle of Attack .....	65
b. Results for 30 Degrees Angle of Attack .....	68
3. n-Moment (yaw) .....	70
a. Results for 20 and 25 Degrees Angle of Attack .....	70
b. Results for 30 Degrees Angle of Attack .....	74
4. Lateral-Directional Parameters Summary .....	75
C. CORRELATION MATRICES .....	76
VI. CONCLUSIONS AND RECOMMENDATIONS .....	81
A. CONCLUSIONS .....	81
B. RECOMMENDATIONS .....	81
LIST OF REFERENCES .....	83
APPENDIX A. EQUATIONS OF MOTION .....	85
APPENDIX B. COMPUTER SOFTWARE .....	91
APPENDIX C. ROOT MEAN SQUARE & STANDARD DEVIATION .....	101
INITIAL DISTRIBUTION LIST .....	103

## NOMENCLATURE

$b$	reference span
$c$	reference chord
$C_L$	coefficient of lift
$C_Y$	coefficient of lateral force
$C_l$	coefficient of rolling moment
$C_m$	coefficient of pitching moment
$C_n$	coefficient of yawing moment
$C_A$	coefficient of axial force
$C_N$	coefficient of normal force
$C_{A_0}, C_{A_\alpha}, C_{A_q}, C_{A_{\delta e}},$ $C_{A_{\delta ef}}, C_{A_{\delta as}}$	axial force parameters
$C_{N_0}, C_{N_\alpha}, C_{N_q}, C_{N_{\delta e}},$ $C_{N_{\delta ef}}, C_{N_{\delta as}}$	normal force parameters
$C_{Y_0}, C_{Y_\beta}, C_{Y_p}, C_{Y_r},$ $C_{Y_{\delta \alpha}}, C_{Y_{\delta \beta}}, C_{Y_{\delta \eta}}$	lateral force parameters
$C_{l_0}, C_{l_\beta}, C_{l_p}, C_{l_r},$ $C_{l_{\delta \alpha}}, C_{l_{\delta \beta}}, C_{l_{\delta \eta}}$	rolling moment parameters
$C_{m_0}, C_{m_\alpha}, C_{m_q}, C_{m_{\delta e}},$ $C_{m_{\delta ef}}, C_{m_{\delta as}}$	pitching moment parameters
$C_{n_0}, C_{n_\beta}, C_{n_p}, C_{n_r},$ $C_{n_{\delta \alpha}}, C_{n_{\delta \beta}}, C_{n_{\delta \eta}}$	yawing moment parameters
$C_{\delta p v}, C_{\delta y v}$	thrust vectoring parameters
$\delta \alpha$	aileron deflection
$\delta \alpha s$	simultaneous aileron deflection
$\delta e$	elevator deflection
$\delta h$	differential horizontal tail deflection
$\delta p v$	thrust vectoring pitch vanes deflection
$\delta r$	rudder deflection
$\delta e f$	trailing edge flaps deflection
$\delta y v$	thrust vectoring yaw vanes deflection

<i>f</i>	state derivative function
FDAS	Flight Data Acquisition system
<i>g</i>	response function
<i>g</i>	gravitational acceleration
GetData	Time History data manipulating software
GetFdas	Time History retrievable data system
HARV	High Alpha Research Vehicle
HATP	High Angle of Attack Technology Program
$I_x, I_y, I_z$	moments of inertia
$I_{xy}, I_{xz}, I_{yz}$	cross products of inertia
<i>J</i>	Cost Function
<i>L</i>	Likelihood functional
<i>m</i>	mass
M	Aircraft System
OBES	On Board Exciter System
<i>p</i>	roll rate
pEst	parameter estimation program
<i>q</i>	pitch rate
$\bar{q}$	dynamic pressure
<i>r</i>	yaw rate
<i>R</i>	conversion factor (57.2958)
RAV	Remote Augmented Vehicle
RFCS	Research Flight Control System
<i>s</i>	reference area
SSI	Single-surface input
<b>u</b>	control input vector
<i>V</i>	total velocity
W	response weighting matrix

$y$	output vector
$z$	response or outcome
$\alpha$	angle of attack
$\beta$	angle of sideslip
$\epsilon$	chosen error
$\theta$	pitch attitude
$\phi$	roll attitude
$\xi$	parameter vector
$\wedge$	computed response



## **ACKNOWLEDGMENTS**

I would like to thank both Albion H. Bowers and Brent R. Cobleigh, my mentors, from NASA Dryden Flight Research Center for their time and guidance in the topic of parameter estimation. The knowledge I gained while working at NASA with these men is invaluable. I would also like to thank Professor Richard M. Howard for arranging my experience tour at NASA Dryden Center and stimulating my interest in the field of parameter estimation. Many thanks belong to Professor Daniel J. Collins for his patience and wisdom during this endeavor. Finally, I would like to thank my family, especially my wife Lisa, for her support and forbearance throughout this long process.

## I. INTRODUCTION

### A. BACKGROUND

Parameter estimation is an inverse process in which the measured response and measured input of an actual system are known and the coefficients of the mathematical model, parameters, are then determined based on the fact that the mathematical model computed response best match the actual measured response. Figure 1.1 is a simple block diagram representation of parameter estimation which includes two fields that support the continued research in system identification.

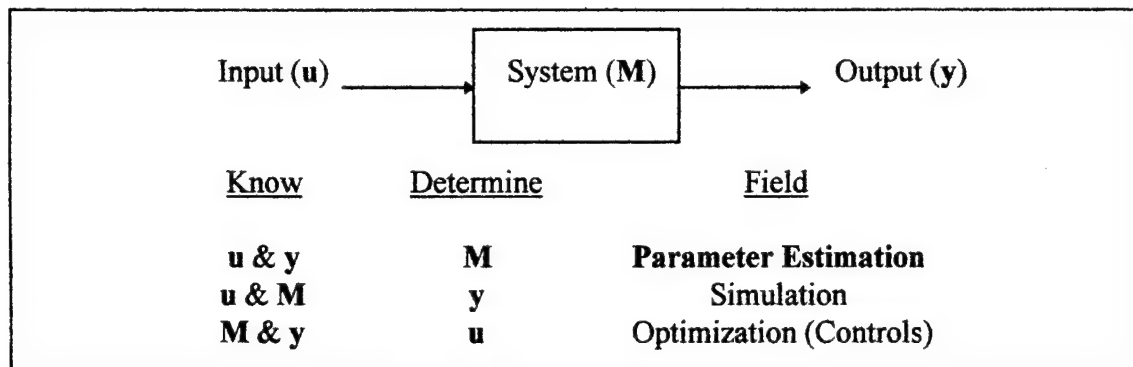


Figure 1.1. Parameter Estimation

Mathematical model coefficients and/or parameters are more commonly referred to as dynamic and control stability derivatives. Stability derivatives simply define the stability and control characteristics of the aircraft. Control characteristics of an aircraft are of great interest to the aeronautical engineer, but the aerodynamic forces and moments needed to determine such characteristics cannot be measured directly in flight. Therefore, parameter estimation techniques were developed to use measurable quantities, such as resulting motion from the change in control surface deflection forces. The technique has not changed since the original concept was conceived, but the accuracy, complexity, and expedience of parameter estimation have greatly improved. Original

analysis used simplified one-degree-of-freedom equations of motion and solved for one parameter at a time while fixing other parameters. Technological advancements lead to the present analysis of full six-degree-of-freedom nonlinear equations of motion which are solved simultaneously for all the parameters.

The evolution of parameter estimation progressed as higher performance aircraft were developed and data acquisition and analysis tools improved. Two factors which caused a revolution in parameter estimation techniques starting in the mid-1960's were:

- (1) highly automated data acquisition systems became a standard in flight testing equipment, and
- (2) large capacity, high-speed digital computers were available to solve complicated algorithms efficiently. [Ref. 1]

These two factors enabled accurate parameters to be determined in a matter of a few hours from the flight test versus days or months from previous methods.

Accurate parameter estimation from flight testing is becoming more important as the performance and capabilities of aircraft increase. Parameter estimates from flight data are used to:

- (1) verify wind tunnel parameter estimates;
- (2) update aircraft dynamic models for flight control system analysis and design;
- (3) justify and improve *a priori* aerodynamic computations;
- (4) predict aircraft responses for realistic flight simulation and ground-based flight training. [Ref. 2]

The four reasons as stated above validate the importance of parameter estimation. The fact that safety margins and flight constraints can be and are determined by parameter estimations also indicates the importance of the method.

The goal of the aerodynamic engineer is to produce accurate parameter estimates. Good parameter identification depends on instrumentation, input, aerodynamic mathematical model, analysis technique and region of flight. The region of flight is important due to the extreme differences between low and high angle of attack. Accurate

parameter estimation is significantly easier at small angles of attack since the small perturbations involved, approximate linear models. In flight regime of high angles of attack which introduce large perturbations, non-linearity, and input maneuvers that are limited in magnitude and duration, parameter estimation is much more difficult. The advent of more capable aircraft has made research into parameter estimation at high angles of attack more important.

The increased interest in aircraft with more maneuverability and stability at higher angles of attack influenced the National Aeronautics and Space Administration (NASA) to start the High Angle-of-Attack Technology Program (HATP). The NASA High Angle-of-Attack Technology Program was designed to investigate a series of objectives at high alpha flight. These objectives included but were not limited to aerodynamics, controls, engine inlets, computational fluid dynamics, and advanced control laws. Parameter estimation is part of the aerodynamic portion of the program. The HATP consists of full integration of all the NASA research centers working on a single research program in high angle of attack flight. The NASA Dryden Research Center is the flight test center for the program.

A highly modified F-18 airframe, the High Alpha Research Vehicle (HARV), is used as the test bed aircraft. The F-18 was originally 'Full Scale Development Ship 6' used by McDonnell Douglas Corp. for F-18 configuration testing at high angles of attack to include departed flight (spins). For the spin flights, the aircraft was modified with the addition of a spin chute and with emergency battery power systems. The F-18's known high angle of attack capabilities coupled with the platforms availability, made the aircraft an excellent flight-test vehicle for the HATP. Subsequent modifications to the HARV for the HATP included:

- (1) Thrust Vectoring & Control system -- three thrust vectoring vanes made of Nickel Alloy (Inconel 625) positioned externally to each exhaust nozzle, and a separate Research Flight Control System (RFCS) written into the control law.
- (2) Upgraded Instrumentation systems;

- (3) Highly Modified Aircraft systems;
- (4) Emergency systems;
- (5) Special Flight Control Computer. [Ref. 3]

The RFCS flight control system for vectored thrust adds control capability up to 60 degrees angle of attack for the HARV. The thrust vectoring vanes add another control surface to the mathematical model used for parameter estimation.

Recently, optimal input maneuver techniques have been designed and developed for parameter estimation at high angles of attack. Optimal input is desirable for achieving maximum accuracy of parameter estimation in minimum flight time. Optimal inputs and more traditional inputs such as doublets were used for parameter estimation of the HARV.

## **B. PURPOSE**

Input technique was mentioned earlier as an important factor in good parameter estimation. One objective of the HATP was the improvement of parameter identification at high angles of attack. The purpose of this research is to:

- (1) Analyze recorded flight data from HARV flights at high angles of attack for which both classical inputs and optimal inputs were applied under the same flight conditions;
- (2) Conduct parameter estimations to determine estimates of stability and control derivatives and their Cramer-Rao bounds for each input technique; and
- (3) Compare the Cramer-Rao bounds of each technique to determine which input produces the most accurate parameters.

## II. MAXIMUM LIKELIHOOD ESTIMATOR

The maximum likelihood estimator technique was introduced into statistics by R.A. Fisher in 1906. The technique assumes that an outcome  $Z$  of an experiment is determined by some unknown parameter  $\xi$ . From the outcome  $Z$  an initial best guess is inferred for  $\xi$ . The obvious best guess would be  $\xi$  such that the observed value of  $Z$  is the most probable. Stated mathematically: select  $\xi$  to maximize the conditional probability of  $Z$ , given  $\xi$ ; or

$$\hat{\xi} = \max_{\xi} p(Z | \xi) \quad (2.1)$$

where  $\hat{\xi}$  is the maximum likelihood estimate of  $\xi$  and  $p(Z | \xi)$  is the conditional probability of  $Z$ , given  $\xi$ . [Ref. 4] The technique is an iterative process where the updated values of  $\xi$  depend on the output error which is the difference between the measured response and the computed response. Parameter estimation using the maximum likelihood method is similar to the output-error approach of reference [5].

Maximum likelihood estimation is the most commonly used estimator technique for parameter estimates from flight data. The single largest reason for using the maximum likelihood method is that no prior information or probability distribution for  $\xi$  is required. This is not the case in other estimator techniques. In addition the maximum likelihood estimates are efficient and unbiased, and the mean square error is equal to the Cramer-Rao bound. The Cramer-Rao bound is an indication of the accuracy of the estimate and will be discussed later. Derivation of the maximum likelihood technique will not be addressed in this thesis, but references [5] through [8] provide detailed information on the topic.

## A. PARAMETER ESTIMATION PROGRAM (pEst)

'pEst' is an interactive, maximum likelihood, parameter estimation program for determining flight dynamic derivatives developed by Murray and Maine of NASA Dryden. [Ref. 9] The program permits the user total freedom in defining the equations of motion. Equations can be linear or non-linear as required by the analysis. Subroutines inside pEst define a generic set of non-linear equations of motion for an aircraft which are used as default equations for parameter estimation if original equations are not entered.

Equations of motion are defined to best represent the dynamic system being modeled. The more accurate the model the more accurate the estimates for the dynamic derivatives will be when the estimation process is complete. Once the model has been determined, an experiment can be run while recording the input and measuring the output. The idea is to adjust the values of the unknown parameters in the model until the computed response from the model best matches the measured response of the actual system (Maximum Likelihood). To accomplish these results the pEst program:

- (1) defines a cost function based on the difference between the measured response and the computed response; and
- (2) lets the user choose a minimization algorithm to mechanize the search for the unknown parameters. [Ref. 9]

The cost function used inside the pEst program is defined as:

$$J(\xi) = \frac{1}{2n_z n_t} \sum_{i=1}^{n_t} [z(t_i) - \hat{z}(t_i)]^* W [z(t_i) - \hat{z}(t_i)] \quad (2.2)$$

where  $n_t$  and  $n_z$  are the numbers of time history points and response variables respectively,  $t$  is the time variable,  $W$  the response weighting matrix,  $z$  the measured response and  $\hat{z}$  the computed response. Minimizing the cost function  $J(\xi)$  is equivalent to maximizing the likelihood functional:

$$L(\xi) = p(Z | \xi) \Big|_{Z = Z_{\text{measured}}} \quad (2.3)$$

Figure 2.1 is an illustration of the pEst process. The process begins with a control input used in a flight-test maneuver. Time history data of the maneuver are recorded as the measured response which includes noise. A nonlinear aircraft model uses the recorded time history data in the form of a *measured* file to determine a computed response. The two responses are compared to produce an output error. The error is supplied to a cost function along with a minimization algorithm to determine estimates of the parameters and uncertainty bounds. These parameter values are placed back into the nonlinear aircraft model and a new computed response determined. When two iterative values of the cost function have a difference less than a given tolerance the iterative process stops and final parameter estimates and uncertainty bounds are yielded.

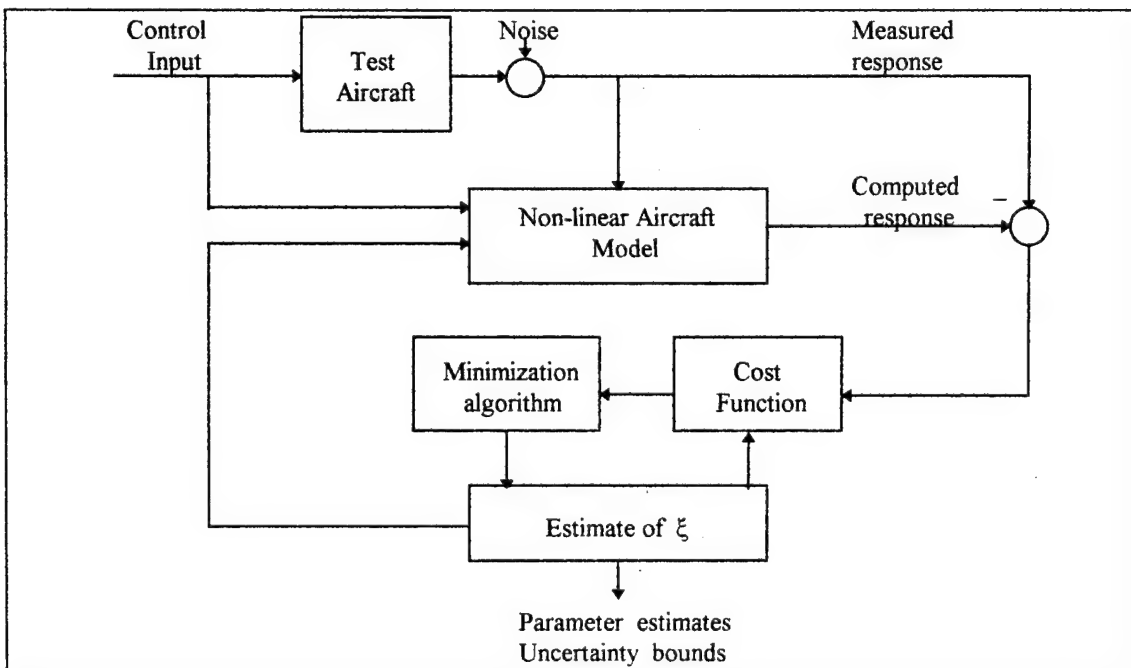


Figure 2.1. From Ref.[9]. The pEst Parameter Estimation Process.

The iterative process in 'pEst' is started once the user loads a *measured* file and *current* file of choice. A *measured* file is a time history flight data file of the measured input and response. The *current* file is an interactive file which allows the user to choose what parameters will be estimated as well as what minimization technique is applied. For more details refer to reference [9].

## B. MATHEMATICAL MODEL

The mathematical model (i.e. equations of motion) used inside 'pEst' to model the actual system is a critical element in parameter estimation. The more accurate the model the more accurate the parameters. Therefore, inherent to accurate parameter estimation is the development of a good mathematical model.

Derivation of the model is not presented here but can be found in reference [5]. The equations of motion used in 'pEst' are a set of ordinary differential equations. Both a continuous system and a discrete system of equations are used to represent the model in 'pEst'. The system equations are:

$$\begin{aligned} x(t_0) &= x_0 \\ \dot{x}(t) &= f[x(t), u(t), \xi] \\ z(t_i) &= g[x(t_i), u(t_i), \xi] \end{aligned} \tag{2.4}$$

where  $x$  is the state variable,  $u$  the input variable,  $f$  the state derivative function,  $g$  the response function, and  $\xi$  the vector of parameters. The fully developed equations of motion are listed in Appendix A.

### 1. Control Surfaces Used in the Model

The modeling of a highly augmented aircraft like the F-18 HARV is difficult. The HARV has been modified with many extra control surfaces which affect the

response of the aircraft. These modifications have been implemented into the control laws for the HARV and are accounted for in the systems equations of motion. The control surfaces used are divided into longitudinal and lateral-directional surfaces.

The longitudinal control surfaces used in the model for the research in this thesis are elevator, simultaneous aileron, trailing edge flaps, and pitch thrust vectoring vanes shown in Figures 2.2 and 2.3. The elevator is really the two horizontal stabilators moving in unison as an elevator. The trailing edge flaps and simultaneous aileron control surfaces are both located along the aft trailing edge of the wing. The simultaneous aileron input was an added modification for extra pitch authority at high angles of attack. Instead of the ailerons moving in opposite directions they move together in the same direction. Trailing edge flaps act similarly to the simultaneous aileron input and are located inboard on the wing with respect to the ailerons. The flaps work in tandem like normal flaps but are limited in movement based on angle of attack. At 26 degrees angle of attack the trailing edge flaps lock full down and therefore should not be used as a control surface input when running 'pEst' on maneuvers with angle of attack greater than 26 degrees. The pitch thrust vectoring vanes are shown in Figure 2.3. The vanes move as follows: vanes 1 and 4 above the exhaust nozzles move together, vanes 2 and 6 below and left of the exhaust nozzles move together, and vanes 3 and 5 below and right of the exhaust nozzles move together. A pitch control input moves the vanes together so that the lateral thrust vector component is zero.

The lateral-directional control surfaces used in the model for the research in this thesis are aileron, rudder, differential horizontal tail, and yaw thrust-vectoring vanes. Ailerons and rudders are conventional control surfaces normally used in lateral-directional modeling. The differential horizontal tail is derived from the horizontal stabilators acting like ailerons. One stabilator moves in one direction while the other moves in the opposite direction to produce a rolling moment. Yaw thrust-vectoring vanes are used to produce a yawing moment. Vanes 2 and 6 move together to give a

positive yawing moment (nose right) while vanes 3 and 5 move together to give a negative yawing moment.

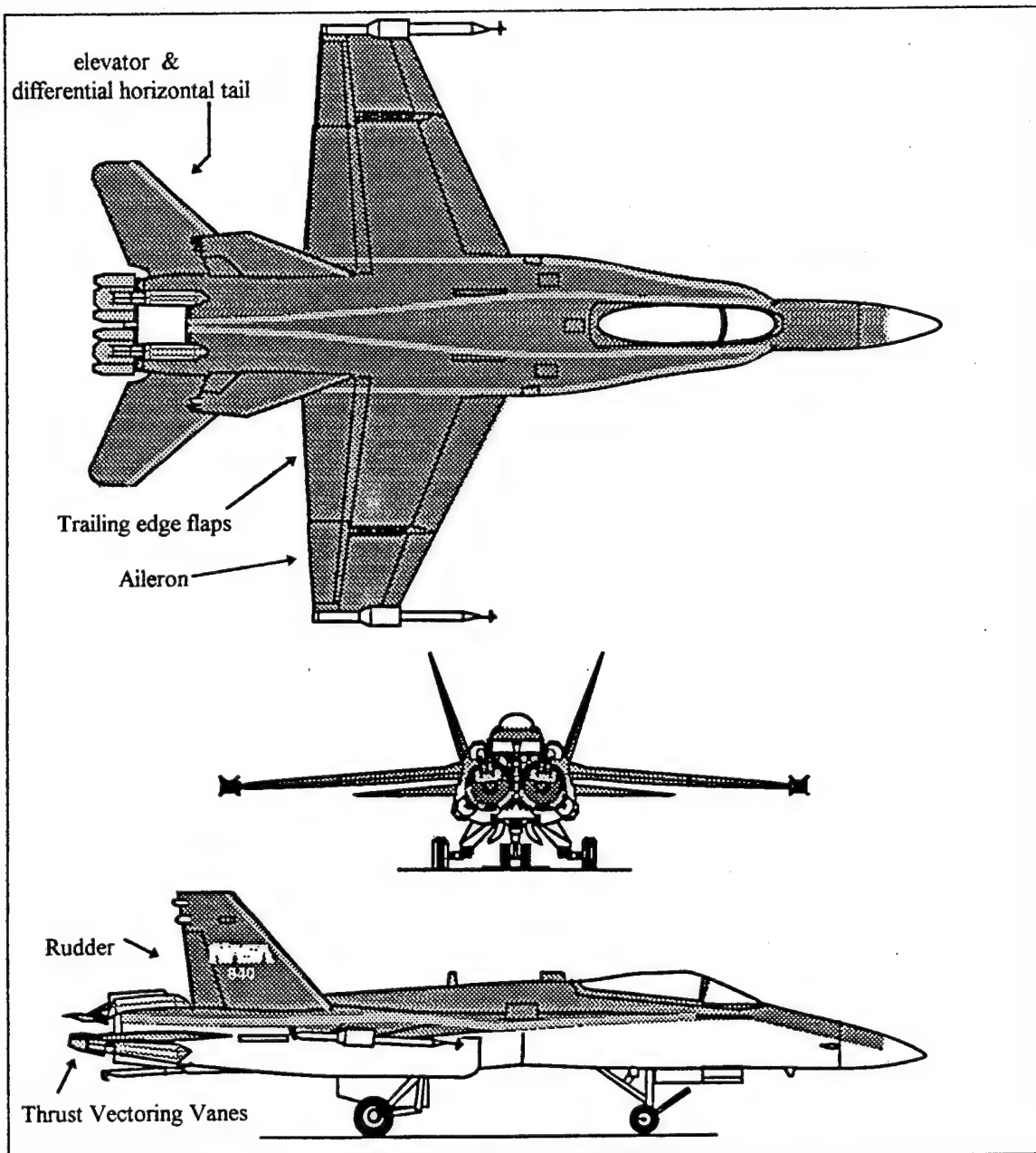


Figure 2.2. From Ref. [3]. The Control Surfaces on the HARV.

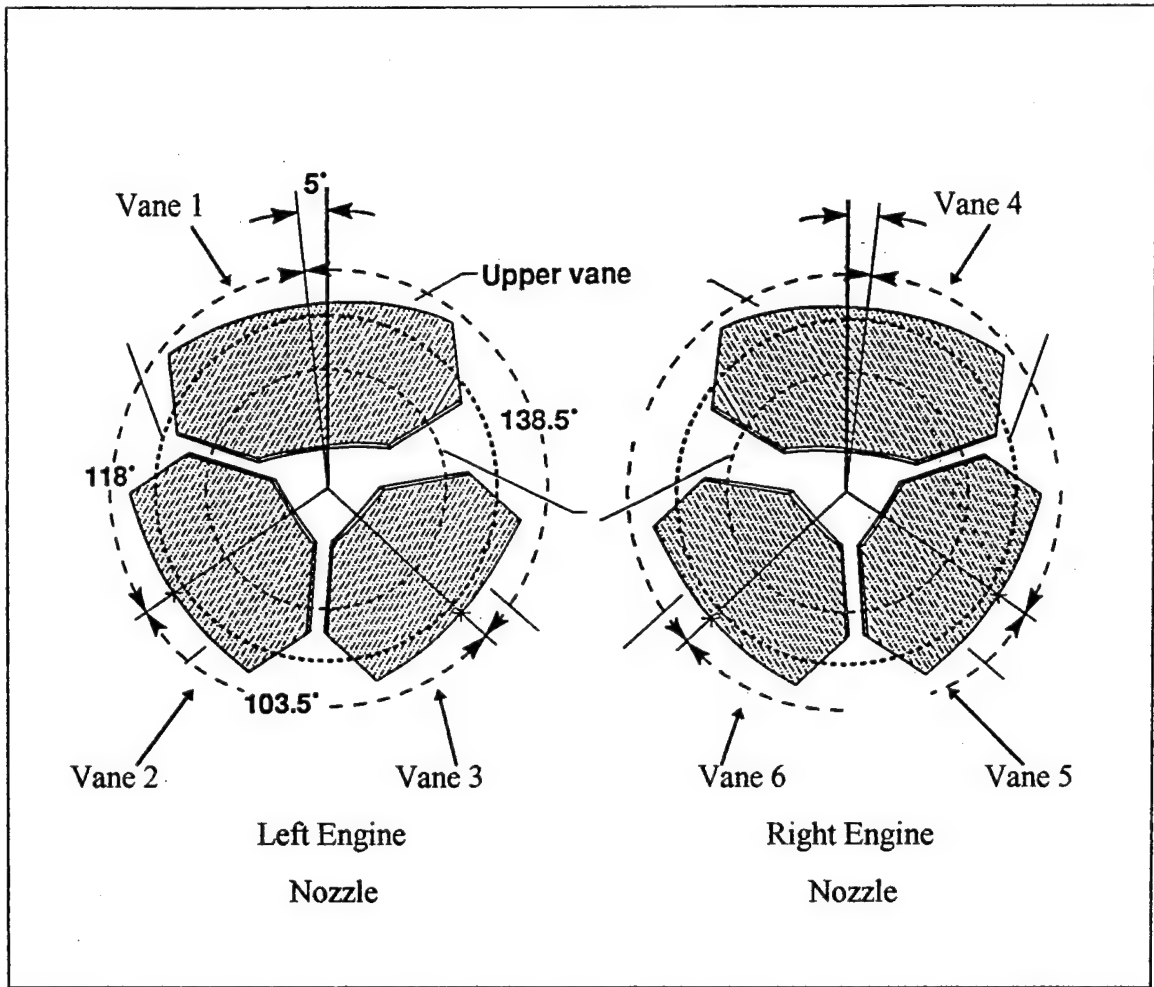


Figure 2.3. After Ref. [3]. The Thrust Vectoring Configuration on the HARV.

## 2. Convergence Criterion

Numerical solutions to systems of differential equations use an iterative process to solve the system. The pEst code, like all numerical methods, requires a convergence criterion to stop the iterative process. The criterion used for convergence is the accuracy of the absolute error between the current cost and the old cost (i.e.):

$$\left| J(\hat{\xi}_i) - J(\hat{\xi}_{i-1}) \right| < \varepsilon \quad (2.5)$$

where  $J(\hat{\xi}_i)$  is current cost and  $J(\hat{\xi}_{i-1})$  is old cost. The cost is a function of the parameter estimates. Epsilon,  $\epsilon$ , is chosen by the user and set in the *current* file. (See *current* file in Appendix B).

### 3. Output Weightings

State outputs are normally divided into two sets: 1) longitudinal and 2) lateral-directional. Longitudinal state outputs are angle of attack ( $\alpha$ ), pitch rate ( $q$ ), pitch angle ( $\theta$ ), and normal acceleration ( $a_n$ ). Lateral-directional state outputs are sideslip angle ( $\beta$ ), roll rate ( $p$ ), yaw rate ( $r$ ), bank angle ( $\phi$ ), and lateral acceleration ( $a_y$ ). Weights on each of the outputs directly affect the pEst parameter estimates. A plot of computed response and measured response versus time graphically shows the difference between the responses for each output state, and indications of weights that are good and weights that are not so good can be perceived. Increasing the weight for a particular state increases the cost function and increases the importance of the parameter estimates related to that state.

The response weighting matrix is a diagonal matrix whose entries correspond to the weight factors chosen by the user. Listed here is a simple two-by-two example of the response weighting matrix where each  $w_{ii}$  corresponds to the weight factor of each output.

$$W = \begin{bmatrix} w_{11} & 0 \\ 0 & w_{22} \end{bmatrix} \quad (2.6)$$

The response weighting matrix is used in the cost function mentioned in section II.A for establishing how much each output will affect the total cost of the cost function. Each factor is listed next to the separate state output at the bottom of the *current* file. Default weights are used for each selected state output if no changes are made by the user.

#### 4. A Priori Information

Knowledge of the parameter estimates before beginning the parameter estimation process is called *a priori* information. The *a priori* values come mainly from wind tunnel results or theoretical calculations based on an actual aircraft configuration. Using *a priori* information in parameter estimation can have both a positive and negative effect. The positive influences are faster convergence and more accurate parameter estimates assuming that the *a priori* information is accurate. Conversely, *a priori* information biases the parameter estimates toward the *a priori* values and can result in poor estimates if the *a priori* knowledge is poor. In the latter case one no longer has efficient unbiased estimates.

Efficient unbiased estimates are estimates which attain the lowest variance from the true value of the estimate.[Ref. 10] When conducting parameter estimation, efficient estimates are favorable estimates. The maximum likelihood estimator, if it exists, is an efficient estimator and no preference is given to any estimate,  $\xi$ , prior to the beginning of parameter estimation. The negative affect of *a priori* information is inefficient estimates.

#### C. MINIMIZATION TECHNIQUE

Most estimators including pEst require the minimization or maximization of a nonlinear function. Interactive numerical algorithms based on optimization are the most common solutions. The optimization problem is to determine the value of the vector  $\mathbf{x}$  that makes the scalar-valued function  $J(\mathbf{x})$  smallest. This function is normally called the cost function. In most cases constraints are placed on input and output amplitudes so that a solution for  $\mathbf{x}$  will exist. References [11-13] explain the details of the optimization methods that have been purposely omitted here.

There are 6 minimization algorithms used by 'pEst' for minimizing the cost function  $J(\xi)$ . The user needs to choose one of the six following options:

- (1) Levenberg-Marquardt Method;

- (2) Levenberg-Marquardt with search Method;
- (3) Gauss-Newton Method;
- (4) Davidson-Fletcher-Powell Method;
- (5) Broyden-Fletcher-Goldfarb-Shanno Method; and
- (6) Steepest descent (gradient) Method.

All of the six options are concerned with local minimum, not global minimum, although arguments can often be used to imply global minimum. The definition of a local minimum is:  $\hat{\xi}$  is a local minimum of  $J(\xi)$  if there exists a scalar  $\delta > 0$  such that  $J(\hat{\xi}) \leq J(\hat{\xi} + \kappa)$  for all  $\kappa$  in which  $|\kappa| < \delta$ . 'pEst' determines the best values for the parameters  $\xi$  by employing one of the minimization techniques to find  $\xi$  which satisfies the stated definition for each parameter's local minimum.

The recommended minimization technique and default setting in 'pEst' is the Levenberg-Marquardt method. The Levenberg-Marquardt method is a very robust, nonlinear, least-squares method which combines the steepest descent (gradient) method and inverse Hessian method. Initially the method uses the steepest descent method to quickly approach a probable solution. Once the parameters are near values which minimize the cost function, the inverse Hessian method is used to smooth the solution. The inverse Hessian method is similar to the Newton-Raphson method, [Ref. 10] which depends on the second partial of the cost function with respect to the parameter vector  $\xi$ . The Newton-Raphson method is the basis for all second order methods which approximates the cost function by the first three terms of its Taylor series expansion about the current parameter estimates,  $\xi$ . The Newton-Raphson method is known for its quadratic convergence, but has poor performance when  $J(\xi)$  is far from the minimum. The Levenberg-Marquardt method eliminates the poor performance problem when a minimum exists. Components of the Hessian matrix are used to scale the problem to determine when the switch from steepest descent to inverse Hessian should occur. Reference [14] provides an explicit derivation of the Levenberg-Marquardt method.

Prior to the Levenberg-Marquardt method being implemented into 'pEst', the best approach for parameter estimation was to begin the iterative process using the gradient method and switch to the Newton method once the solution was close to the minimum. To verify that the Levenberg-Marquardt method is the best, other methods were also used to determine the parameters. Parameters computed from the approach using the gradient technique first, then Newton's method, were compared to parameters determined from the Levenberg-Marquardt method. The final parameters determined from both cases were identical to the fifth decimal place, but the Levenberg-Marquardt method was more user friendly and did not require additional commands in the middle of the estimation process. Therefore, the parameter estimates determined in this thesis were from the Levenberg-Marquardt method.

#### **D. MEASURES OF ACCURACY**

Accuracy of the parameter estimates is a critical issue of parameter estimation. If the estimates are going to be implemented in some control law or control system then some measure of judgment is needed to determine if the values obtained for the estimates are of sufficient accuracy.

Measures of accuracy are affected by modeling problems. However, for the analysis in this thesis the model is assumed to be exact, and accuracy is a measurement of the error in the estimates. Using the error in the estimate approach, accuracy becomes a quantitative measure. The following paragraphs briefly explain two of the measures of accuracy used in parameter estimation. Further explanation of these measures can be found in references [10 and 15].

##### **1. Insensitivity**

Statistically measures of accuracy of estimated parameters are based on uncertainty regions. For the analysis in this thesis, an ellipsoid is used for the uncertainty region. An uncertainty ellipsoid for two parameters is shown in Figure 2.4. In Figure 2.4

the vertical axis is the cost function,  $J(\xi)$ , whose value depends on the parameters,  $\xi_i$ . For a one-dimensional case, the amount of change ( $\Delta\xi$ ) allowed in a parameter such that  $J(\xi)$  remains within a certain bound ( $\Delta J$ ) is called the insensitivity of that parameter. Insensitivity is a conditional measure where by all of the other parameters are fixed when determining the insensitivity of one parameter. Figure 2.5 is a geometric representation of the insensitivity in a problem with two unknown parameters. [Ref. 10] The insensitivities of  $\xi_1$  and  $\xi_2$  are indicated by  $I_1$  and  $I_2$ . Insensitivity is a reasonable measure of accuracy for one-dimensional problems, but aircraft problems have dimensions much larger than one.

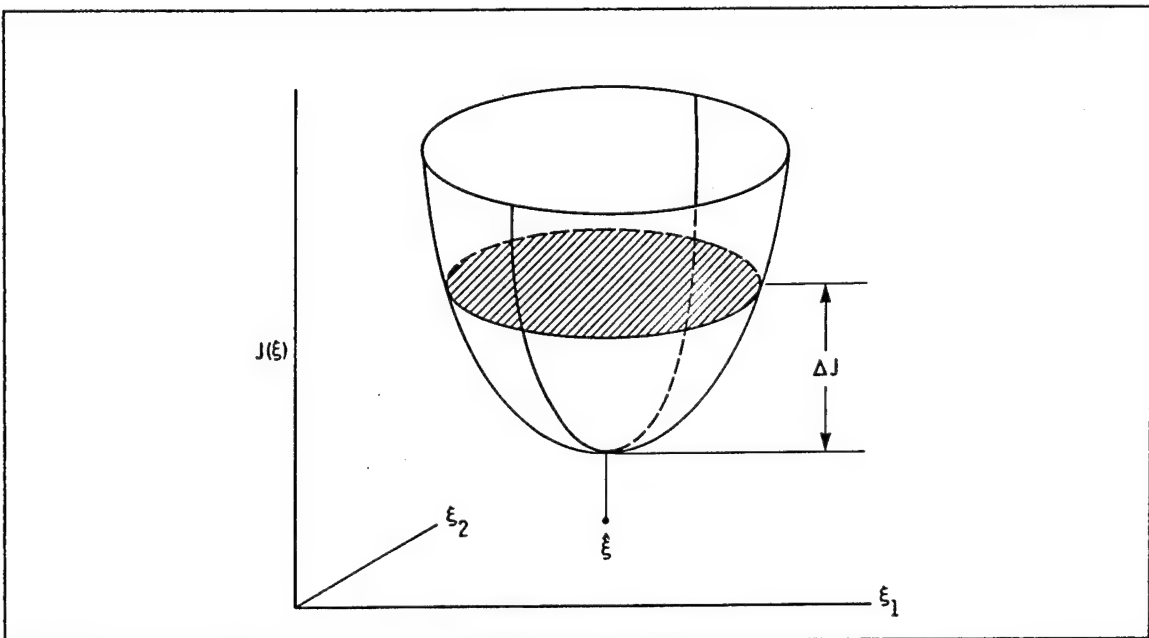


Figure 2.4. From Ref. [15]. An Uncertainty Ellipsoid for Two Parameters.

## 2. Cramer-Rao Bound

Most parameter estimation problems do not have any knowledge of the parameter values before beginning the parameter estimation process. Without this knowledge another measure of accuracy is needed for multi-dimensional problems. The most useful measure from the uncertainty ellipsoid is the Cramer-Rao bound.

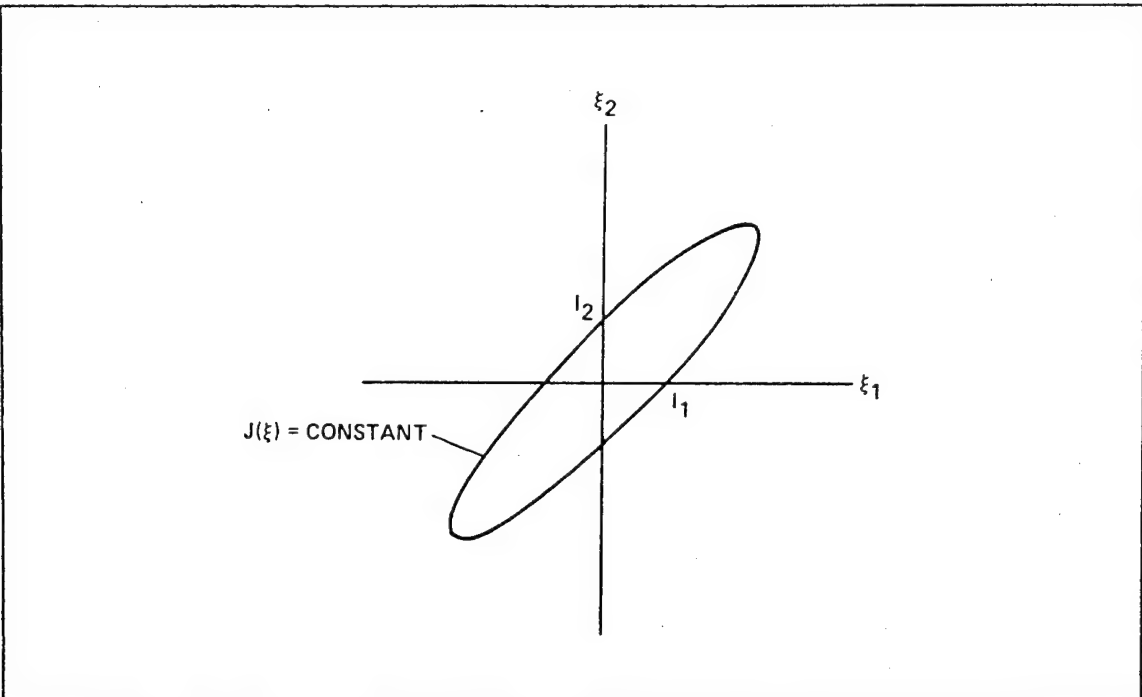


Figure 2.5. From Ref. [10]. A Geometric Representation of Insensitivity.

Statistically the Cramer-Rao bound of an estimated parameter is the unconditional standard deviation of the error in that parameter. Unconditional deviation is used as opposed to conditional deviation to note that none of the parameters is known or fixed as was the case with insensitivity. The Cramer-Rao bound is similar to insensitivity except for the conditional factor. The Cramer-Rao bound is the largest change ( $\Delta\xi$ ) a parameter can have and not cause the solution to leave the uncertainty ellipsoid defined by  $J(\xi) = \text{constant}$ . The fact that the Cramer-Rao bound is unconditional is the reason why the bound is useful in measuring the accuracy of parameter estimates. Derivation of the Cramer-Rao bound is found in reference [15]. Figure 2.6 shows an uncertainty ellipsoid with both the insensitivity ( $I_1, I_2$ ) and the Cramer-Rao bounds ( $C_1, C_2$ ) for two parameters. The insensitivity for each parameter is indicated as before in Figure 2.5, and the Cramer-Rao bound is indicated as  $C_1$  and  $C_2$  for each respective parameter  $\xi_1$  and  $\xi_2$ .

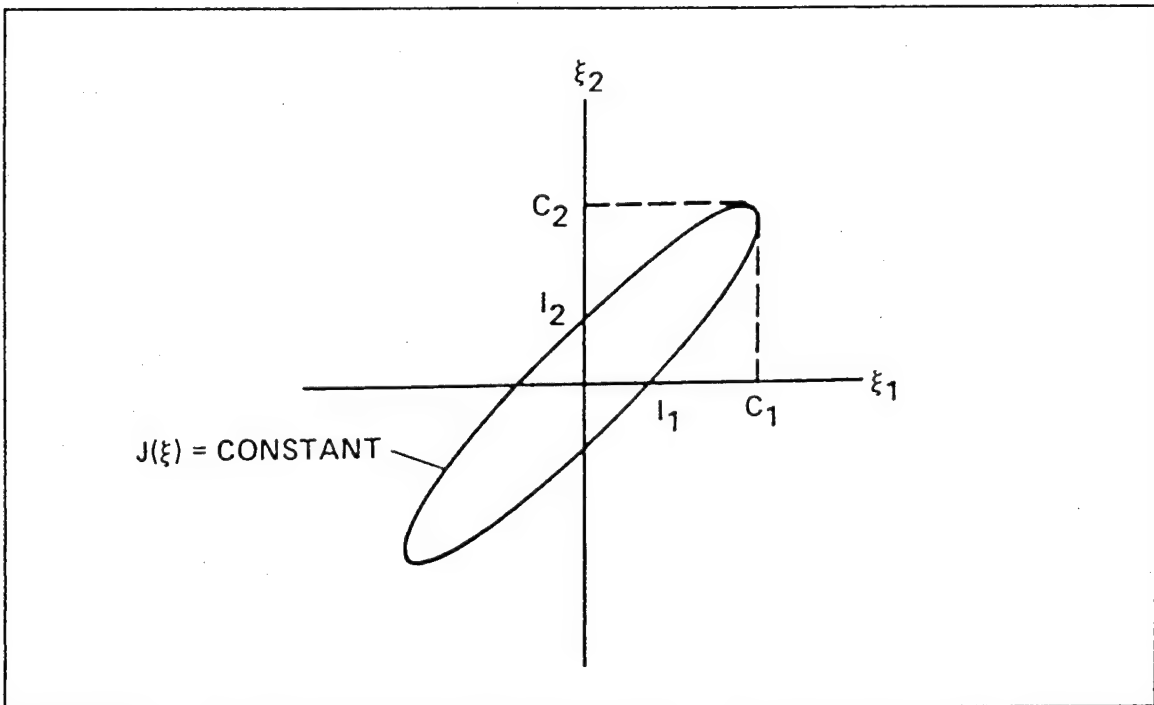


Figure 2.6. From Ref. [10]. The Cramer-Rao Bound and Insensitivity.

The Cramer-Rao bound is the unconditional measure of accuracy used in the comparison analysis in this thesis. Insensitivity effects are included in the Cramer-Rao bound. Therefore, insensitivity will not provide any additional information about the accuracy of the parameter estimations. However, insensitivities can be used as a means to help determine causes of inaccuracies since it is a sufficient measure for one-dimensional problems. Insensitivity can provide information on the slope of a specific parameter which might explain why that specific parameter has a high Cramer-Rao bound. In general, high insensitivity corresponds with a flat sloped function which yields a high Cramer-Rao bound for that parameter.

#### E. CORRELATION

Accurate parameter estimation requires low correlation and good excitation of the system in all the axes of rotation. An example from the HARV research aircraft provides

a clearer understanding of correlation. When the HARV has the RFCS engaged, pitch vane deflection and elevator deflection are two separate control surfaces which are both located in close proximity on the aircraft. These surfaces when deflected also excite motion response along the same axis. Therefore, if these two surfaces move together (highly correlated) and cause the same longitudinal pitching response, it is difficult to determine how much of the response was caused by each of the respective control surfaces. The high correlated motion of control surfaces can result in inaccurate parameter estimates. The best way to check for correlation is plot the separate inputs versus each other. Figure 2.7 is a plot of the aileron input ( $\delta_a$ ) versus the differential horizontal tail ( $\delta_h$ ) showing high correlation. The correlated response is similar to a hysteresis loop. A linear relationship between the two control surfaces given by  $\delta_a = 2 \delta_h$  is a good representation of the data. The normal coefficient for the aircraft motion is defined in 'pEst' by:

$$C_n = C_{n_0} + C_{n_{\delta_a}} \delta_a + C_{n_{\delta_h}} \delta_h + \dots \quad (2.7)$$

if one inserts  $\delta_a = 2 \delta_h$  the equation becomes:

$$C_n = C_{n_0} + C_{n_{\delta_a}} (2 \delta_h) + C_{n_{\delta_h}} \delta_h + \dots = C_{n_0} + (2 C_{n_{\delta_a}} + C_{n_{\delta_h}}) \delta_h + \dots \quad (2.8)$$

In this case the high correlation prevents  $C_{n_{\delta_a}}$  and  $C_{n_{\delta_h}}$  from being determined accurately. Figure 2.8 is a plot from the same maneuver between two different control surfaces showing low correlation. In the second plot, the lack of correlation between the control inputs facilitates accurate parameter identification.

Correlation in the data is caused by the control law due to feedback. In fact at high angles of attack a good control law will have high correlation. The reason for high correlation is that each of the control surfaces act together to produce a desired result. For aircraft control purposes this is a favorable outcome. However, these concurrent inputs which produce the same motion response make parameter estimation difficult.

The cause of correlation is feedback in the control law. When no correlated inputs are used for a maneuver, some correlation is added into the data due to feedback. The flight control system uses feedback to compare the actual output with what output was commanded by the input. Changes to the input are then made automatically by the flight control system to produce the most efficient input to achieve the commanded output. The most efficient input is going to use all of the control surfaces to produce the same output. This efficient input will have some correlation.

One way to decrease the correlation is to not use a feedback loop in the control law, but stability of the system would be questionable. Another method to decrease correlation is to degrade the control power to control surfaces not being used in a specific input. The later approach has been used with some input techniques on the HARV. Both of the previous suggestions try to reduce the correlation in the data. If the correlation is already in the data, output weights in the weighting response matrix can help 'pEst' in determining more accurate parameters, but the correlation in the data will not be removed.

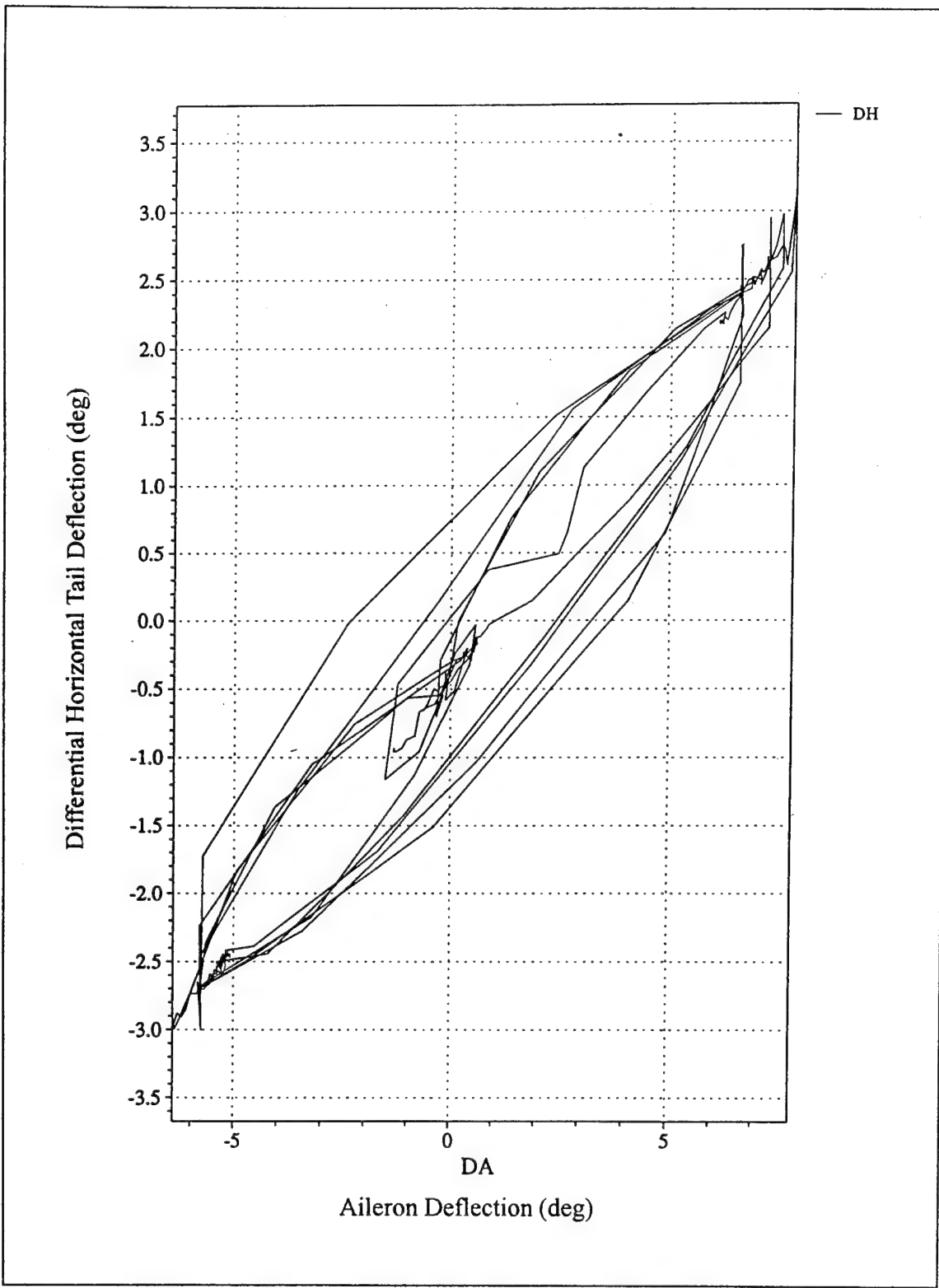


Figure 2.7. High Correlation between two Control Surface Inputs.

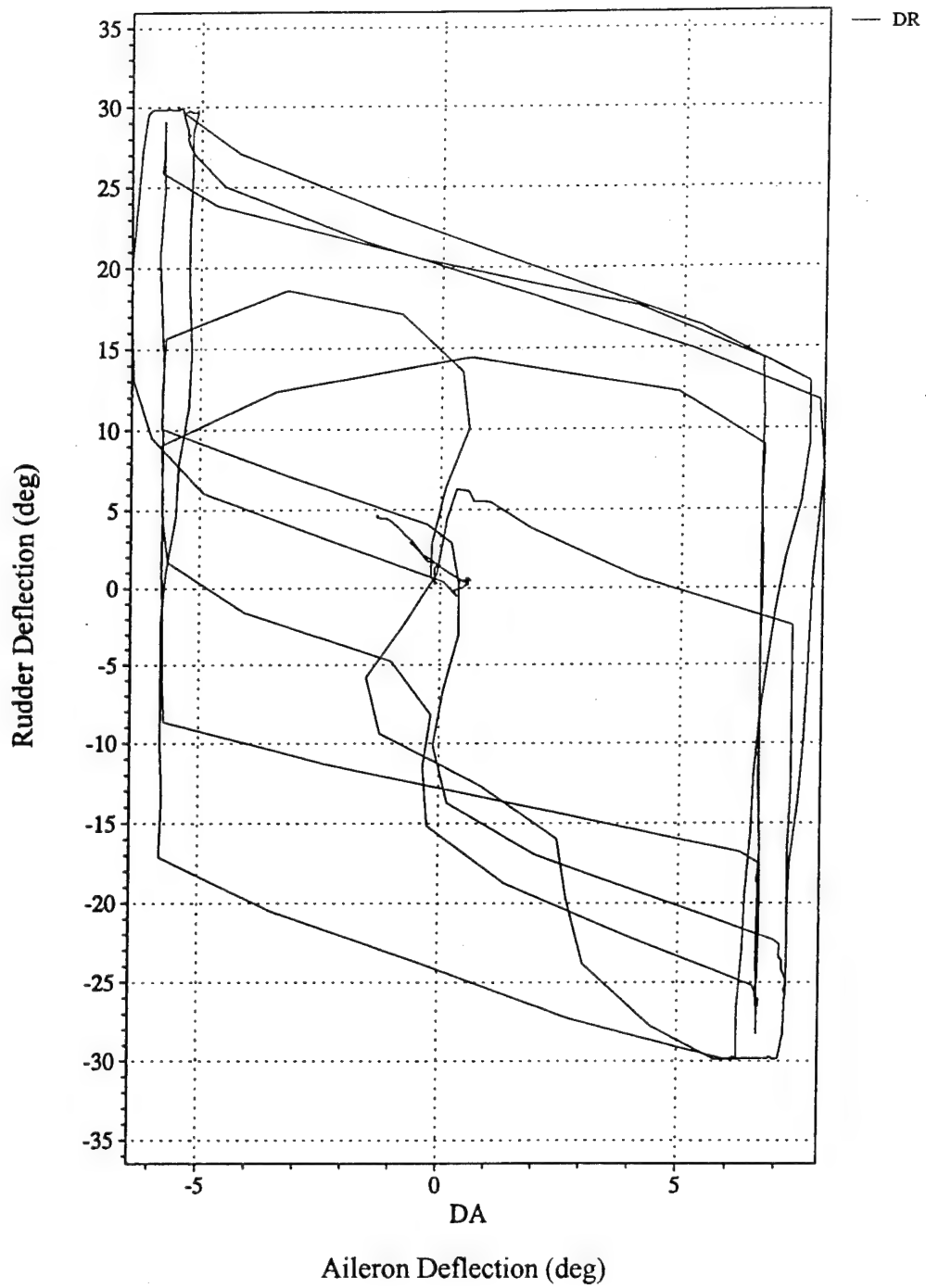


Figure 2.8. Low Correlation between two Input Control Surfaces.

### III. INPUT TECHNIQUES

Good parameter estimation depends mainly on instrumentation and input. Inputs need to excite the aircraft motion in such a way that the derivatives can be independently estimated. Excitement depends on the power and frequency of the input. The idea is to excite the different modes of the aircraft (short period, phugoid, dutch roll) to cause motion which allows easy determination of the parameters. Four different input techniques have been used on the HARV for parameter estimation. The four input techniques are doublets, single-surface inputs, and two optimal input techniques. With good instrumentation and inputs, data can be measured and recorded that result in accurate parameter estimates. Instrumentation includes location, time shifts, resolution, and accuracy. The instrumentation system design is usually driven by the needs for parameter estimation. For the research of this thesis the instrumentation is assumed to be designed properly. The focus is on input techniques for parameter identification which have advanced from classical sine waves and doublets to optimal input techniques. The following pages define types of inputs used for parameter estimation.

#### A. SINE WAVES

Input techniques to excite the aircraft for parameter estimation did not begin until 1922 when Norton and Brown used a rolling maneuver to determine the roll control and damping coefficients of a biplane. Following in 1923, Norton used oscillations combined with static maneuvers to estimate longitudinal stability coefficients. [Ref. 1] Similar input techniques were used until the end of World War II. The development of higher performance aircraft resulted in changes in aircraft dynamics. The earlier phugoid techniques were not adequate for estimating the short period mode stability derivatives. New techniques for parameter estimation were developed to improve accuracy of the estimates of the short period motion.

In the late 1940's and early 1950's, frequency-response techniques were introduced for determining dynamic derivatives. The frequency-response technique used sine wave type oscillations as inputs. In Figure 3.1 a sine wave is shown on the left and the corresponding power spectral density on the right. An autopilot was used to input discrete frequencies over a desired range of frequencies. Measurements of the steady-state amplitude and phase angle between the control surface input and the response variable were recorded. The draw back to this approach was the large amount of flight-time required to cover the total frequency range of interest. This draw back is due to the fact that the sine wave input has very good power but an extremely narrow frequency band which can be seen in the power spectral density in Figure 3.1 on the right. If the

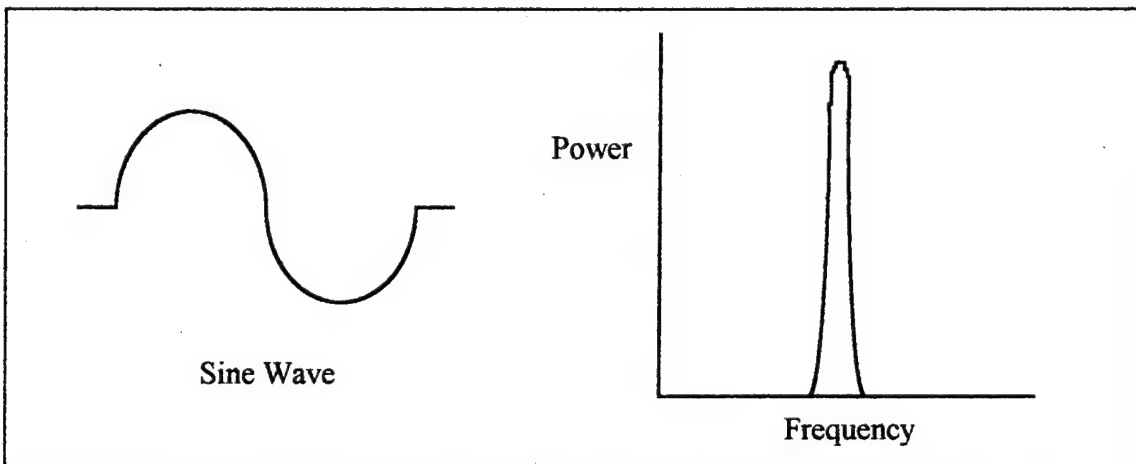


Figure 3.1. Sine Wave Input with Power versus Frequency Plot.

input frequency is not close to a natural frequency of the aircraft, excitation of the aircraft will be minimal which produces poor parameter estimates. Therefore, a large range of frequency inputs needs to be used to get good excitation and better estimates.

## B. DOUBLETS

Need for an improved input technique lead to the development of the doublet. The doublet is the most classical input technique still in use today. Shown in Figure 3.2

on the left is a square wave doublet with amplitude reversal at half the duration of the wave. A power spectral density plot is displayed on the right in Figure 3.2. The frequency band covered by a doublet is usually broad enough with enough power to excite the desired aircraft modes. Another favorable argument for the doublet is that it is

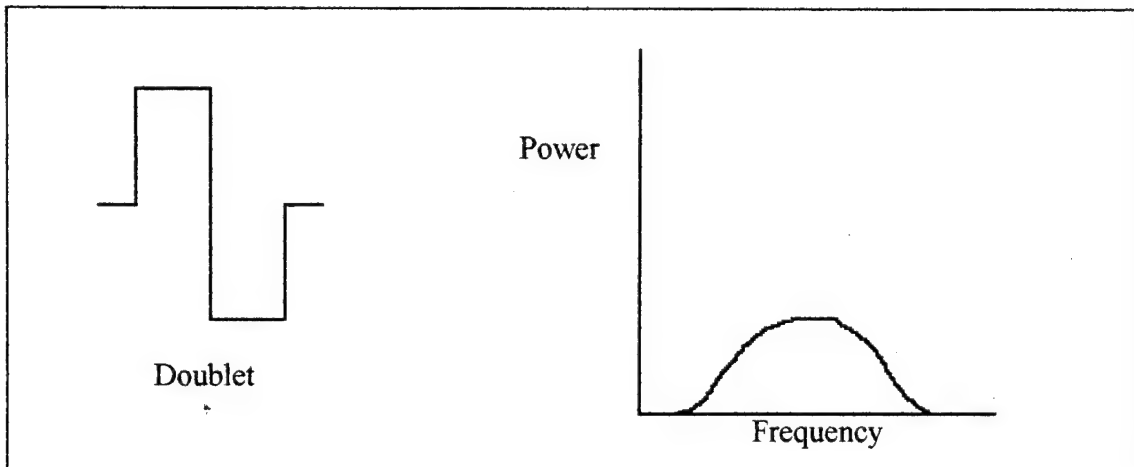


Figure 3.2. Doublet Input with Power versus Frequency Plot.

easy to fly for the pilot or auto-pilot. The doublet input technique for parameter estimation was implemented into the HARV project.

### C. DRYDEN SINGLE-SURFACE INPUTS (SSI / OBES)

Single-surface input techniques use one control surface at a time during inputs. The input technique for each surface is a doublet. Dryden flight-test engineers, Bowers and Cobleigh, developed a sequential series of single-surface inputs in attempts to increase the excitation of the system and decrease the parameter correlation. The input surfaces used correspond to the longitudinal and lateral-directional inputs discussed in Section II.B.1. The normal control law for the HARV would not permit separate control surfaces to move individually using either the pilot's stick or auto-pilot. To accomplish the desired input an On Board Excitation System (OBES) was implemented into the HARV project. The OBES software enabled preprogrammed maneuvers such as

doublets, frequency sweeps, or degradation of control power to control surfaces. The excitation system, shown in Figure 3.3, moves the control surfaces directly without moving the pilot's stick. Implementation of the degraded control power allows single surface deflection without moving any other control surface which significantly decreases the correlation of the input control surfaces. However, since the feedback term remains in the control law, some correlation is still present. A sequenced series application of degraded control power leads to the Dryden sequential-single-surface inputs shown in Figure 3.4. The input technique begins with a 4-second differential horizontal tail (DH) doublet followed by a 1-second pause. Then a 4-second rudder (DR) doublet, 1-second pause and 4-second aileron (DA) doublet are input. A 2-second pause follows the aileron input before the final 4-second thrust vectoring yaw vane (DYV) doublet is input. Note the correlation between the aileron and differential horizontal tail when the aileron is input at 11.5 seconds, and the high correlation between the thrust vectoring yaw vane and the rudder when the yaw vane is input at 17.5 seconds. The maneuver is preprogrammed into the OBES and performed during a flight-test.

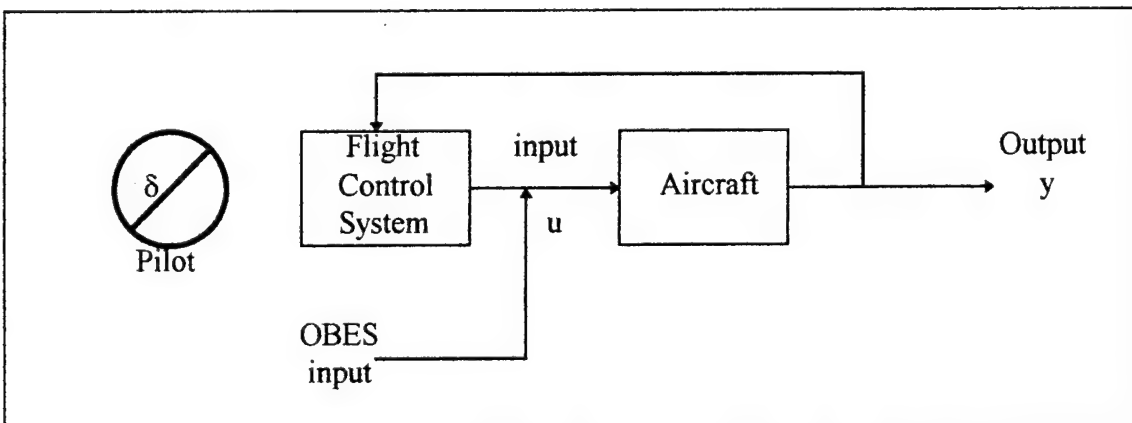


Figure 3.3. Representation of OBES Inputs with Pilot Out of the Loop.

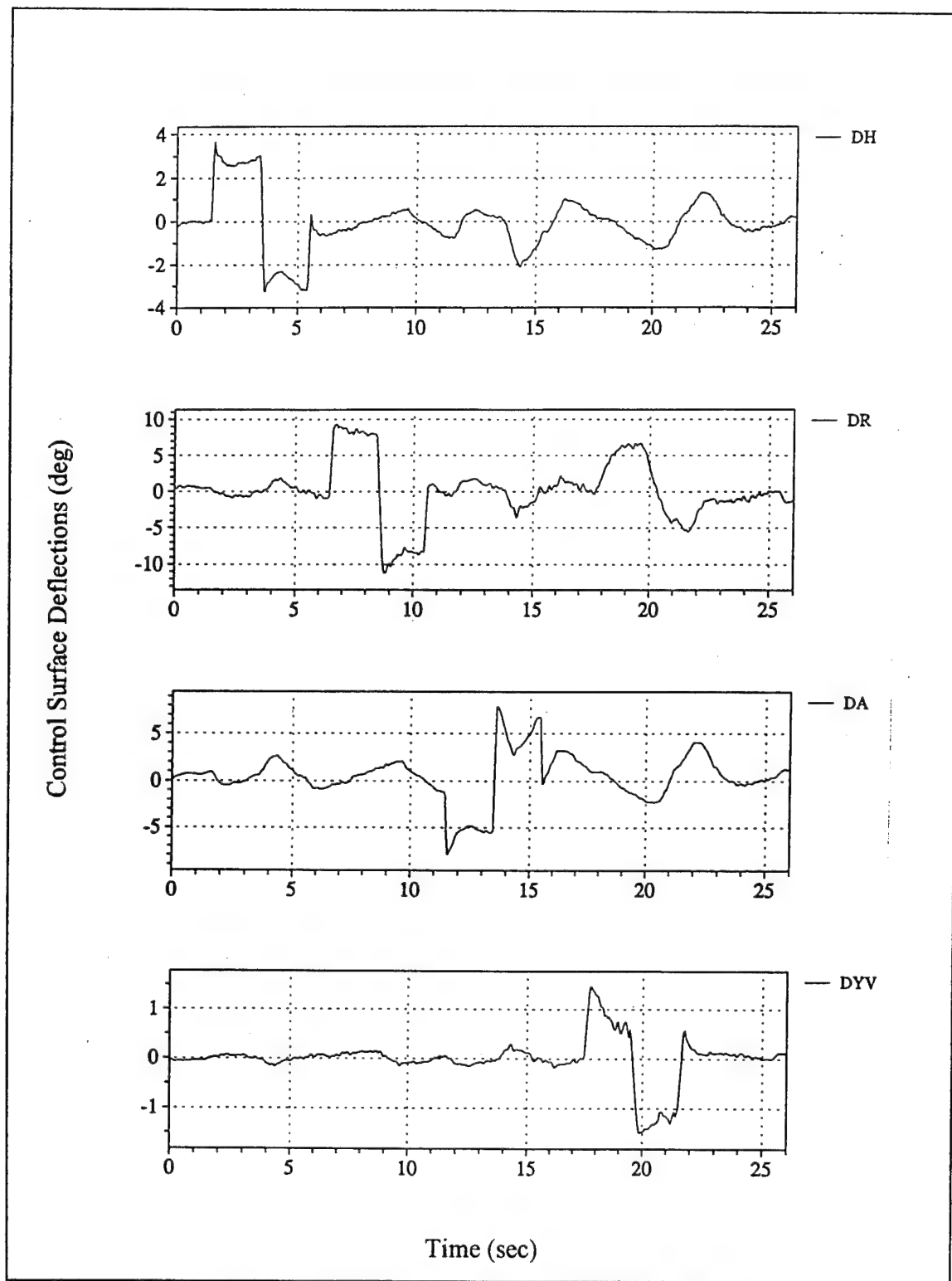


Figure 3.4. Dryden Sequential Single Surface Inputs.

#### D. OPTIMAL INPUTS

Two separate optimal input techniques were used for parameter estimation on the HARV project. The two techniques were the Klein Targeted Optimal Input Maneuvers and the Morelli Optimal Input Maneuvers. Both techniques were designed using the method of dynamic programming outlined in reference [2] and discussed later. The same optimization principles, input forms, and constraints were applied in both cases. Bellman's principal of optimality was implemented to ensure a globally time optimal input. Chen's work indicated that "bang-bang" type inputs are the most optimal. Input forms were restricted to square wave inputs of full positive, full negative or zero based on the work of Chen. [Ref. 16] Amplitude constraints on both the input and output are also imposed in the formulation of the design.

The optimization problem according to Morelli [Ref. 17] is: "*choose the input which minimizes the time to achieve the a priori desired accuracies on the parameters.*" The desired accuracies mentioned are the goals for the Cramer-Rao bounds of the parameter estimates. To achieve the stated objective, Klein and Morelli used dynamic programming to produce the needed results.

Dynamic programming is the method applied in both input techniques to obtain the desired input. An example follows to help explain the dynamic programming approach. An input is discretized into a finite number of points. Each point is called a stage time. At any given stage time, each control input is constant during that stage time. Dynamic programming begins by choosing an initial starting control input. Then the next input is determined by advancing one discretized stage at a time and computing the Cramer-Rao bound for all allowable combinations of inputs. The input at that stage time which yields the smallest Cramer-Rao bound is the optimal input, which is selected and stored at each separate stage time. After the optimal inputs at each stage time have been determined, the final input is computed by summing up all of the individual optimal inputs. The sum will be a globally time optimal input using dynamic programming. Parameter estimates determined using this input technique should have the smallest

Cramer-Rao bound possible. For a further detailed explanation of dynamic programming see reference [18].

### **1. Klein Targeted Optimal Input Maneuvers**

Klein targeted maneuvers were designed using the approach stated above for pilot implementation. Since Klein maneuvers require precise inputs to get the desired accurate estimates, visual steering commands are transmitted to the HARV using a Remotely Augmented Vehicle (RAV). The Remotely Augmented Vehicle receives a downlinked data stream from the HARV, processes the data using a computer, and sends a real time uplink steering signal to the HARV. An upgraded heads-up-display (HUD) on board the HARV, displays the RAV signal as needles to inform the pilot where to “fly-to”. The needles include an elevation deviation bar for pitch steering and an azimuth deviation bar for directional steering. Ground based simulation of the exact same maneuver prior to flight-test is conducted to ensure precise maneuvers are flown. The Klein input is shown in Figure 3.5. The figure shows the differential horizontal tail (DH) input at the top of the page followed by the rudder (DR) input and aileron (DA) input. The rudder input is anti-cyclic with the highly correlated differential horizontal tail and aileron inputs.

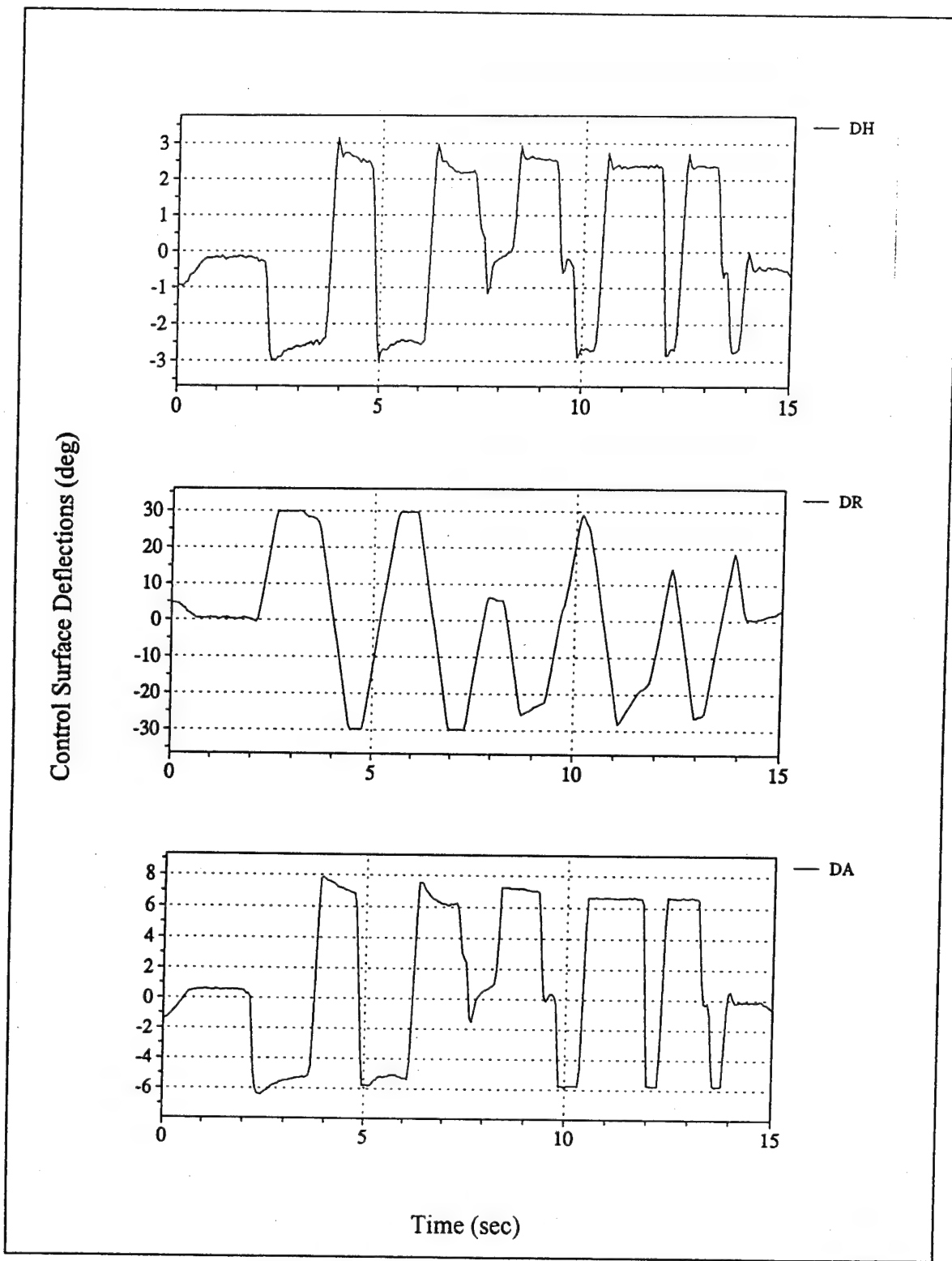


Figure 3.5. Klein Targeted Optimal Input.

## 2. Morelli Optimal Input Maneuvers

Morelli inputs were designed using the dynamic programming method already discussed in Section III.D. The difference between Morelli inputs and Klein inputs is the implementation technique. Klein maneuvers were flown by the pilot. Morelli maneuvers were flown by a computer. The same On Board Excitation System (OBES) used for the Single-Surface input technique discussed in Section III.C. is used for Morelli optimal inputs.

The maneuver is first developed using dynamic programming. The optimal input that results from the dynamic programming is then programmed into the computer which runs the On Board Excitation System. During the parameter estimation flight once the initial conditions for the maneuver have been established, the OBES system commences the series of control surface deflections without moving the pilots stick. See figure 3.4 for OBES type inputs. Figure 3.6 shows the Morelli input technique. The differential horizontal tail (DH) input is at the top of the figure followed by the rudder (DR) input and the aileron (DA) input. Any correlation that may exist with this input is difficult to see visually in the figure. The aileron (DA) input shown has the wrong sign of deflection that Morelli intended. The cause of the sign error was faulty programming of the input in the OBES software. The result is a positive aileron deflection when a negative deflection is desired.

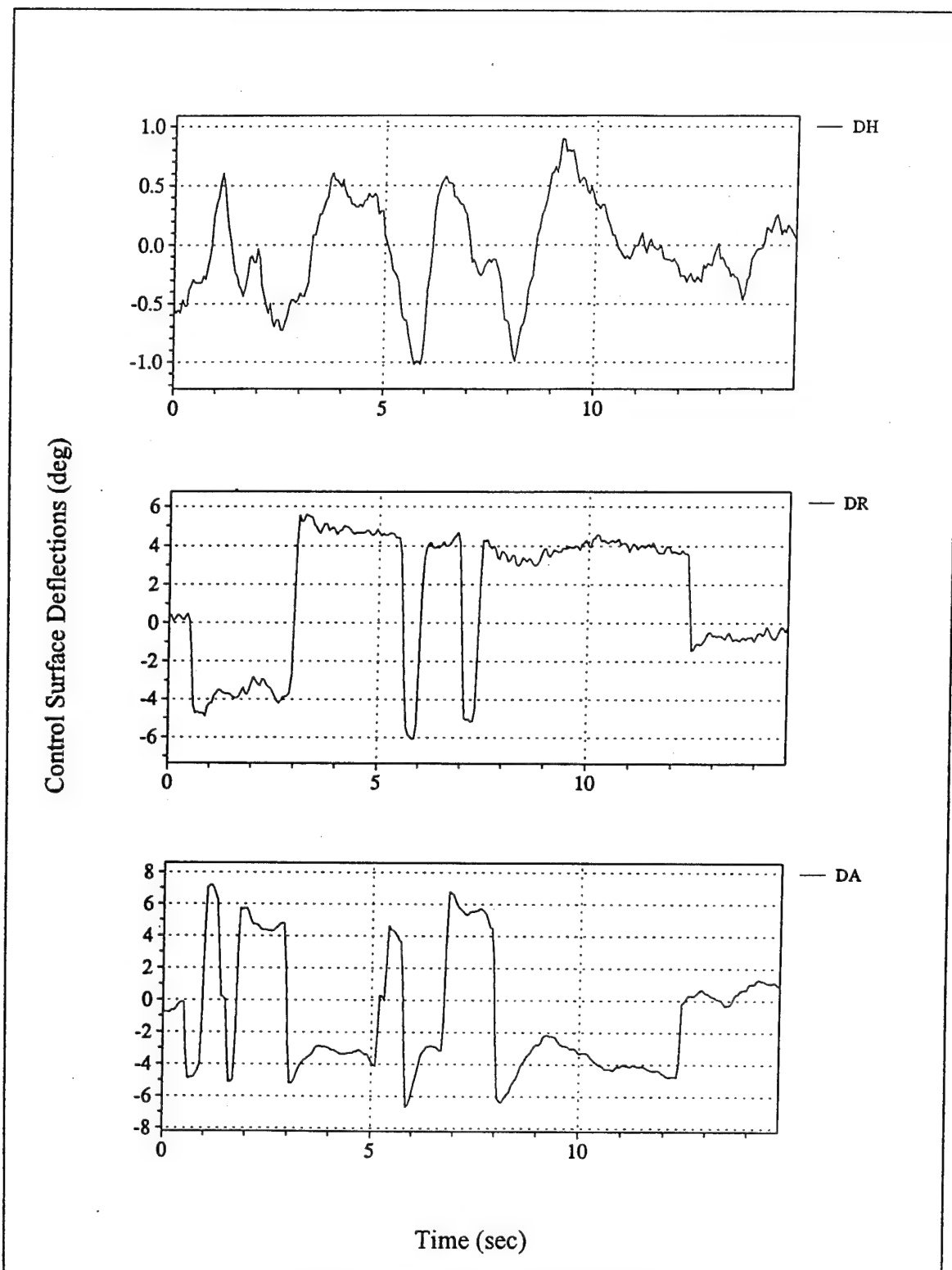


Figure 3.6. Morelli Optimal Input.

## E. 3211 DOUBLET

The "3211" doublet series is an input technique used to widen the frequency range excited by the input. Again, the input is a "bang-bang" type of input where either full positive amplitude or full negative amplitude is applied to the input control surface. Figure 3.7 shows a '3211' type of input on the left. The input signal begins with a 3 second full positive or full negative control surface deflection. At the end of 3 seconds, a full reversal in amplitude is executed and held for 2 seconds. Two more amplitude reversals are performed and held for 1 second until the signal is turned off. The duration of the control surface deflections define the '3211' input. The signal produces a larger frequency sweep with less power than a plain doublet. The power spectral density plot shown on the right of Figure 3.7 shows the large frequency range with less power.

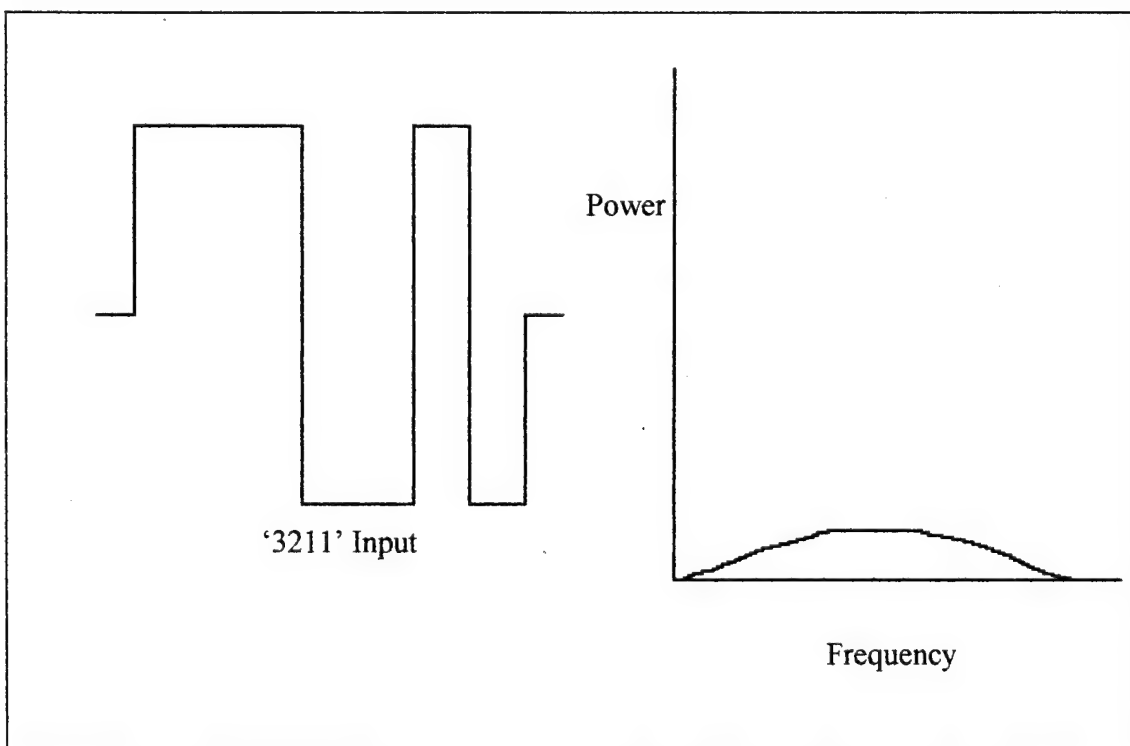


Figure 3.7. '3211' Input Technique and Power versus Frequency Plot.



## IV. COMPUTER ANALYSIS SOFTWARE

### A. FLIGHT TEST DATA

Conducting the research for this thesis required the analysis of large quantities of data. Actual flight data from HARV test flights was used for the required analysis. After a test flight was completed, the recorded time history flight data are downloaded into a main frame computer at NASA Dryden's data acquisition facility. Within an hour, data is accessible for manipulation. Manipulation of the data is made possible by applying computer software written and developed locally at NASA Dryden. Explanation of the software and further applied analysis techniques follow.

#### 1. GetFdas

The most recent software at NASA Dryden for data manipulation is GetFdas. GetFdas is the successor to the old GetData program. The flight data access system (FDAS) contains all the time history data files located at NASA Dryden. GetFdas allows local users to interface with the system and get selected time history data written to a local file. Once the data has been transferred to the local user's file, other software can be applied to analyze the data. Appendix B has a brief introduction to GetFdas commands and utilities including *measured* files, *current* files, and other applications used for this thesis.

#### 2. GetData

GetData has been replaced by GetFdas for retrieving flight test time history data. However, GetFdas cannot perform many functions that GetData was originally programmed to accomplish. Some of these functions are converting file formats, merging data from several input files, and generating calculated output signals as functions of the input signals. Converting file formats is very useful for easy user viewing of the data since the default file format is a compressed data format. The most

important function for the purpose of this thesis was the generation of calculated output signals as functions of the input signals.

The HARV is a highly augmented aircraft which uses many non-conventional input signals. Inputs like simultaneous aileron, simultaneous trailing edge flaps, elevator, and thrust vectoring inputs are non-conventional in that their time history input signals have to be generated. Only GetData has a data manipulation function which allows new signals to be generated by combining existing signals using mathematical operations. A simple HARV example follows: the simultaneous aileron input signal is generated by summing the left aileron signal and the right aileron signal then dividing by 2. This approach is an example of how all of the non-conventional input signals were generated. Appendix B contains a copy of the file used in GetData to generate all of the input signals required for this thesis.

## B. pEst

Parameter estimation begins with the selection of a parameter estimation program. The program used for this thesis was ‘pEst’. As mentioned in Section II.A, a *measured* file and *current* file are required to start the ‘pEst’ iterative process. The *measured* file is the local time history data file generated from using the data manipulation software GetFdas and GetData. The time history data includes both the measured inputs and recorded responses. The *current* file is a status file of what parameters and computed responses the user wants the program to determine. As indicated before, it is in the *current* file that a minimization method is selected and convergence tolerance is set. Using the iterative process shown in Figure 2.1, the ‘pEst’ program determines parameter estimates for the parameters selected in the *current* file.

The ‘pEst’ program can be operated in two different modes. A batch mode can be applied if a sequence of ‘pEst’ commands is defined in a separate file which, when run inside ‘pEst’, will solve the problem. However, the most frequently used mode is the interactive mode. In the interactive mode, the user is constantly interfacing with the

program through simple menu commands. These commands allow the user complete control of the 'pEst' process at any time during the solution. Whether or not the solution is converging can also be observed at each iteration in the interactive mode allowing the user the option to terminate the process. Further explanation of 'pEst' commands can be found in reference [9].

### C. UTILITY PLOTTING PROGRAM (XPlot)

'XPlot' is a utility plotting program for plotting X-Y data. Easy application is made possible through the use of Windows oriented software. The program is set up to interface well with GetData file formats and 'pEst'. A *makefile* allows the 'pEst' source code to access 'XPlot' directly from within 'pEst' by typing the command *plot*. The *makefile* is a UNIX based utility which allows a user to run a large program like 'pEst' without having to run each separate source file, object file, header file, and executable file (target files) separately. When typing *plot*, command and plot windows will appear allowing the user to view the measured and computed responses versus time. Figure 4.1 shows such a plot with THETA.1 being the measured response and THETA-HAT.2 being the computed response. Viewing these two responses graphically, shows how closely the computed response matches the measured response. This is a direct indication of the accuracy of the estimated parameters. If the accuracy is not acceptable, adjustments can be made to the response weighting matrix, while inside 'pEst', to improve the inaccuracy. The 'pEst' program can then be rerun to determine new parameter estimates. Figure 4.1 is an example of high accuracy parameter estimation.

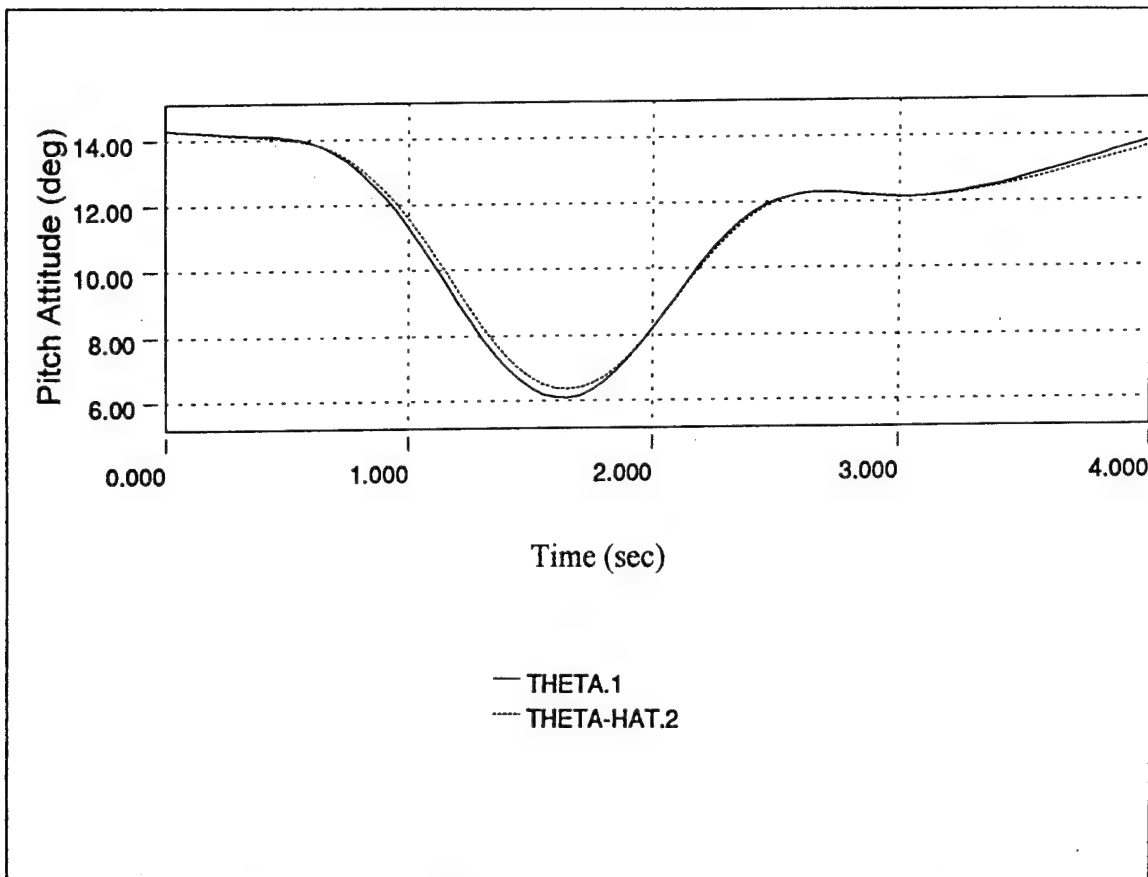


Figure 4.1. Computed Response and Measured Response versus Time.

#### D. CRAMER-RAO COMPARISONS

Since the same minimization method is applied to a single model for different input techniques, the Cramer-Rao bound is an excellent measure to use for the comparison of the results. The lower the Cramer-Rao bound, the less the standard deviation in the error, which means the more likely the estimated parameter is correct. Initial conditions for each different input technique need to be the same for the most meaningful results. These conditions include airspeed, altitude, angle-of-attack and configuration. Parameter estimates can be determined for each input technique using the recorded flight data and 'pEst'. Each parameter estimate will have a corresponding Cramer-Rao bound. Comparing like parameters Cramer-Rao bounds will indicate which input technique produces the most accurate estimates.

## E. CORRELATION MATRIX

Although the Cramer-Rao bound is the best measure of accuracy for parameter estimate comparisons, the corresponding correlation matrix for each input technique can also be used to enhance and verify the results. A 3 by 3 example of a correlation matrix is shown in Figure 4.2. The correlation matrix is a square matrix with ones along the

$$\begin{bmatrix}
 C_{m_0} & C_{m_\alpha} & C_{m_q} \\
 C_{m_0} & 1 & 0.8 & 0.03 \\
 C_{m_\alpha} & 0.8 & 1 & -0.02 \\
 C_{m_q} & 0.03 & -0.02 & 1
 \end{bmatrix}$$

Figure 4.2. Correlation Matrix.

diagonal and whose rows and columns are defined by the parameters being determined. The diagonal terms are 1 since the correlation of each parameter with itself is one. The off diagonal terms are all between -1 and 1. The closer the magnitude of the number is to 1, the more difficult the 'pEst' code has determining the difference between the two parameters. Examples from Figure 4.2, are the correlation value of 0.8 between  $C_{m_0}$  and  $C_{m_\alpha}$ , the correlation value of 0.03 between  $C_{m_0}$  and  $C_{m_q}$ , and the correlation value of -0.02 between  $C_{m_\alpha}$  and  $C_{m_q}$ . The 0.8 value is high correlation which indicates that the 'pEst' program cannot determine the difference between the results for the  $C_{m_0}$  and  $C_{m_\alpha}$  parameters. The other two values of correlation are low which indicates that the parameter value determined for  $C_{m_q}$  should be good.

Correlation is fixed in the recorded data during the test flight. Since correlation depends on the relationships between the measured inputs and the recorded outputs, then the value for correlation is fixed when the data is recorded. This fact can be used to help determine the cause of high Cramer-Rao bounds. Higher correlation will most often correspond to higher Cramer-Rao bounds. Thus, the correlation matrix can be used to indicate one reason why high Cramer-Rao bounds exist.

## V. RESULTS AND DISCUSSION

Four separate input types were used in the parameter estimation flights of the HARV aircraft. The four discrete types were: (1) Doublets; (2) Dryden Single-Surface Inputs; (3) Klein Targeted Optimal Input Maneuvers; and (4) Morelli Optimal Input Maneuvers. Each type of input was used at several angles of attack. These inputs can be further separated into either longitudinal inputs or lateral-directional inputs which produce the corresponding longitudinal or lateral-directional motion response. Longitudinal parameters are selected for determination when a longitudinal input is used for the motion response, and lateral-directional parameters are selected for determination when a lateral-directional input is used for the motion response.

Data recorded from the flights is stored in the flight data access system (FDAS) at NASA Dryden Flight Research Center. The flight data manipulation tools, 'GetFdas' and 'GetData', were used to retrieve and format the flight data producing a *measured* file used in the further analysis. The parameter estimation program, 'pEst', was then used to determine parameter estimates of the HARV stability and control derivatives. A *current* file is used to begin the 'pEst' iterative process by initializing all of the parameters selected to be determined. The *current* file also contains the output weight factors and the convergence tolerance which were used to determine parameters in this thesis. The weight factors set in the *current* file depended on whether a longitudinal maneuver or lateral-directional maneuver was performed. The weight factors were determined by comparing how well the computed response matched the measured response for a large selection of different weight values. Resulting weight factors used for the output responses of longitudinal maneuvers were 4.5 for angle of attack ( $\alpha$ ), 20 for pitch rate ( $q$ ), 7 for pitch attitude ( $\theta$ ), and 45 for normal acceleration ( $a_n$ ). For the lateral directional maneuvers, the weight factors applied were 3 for sideslip angle ( $\beta$ ), 1 for roll rate ( $p$ ), 3 for yaw rate ( $r$ ), 1 for roll attitude ( $\phi$ ), and 30 for lateral acceleration ( $a_y$ ). The

default convergence tolerance of 0.0001 was used to stop the iterative process for all estimated parameters in this thesis.

In addition to parameter estimates, the 'pEst' program also determines the computed response of the model and computes the Cramer-Rao bound of each estimate. Flight data from each separate type of input for all the angles of attack were analyzed using the same optimization procedure to produce Cramer-Rao bounds for all maneuvers. A smaller Cramer-Rao bound implies a more accurate parameter estimate for any given parameter. The type of input which produces the smallest Cramer-Rao bound is the most desirable input. Only the most accurate results from each separate type of input for a given angle of attack are used for comparison studies. For the analysis of the 20 and 25 degrees angle of attack flight data, a linear relationship was assumed between the differences in angle of attack and Cramer-Rao bound results.

#### A. LONGITUDINAL PARAMETERS

The longitudinal parameters are the coefficients of the X-force (axial force), Z-force (normal force), and M-Moment (pitching moment) equations found and defined in Appendix A. Control surfaces used in the model implemented by 'pEst' for the longitudinal control inputs were elevator, trailing edge flaps, simultaneous aileron, and thrust vectoring pitch vanes. Only the Dryden Single-Surface input used the simultaneous aileron control surface. Therefore, parameters based on simultaneous aileron deflection ( $\delta_{as}$ ) were determined only from the Dryden Single-Surface input which makes comparison studies for parameters determined from this deflection not feasible. The Klein Targeted Optimal Inputs did not use the research flight control system (RFCS) which enables thrust vectoring. Thus, the  $C_{\delta p_v}$  parameter based on pitch vane deflection was not determined from the Klein inputs.

The longitudinal parameters used in the comparisons of Cramer-Rao bounds were based on seven different flights. Table 5.1 list the seven flights according to angle of attack, input type, and flight number. Two flights were at 20 degrees angle of attack, two

flights were at 25 degrees angle of attack, and three flights were at 30 degrees angle of attack. Since not all input techniques were used at each separate angle of attack, some conclusions must be inferred.

AOA	20 Alpha		25 Alpha		30 Alpha		
	Doublets	Klein OIM	Klein OIM	Dryden SSI	Doublets	Morelli OIM	Dryden SSI
Flight #>>>	116.5	153.2	156.1	167.1	116.7	165.2	166.3

Table 5.1. Longitudinal Flights Used for Cramer-Rao Bound Comparisons.

In general, a Cramer-Rao bound of the same parameter will be smaller for a lower angle of attack. What this statement implies is that if two Cramer-Rao bounds of the same parameter from two different flights are equal but the angle of attack of each flight are not equal, then the Cramer-Rao bound from the flight with the higher angle of attack is theoretically smaller than the Cramer-Rao bound from the flight with the lower angle of attack even though numerically the numbers are equal. Since the Cramer-Rao bound from the higher angle of attack flight is theoretically smaller, the implication is that the corresponding parameter is more accurate. The same inference must be applied in cases where similar results occur. In the next three sections the longitudinal results for the axial force parameters, normal force parameters, and pitching moment parameters are given.

## 1. X-Force (axial)

### a. Results for 20 and 25 Degrees Angle of Attack

The final results for the axial force parameters Cramer-Rao bounds for 20 and 25 degrees angle of attack are listed in Table 5.2. Axial force parameters are the coefficients  $C_{A_0}$ ,  $C_{A_\alpha}$ ,  $C_{A_q}$ ,  $C_{A_{\delta_e}}$ ,  $C_{A_{\delta_{ref}}}$ , and  $C_{A_{\delta_{as}}}$  from the axial force equation (Appendix A equation A.9). These parameters are specified in the left column of Table 5.2 with their corresponding Cramer-Rao bounds entered for each separate flight across

the row.  $C_{A_q}$  is a very weak parameter which is extremely hard to estimate. For that reason, no effort was made to determine  $C_{A_q}$  for any type of input.

	20 Alpha		25 Alpha	
	Doublets	Klein OIM	Klein OIM	Dryden SSI
$C_{A_0}$	1.506	0.1304	0.3727	0.1071
$C_{A_\alpha}$	8.51E-02	4.95E-03	1.13E-02	3.82E-03
$C_{A\delta_e}$	4.31E-02	4.33E-03	9.36E-03	3.17E-03
$C_{A\delta_{tef}}$	4.04E-02	6.10E-03	4.60E-02	6.15E-03

Table 5.2. Axial Force Parameters Cramer-Rao Bounds at 20 & 25 Degrees Angle of Attack.

Except for the first, each column of Table 5.2 corresponds to a separate flight. The first two flights are at 20 degrees angle of attack, followed by two flights at 25 degrees angle of attack. For comparison purposes, the 20 degree and 25 degree angles of attack are analyzed together.

$C_{A_0}$  is the aerodynamic bias parameter. The Cramer-Rao bounds for  $C_{A_0}$  for the 20 and 25 degree angle of attack inputs, show an order of magnitude difference between the optimal type inputs (Klein and Dryden) Cramer-Rao bounds and the conventional doublet input. As expected, the Cramer-Rao bound for  $C_{A_0}$  from the Klein input at 25 degrees angle of attack is larger than the Cramer-Rao bound for  $C_{A_0}$  from the Klein input at 20 degrees angle of attack. The Dryden input Cramer-Rao bound for  $C_{A_0}$  is the smallest bound of the four  $C_{A_0}$  bounds shown in Table 5.2.

$C_{A_\alpha}$  is the change in axial force caused by a change in angle of attack parameter. Again, Table 5.2 shows the doublet inputs Cramer-Rao bound for  $C_{A_\alpha}$  is an order of magnitude higher than the optimal inputs (Klein and Dryden) Cramer-Rao

bounds for  $C_{A_a}$ . Also, the Cramer-Rao bound for  $C_{A_a}$  from the Klein input at 25 degrees angle of attack is, once more, greater than the Cramer-Rao bound for  $C_{A_a}$  from the Klein input at 20 degrees. In fact, Table 5.2 shows that all of the Cramer-Rao bounds of like parameters from the Klein input at 25 degrees are greater than the Cramer-Rao bounds from the Klein input at 20 degrees. The smallest Cramer-Rao bound shown in Table 5.2 for  $C_{A_a}$  came from the Dryden single-surface input.

$C_{A_{\delta e}}$  is the change in axial force due to a change in elevator deflection parameter. Table 5.2 shows that for  $C_{A_{\delta e}}$  the largest Cramer-Rao bound is from the doublet input and the smallest Cramer-Rao bound is from the Dryden single-surface input.

The last axial force parameter which is compared for the 20 and 25 degree angles of attack is  $C_{A_{\delta ef}}$  which is the change in axial force due to a change in trailing edge flap deflection. Table 5.2 shows that the Klein input at 25 degrees angle of attack has the largest Cramer-Rao bound for  $C_{A_{\delta ef}}$ . However, the Klein input at 20 degrees angle of attack has a Cramer-Rao bound for  $C_{A_{\delta ef}}$  which is 0.00005 smaller than that from the Dryden single surface input at 25 degrees angle of attack. The percentage difference between these two parameters is less than 0.82% while the angle of attack difference is 20%. Therefore as explained in the longitudinal parameters introduction, the Cramer-Rao bound for  $C_{A_{\delta ef}}$  from the Dryden single surface input at 25 degrees angle of attack is theoretically smaller than that from the Klein input, implying that the resulting  $C_{A_{\delta ef}}$  parameter for the Dryden single surface input case is expected to be more accurate.

Figure 5.1 shows the results referred to in the above paragraphs for the axial force parameters Cramer-Rao bounds determined from flights at 20 and 25 degrees angles of attack in a bar graph format. The  $C_{A_0}$  Cramer-Rao bounds are numerically too

large to be plotted in the same figure. The X-axis represents each axial force parameter, and the Y-axis represents the Cramer-Rao bound value. Each axial force has four bars which specify the type of input which is given in the legend inside the figure.

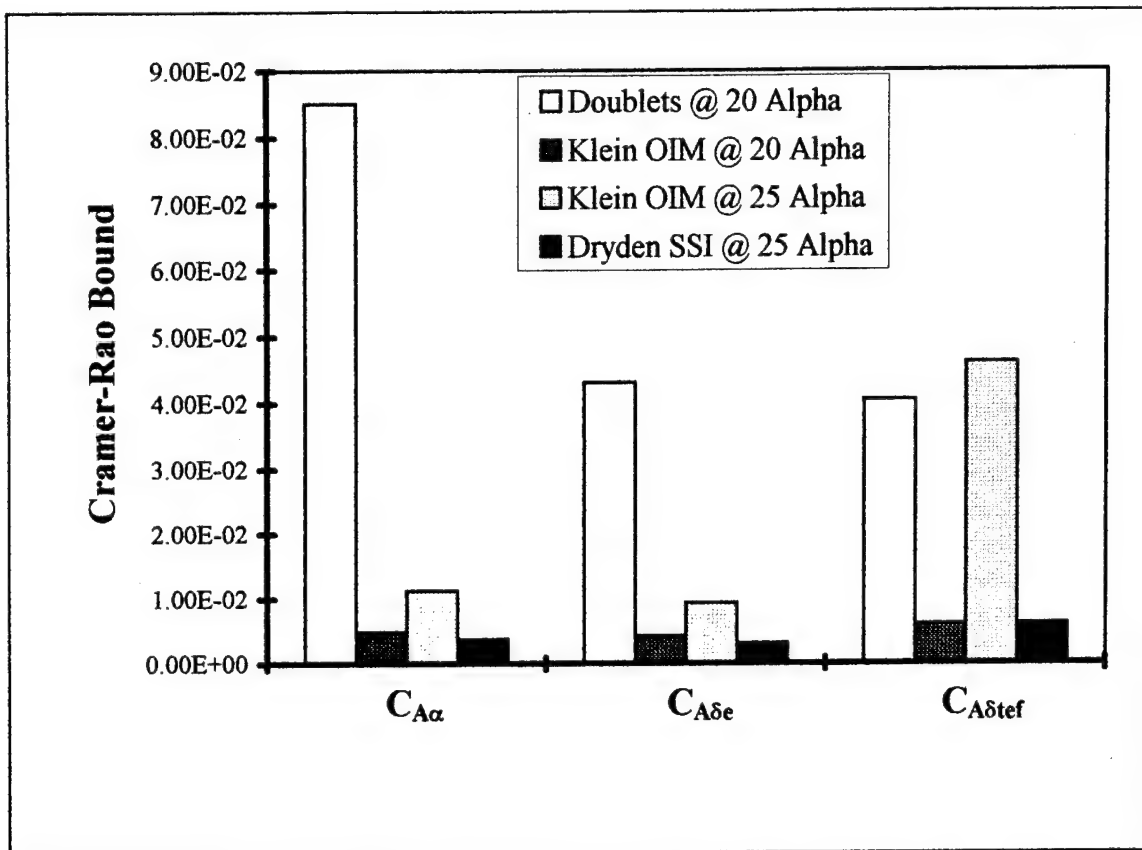


Figure 5.1. Axial Force Parameters Cramer-Rao Bounds at 20 & 25 Degrees Angle of Attack.

#### b. Results for 30 Degrees Angle of Attack

The results for the axial force parameters Cramer-Rao bounds from the 30 degree angle of attack flights are shown in Table 5.3. Table 5.3 is arranged in the same manner as Table 5.2 with the parameters listed on the left, and the respective Cramer-Rao bounds listed across each row according to type of input.

Table 5.3 shows that for all the parameters except the aerodynamic bias,  $C_{A_0}$ , the Cramer-Rao bounds get smaller from left to right. For the aerodynamic bias, the Morelli input has the smallest Cramer-Rao bound by 17.5% over the Dryden single-surface inputs. It is thought that there were two reason for this, first, there may be more noise in the measured signal for the Dryden single-surface flight which is added directly to the bias term. Second, Morelli inputs were found to have higher correlation than Dryden inputs, and

		30 Alpha	
	Doublets	Morelli OIM	Dryden SSI
$C_{A_0}$	1.357	0.5539	0.6511
$C_{A\alpha}$	3.34E-02	1.67E-02	1.39E-02
$C_{A\delta_e}$	1.99E-02	1.18E-02	7.25E-03
$C_{A\delta_{tef}}$	7.68E-02	6.41E-02	2.02E-03

Table 5.3. Axial Force Parameters Cramer-Rao Bounds  
at 30 Degrees Angle of Attack.

some of the bias effects could be placed into the highly correlated parameters rather than the aerodynamic bias. In general, the Cramer-Rao bounds for the axial force parameters determined from the Dryden single-surface inputs were the smallest.

Figure 5.2 displays the axial force parameters Cramer-Rao bounds at 30 degrees angle of attack using the same bar graph form of Figure 5.1. The axial force parameters are separated along the X-axis with their respective Cramer-Rao bound on the Y-axis. In Figure 5.2, the decreasing Cramer-Rao bounds are easily depicted for the different types of inputs listed in the legend. As a general statement for the 20 and 25 degree angle of attack flights and the 30 degree flights, the Cramer-Rao bounds of the axial parameters determined from the Dryden single-surface inputs are, in most cases, the

smallest. This result implies that the Dryden axial force parameters are expected to be the most accurate.

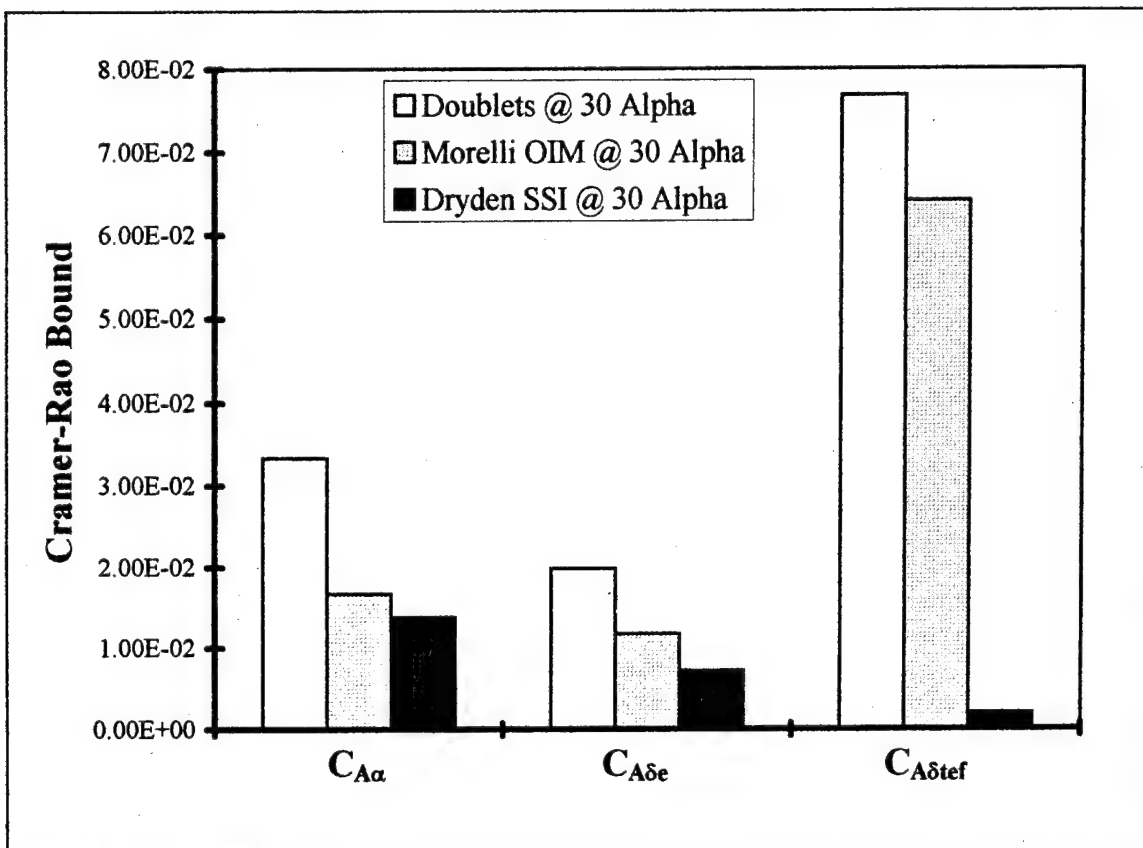


Figure 5.2. Axial Force Parameters Cramer-Rao Bounds at 30 Degrees Angle of Attack.

## 2. Z-Force (normal)

### a. Results from 20 and 25 Degrees Angle of Attack

The results for the normal force parameters Cramer-Rao bounds from the 20 & 25 degrees angle of attack flights are listed in Table 5.4. Normal force parameters are the coefficients  $C_{N_0}$ ,  $C_{N_\alpha}$ ,  $C_{N_q}$ ,  $C_{N_{\delta_e}}$ ,  $C_{N_{\delta_{ef}}}$ ,  $C_{N_{\delta_{as}}}$ , and  $C_{\delta p_v}$  from the normal force equation (Appendix A, equation A.10). These parameters are specified in the left column of Table 5.4 with their corresponding Cramer-Rao bounds entered for

each separate flight across the row. At the top of the table for each column are the angle of attack and type of input.

	20 Alpha		25 Alpha	
	Doublets	Klein OIM	Klein OIM	Dryden SSI
$C_{N_0}$	0.1527	0.1442	9.55E-02	7.52E-02
$C_{N\alpha}$	2.68E-03	4.76E-03	3.66E-03	2.69E-03
$C_{Nq}$	6.905	11.89	9.242	8.569
$C_{N\delta e}$	1.56E-03	2.04E-03	1.60E-03	1.26E-03
$C_{N\delta tef}$	2.84E-03	5.92E-03	1.27E-02	4.63E-03
$C_{\delta p v}$	4.53E-03	~~~	~~~	7.37E-04

Table 5.4. Normal Force Parameters Cramer-Rao Bounds at 20 & 25 Degrees Angle of Attack.

The first parameter in Table 5.4 is the normal force aerodynamic bias,  $C_{N_0}$ . The improvement of the Cramer-Rao bound from the doublet input to the Dryden single-surface input is 50.8%.

The next parameter in Table 5.4 is  $C_{N\alpha}$  which is the parameter for the change in normal force due to a change in angle of attack. In Table 5.4, the doublet input at 20 degrees angle of attack has a Cramer-Rao bound for  $C_{N\alpha}$  that is .00001 less than the Cramer-Rao bound for  $C_{N\alpha}$  from the Dryden single-surface input at 25 degrees angle of attack. The percentage difference between these two parameters is less than 0.38% while the angle of attack difference is 20%. Therefore, as in the example case given in the longitudinal parameters introduction, the Dryden single-surface input's Cramer-Rao bound is theoretically smaller by 19.6%, which implies that the  $C_{N\alpha}$  parameter from the Dryden input is expected to be more accurate.

$C_{N_q}$  is the change in normal force due to a change in the pitch rate. The doublet input has the smallest Cramer-Rao bound for  $C_{N_q}$  of the four inputs. The difference between the Dryden Cramer-Rao bound for  $C_{N_q}$  and the doublets Cramer-Rao bound for  $C_{N_q}$  is 19.4%. While the difference in angle of attack remains at 20% for the two bounds. Therefore, a fair estimation is that the two Cramer-Rao bounds are approximately equal, or that their respective parameters are of equal accuracy.

$C_{N_{\delta e}}$  is the parameter for the change in the normal force due to a change in the deflection of the elevator control surface. Table 5.4 shows the improvement of the Cramer-Rao bound for  $C_{N_{\delta e}}$  from the Klein optimal input at 25 degrees angle of attack to the Dryden single-surface input is 21.3%.

$C_{N_{\delta e f}}$  is the parameter for the change in the normal force due to the change in deflection of the trailing edge flaps. Table 5.4 shows that the Cramer-Rao bound for  $C_{N_{\delta e f}}$  from the doublet input at 20 degrees angle of attack is 38.7% less than the Cramer-Rao bound for  $C_{N_{\delta e f}}$  of the Dryden single-surface input at 25 degrees angle of attack. The angle of attack difference is only 20%. Therefore the smallest Cramer-Rao bound for  $C_{N_{\delta e f}}$  comes from the doublet input.

$C_{\delta p v}$  is the parameter for the change in deflection of thrust due to the change of the pitch vanes. This is a unique parameter in that the addition of the thrust vectoring pitch vanes effect both the normal force and pitching moment equations. However, the actual parameter in the model is defined to determine how much change in thrust direction there is for the deflection change of the pitch vanes. Therefore, only one parameter is used in the model with the appropriate moment arm multiplier used in the moment equation (see equations 10 and 11 in Appendix A). Only the doublet input and Dryden single-surface input used the pitch vane deflection input. Table 5.4 shows the Cramer-Rao bound for  $C_{\delta p v}$  from the Dryden single-surface input is an order of

magnitude better than the Cramer-Rao bound for  $C_{\delta_{pv}}$  from the doublet input. This is most likely due to the high correlation between the elevator and pitch vane deflections in the doublet input not seen in the Dryden single-surface input.

Figure 5.3 is a bar graph representation of the Cramer-Rao bounds from Table 5.4 excluding  $C_{N_0}$  and  $C_{N_q}$ . The figure is arranged with the normal force parameters along the X-axis, and the respective Cramer-Rao bounds along the Y-axis. For each normal force parameter, there exists two or four different Cramer-Rao bounds corresponding to the different type of inputs listed in the legend.

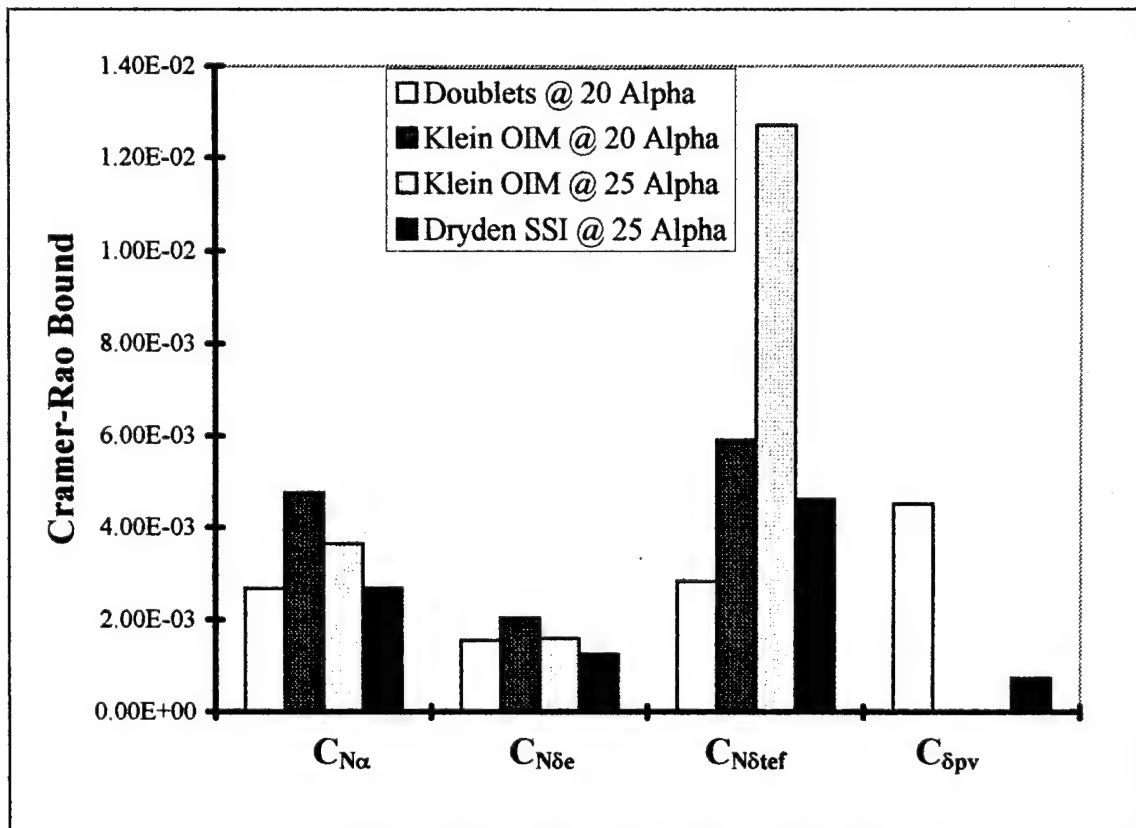


Figure 5.3. Normal Force Parameters Cramer-Rao Bounds at 20 & 25 Degrees Angle of Attack.

### b. Results from 30 Degrees Angle of Attack

The results for the normal force parameter Cramer-Rao bounds from the 30 degree angle of attack flights are shown in Table 5.5. Table 5.5 is arranged using the same format as Table 5.4 with the normal force parameters listed in the left column, and the respective Cramer-Rao bounds listed across each row according to the type of input.

	30 Alpha		
	Doublts	Morelli OIM	Dryden SSI
$C_{N_0}$	0.3555	1.43E-01	0.1706
$C_{N_\alpha}$	5.36E-03	5.28E-03	2.82E-03
$C_{N_q}$	12.33	16.96	11.53
$C_{N\delta_e}$	3.55E-03	1.75E-03	2.07E-03
$C_{N\delta_{ef}}$	1.77E-02	1.76E-02	8.83E-04
$C_{\delta_{pv}}$	4.84E-03	2.70E-03	5.73E-04

Table 5.5. Normal Force Parameters Cramer-Rao Bounds at 30 Degrees Angle of Attack.

In Table 5.5 the parameters  $C_{N_0}$  and  $C_{N_q}$  have much larger Cramer-Rao bounds than the other parameters. The  $C_{N_0}$  Cramer-Rao bound is smallest for the Morelli optimal input which is a 58.8% improvement over the doublet input and a 16.2% improvement over the Dryden single-surface input. The  $C_{N_q}$  Cramer-Rao bound is smallest for the Dryden single-surface input which is a 32% improvement over the Morelli optimal input and a 6.5% improvement over the doublet technique.

The Cramer-Rao bounds for the remaining normal force parameters are much smaller than the bounds seen for  $C_{N_0}$  and  $C_{N_q}$ . The remaining parameters are  $C_{N_\alpha}$ ,  $C_{N_{\delta_e}}$ ,  $C_{N_{\delta_{ef}}}$ , and  $C_{\delta_{pv}}$ . Table 5.5 shows that the Cramer-Rao bounds

associated with the Dryden single-surface input are smallest for all of these remaining parameters except  $C_{N_{\delta e}}$ . The smallest Cramer-Rao bound for  $C_{N_{\delta e}}$  is from the Morelli optimal input which is a 15.5% improvement over the Dryden single-surface input Cramer-Rao bound.

Figure 5.4 uses bar graphs to show the results explained above.  $C_{N_0}$  and  $C_{N_q}$  are not plotted for scaling purposes. The figure lists the parameters along the X-axis with their respective Cramer-Rao bound on the Y-axis. Each parameter has three Cramer-Rao bounds corresponding to the three different types of inputs shown in the legend.

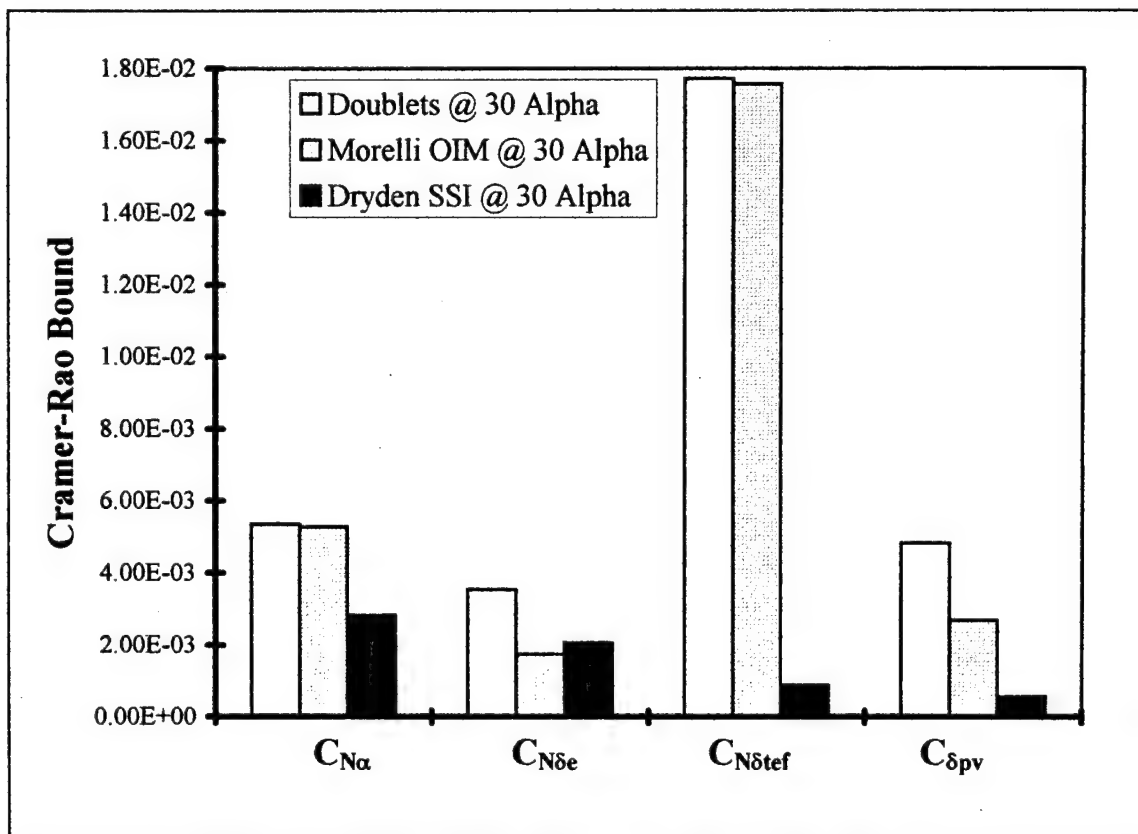


Figure 5.4. Normal Force Parameters Cramer-Rao Bounds at 30 Degrees Angle of Attack.

The doublet input technique is very effective for determining normal force parameters at lower angles of attack. However, as the angle of attack increases past 20 degrees, optimal input techniques produce smaller Cramer-Rao bound by an order of magnitude. The Dryden single-surface input produced the smallest Cramer-Rao bounds for four of six parameters.

### 3. m-Moment (pitch)

#### a. Results from 20 and 25 Degrees Angle of Attack

Results for the pitching moment parameters Cramer-Rao bounds from the 20 and 25 degrees angle of attack flights are listed in Table 5.6. Pitching moment parameters are the coefficients  $C_{m_0}$ ,  $C_{m_\alpha}$ ,  $C_{m_q}$ ,  $C_{m_{\delta e}}$ ,  $C_{m_{\delta e f}}$ , and  $C_{m_{\delta a s}}$  from the pitching moment equation (Appendix A equation A.11). These parameters are listed in the left column of Table 5.6 with their respective Cramer-Rao bounds entered across the row for each corresponding flight. At the top of the table for each column are the angle of attack and type of input.

	20 Alpha		25 Alpha	
	Doublets	Klein OIM	Klein OIM	Dryden SSI
$C_{m_0}$	1.39E-03	6.58E-03	2.14E-03	1.65E-03
$C_{m_\alpha}$	1.43E-04	2.18E-04	7.60E-05	5.88E-05
$C_{m_q}$	0.8873	0.5674	0.2961	0.1623
$C_{m_{\delta e}}$	4.49E-04	8.80E-05	4.88E-05	4.48E-05
$C_{m_{\delta e f}}$	1.65E-04	2.65E-04	3.71E-04	8.14E-05

Table 5.6. Pitching Moment Parameters Cramer-Rao Bounds at 20 & 25 Degrees Angle of Attack.

The first parameter listed in Table 5.6 is the pitching moment aerodynamic bias  $C_{m_0}$ . The Cramer-Rao bound for  $C_{m_0}$  for the doublet input at 20

degrees angle of attack is 15.8% less than that for  $C_{m_0}$  for the Dryden single-surface input at 25 degrees angle of attack, but the difference between the angle of attack is 20%. Therefore, the Cramer-Rao bound for  $C_{m_0}$  from the Dryden single-surface input, in theory, is approximately equal to that from the doublet input.

$C_{m_\alpha}$  is the change in pitching moment due to a change in angle of attack.

The smallest Cramer-Rao bound for  $C_{m_\alpha}$  in Table 5.6 is from the Dryden single-surface input. The bound is 22.6% less than the Cramer-Rao bound for  $C_{m_\alpha}$  from the Klein optimal input at 25 degrees angle of attack.

The next parameter,  $C_{m_q}$ , is the change in pitching moment due to a change in pitch rate. Table 5.6 shows that the Cramer-Rao bound for  $C_{m_q}$  from the Dryden single-surface input is an 81.7% improvement over that for  $C_{m_q}$  from the doublet input.

$C_{m_\epsilon}$  is the change in pitching moment due to a change in the deflection of the elevator control surface. Table 5.6 shows the smallest Cramer-Rao bound for  $C_{m_\epsilon}$  is from the Dryden single-surface input. The bound is an 8.2% improvement over the Cramer-Rao bound for  $C_{m_\epsilon}$  from the Klein optimal input at 25 degrees angle of attack.

The last longitudinal parameter of interest is  $C_{m_{\alpha_{ef}}}$ , which is the change in pitching moment due to the change in deflection of the trailing edge flaps. The smallest Cramer-Rao bound listed in table 5.6 for the  $C_{m_{\alpha_{ef}}}$  parameter is associated with the Dryden single-surface input. This bound is 50.7% less than the next smallest bound associated with the doublet input.

Figure 5.5 represents the Cramer-Rao bound for the pitching moment parameters for 20 and 25 degrees angle of attack flights. The same bar graph format is

used to display the results.  $C_{m_0}$  and  $C_{m_q}$  are not plotted since they are numerically too large. The X-axis lists the pitching moment parameters, and the Y-axis is the respective Cramer-Rao bounds. Each parameter has four Cramer-Rao bounds corresponding to the four different types of inputs shown in the legend.

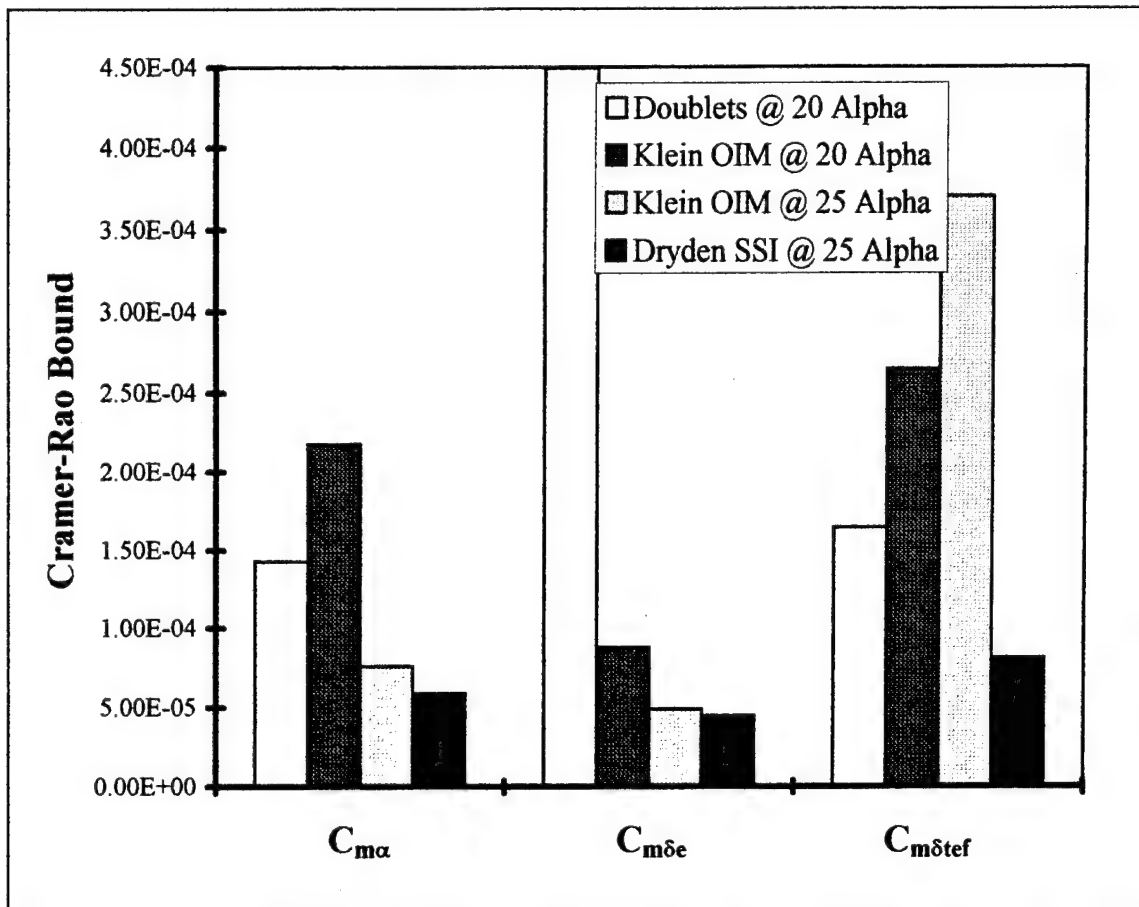


Figure 5.5. Pitching Moment Parameters Cramer-Rao Bounds at 20 & 25 Degrees Angle of Attack.

For the pitching moment parameters, the smallest Cramer-Rao bound was always associated with the Dryden single-surface input. Even for the case of  $C_{m_0}$ , when the actual numerical value of the Cramer-Rao bound was larger than the doublets

Cramer-Rao bound, the angle of attack difference negated the smaller number. Therefore, the most accurate parameters come from the Dryden single-surface input.

### b. Results from 30 degrees Angle of Attack

The results for the pitching moment parameters Cramer-Rao bounds from the 30 degree angle of attack flights are listed in Table 5.7. Table 5.7 is arranged in the same manner as Table 5.6 with the pitching moment parameters listed in the left column and the respective Cramer-Rao bounds listed across each row according to type of input.

30 Alpha			
	Doublts	Morelli OIM	Dryden SSI
$C_{m_0}$	1.33E-02	5.61E-03	1.25E-03
$C_{m_a}$	6.65E-04	1.90E-04	3.93E-05
$C_{m_q}$	1.128	0.5406	0.2304
$C_{m_{\delta_e}}$	1.25E-03	8.69E-05	4.72E-05
$C_{m_{\delta_{lef}}}$	1.64E-03	4.70E-04	1.02E-05

Table 5.7. Pitching Moment Parameters Cramer-Rao Bounds at 30 Degrees Angle of Attack.

All the Cramer-Rao bounds listed in Table 5.7 decrease from left to right for each pitching moment parameter. The smallest Cramer-Rao bound decrease between the Morelli optimal input and the Dryden single-surface input is 45.7% in the  $C_{m_{\delta_e}}$  parameter. The difference in Cramer-Rao bounds for the rest of the parameters is greater than 57% in all cases. Thus the Dryden single-surface input produced the most accurate pitching moment parameters.

Figure 5.6 shows the decreasing pitching moment Cramer-Rao bounds for the 30 degree angle of attack flights.  $C_{m_0}$  and  $C_{m_q}$  are not plotted due to their numerical size. In Figure 5.6, the pitching moment parameters are across the X-axis versus their

respective Cramer-Rao bounds on the Y-axis. Each parameter has three Cramer-Rao bounds corresponding to the three different types of inputs shown in the legend. The Cramer-Rao bounds associated with the Dryden single-surface input technique are the smallest for all three parameters shown.

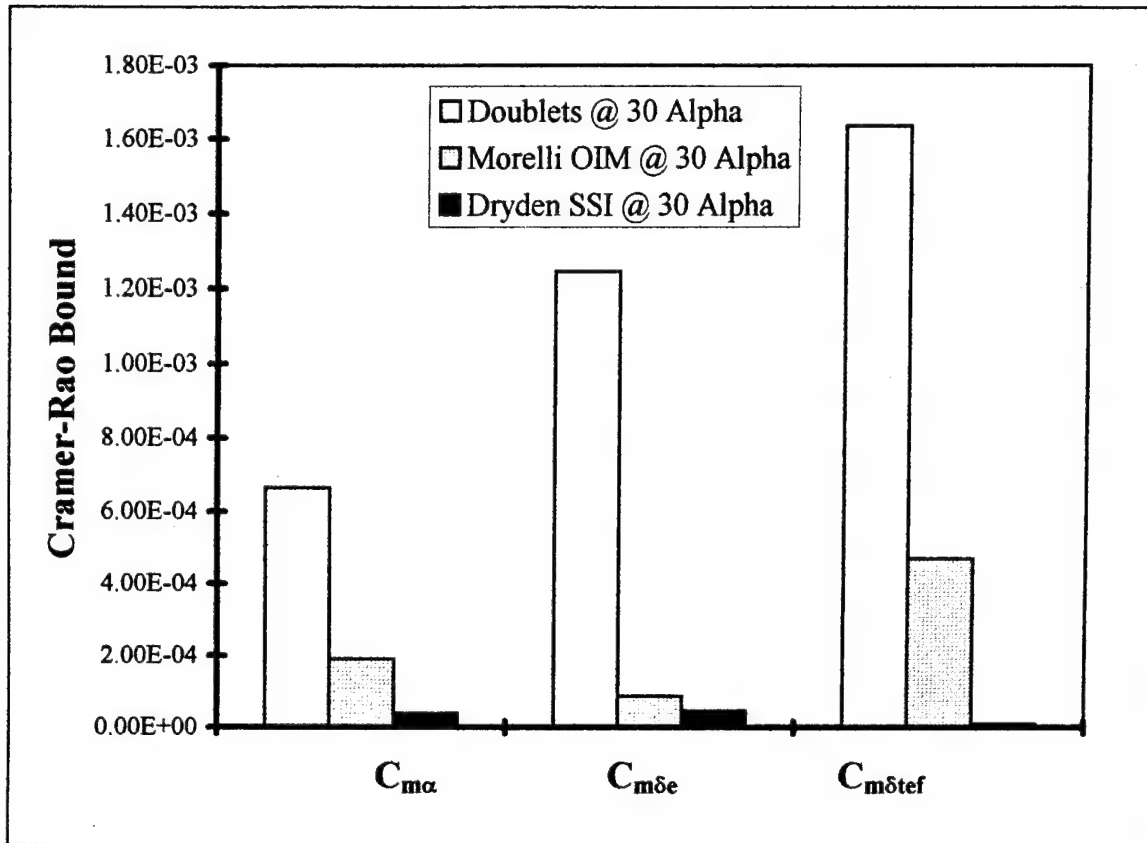


Figure 5.6. Pitching Moment Parameters Cramer-Rao Bounds at 30 Degrees Angle of Attack.

#### 4. Longitudinal Parameters Summary

In summary, of the 16 longitudinal parameters Cramer-Rao bounds compared for the 20 and 25 degree angle of attack cases, 13 of the Cramer-Rao bound were smallest from the Dryden single-surface input. Two of 16 Cramer-Rao bounds,  $C_{N\alpha}$  and  $C_{A_{\alpha\text{ref}}}$ , were approximately equal for the Dryden single-surface input and for the doublet

input. In one case, the Cramer-Rao bound from the doublet input was the smallest ( $C_{N_{\delta e_f}}$ ). A reason the bound for  $C_{N_{\delta e_f}}$  was smaller and  $C_{A_{\delta e_f}}$  approximately equal from the doublet input versus the Dryden single-surface input may be due to the fact that when the trailing edge deflection in the Dryden single-surface input was supposed to occur, the angle of attack of the aircraft was greater than 26 degrees. At 26 degrees angle of attack the trailing edge flaps are deflected to their fullest deflection possible and cannot be used as an input control surface in parameter estimation.

The 30 degree angle of attack flights also compared 16 Cramer-Rao bounds with similar results. The Dryden single-surface input produced the smallest Cramer-Rao bounds in 13 of 16 parameters. The other three parameters had the smallest bounds from the Morelli optimal input technique. These three parameters were the aerodynamic bias-coefficients for the axial force ( $C_{A_0}$ ) and normal force ( $C_{N_0}$ ) as well as the normal force coefficient with respect to elevator deflection ( $C_{N_{\delta e}}$ ). In general, the reason the Dryden single-surface input produced the most accurate parameters was due to the reduced correlation of the input signal (see Section V.C.).

## B. LATERAL-DIRECTIONAL PARAMETERS

The lateral-directional parameters are the coefficients of the Y-force (side force), l-Moment (rolling moment), and n-Moment (yawing moment) equations found and defined in Appendix A (equations A.12-A.14). Control surfaces used in the dynamic model implemented by 'pEst' for the lateral-directional control inputs were aileron, rudder, differential horizontal tail, and thrust vectoring yaw vanes. For the lateral-directional parameters, the Morelli optimal inputs were implemented with the wrong sign on the aileron input. They cannot, therefore, be considered optimal for these experiments. There is an exception to this conclusion which will be discussed later. After the software modeled for the OBES input was completed, analysis of the flight data

exposed the incorrect aileron input. Unfortunately, time and costs have prevented the correct Morelli optimal input to be re-implemented into the parameter estimation flights.

The lateral-directional parameters Cramer-Rao bounds used for comparison were based on seven different flights. Table 5.8 lists the seven flights across the top of the table according to angle of attack, input type, and flight number. Two flights were at 20 degrees angle of attack, one was at 25 degrees angle of attack, and four were at 30 degrees angle of attack. Again, comparisons of the Cramer-Rao bounds from the three flights at 20 and 25 degrees angle of attack were conducted, as were the four flights at 30 degrees angle of attack compared. In the next three sections, the lateral-directional results for the side force parameters, rolling moment parameters, and yawing moment parameters are given.

AOA	20 Alpha		25 Alpha	30 Alpha			
Input Type	Klein OIM	Doubllets	Dryden SSI	Morelli OIM	Klein OIM	Doubllets	Dryden SSI
Flight # >>>	160.5	116.6	165.2	165.3	161.1	116.8	165.3

Table 5.8. Lateral-Directional Flights used for Cramer-Rao Bound Comparisons.

### 1. Y-Force (side force)

#### a. Results for 20 and 25 Degrees Angle of Attack

The final results for the side force parameters Cramer-Rao bounds for the 20 and 25 degrees angle of attack flights are listed in Table 5.9. Side force parameters are the coefficients  $C_{Y_0}$ ,  $C_{Y_\beta}$ ,  $C_{Y_{\delta\alpha}}$ ,  $C_{Y_{\delta\sigma}}$ ,  $C_{Y_{\delta\theta}}$ , and  $C_{\delta yv}$  from the side force equation (Appendix A equation A.12). These parameters are specified in the left column of Table 5.9 with their corresponding Cramer-Rao bounds entered for each separate flight across the row. The first two columns of Cramer-Rao bounds come from the 20 degree angle of attack flights while the last column is from the 25 degree angle of attack flight. Again,  $C_{\delta yv}$ , the thrust vectoring yaw vane coefficient, is used as the same parameter in both the side force equation (Appendix A equation A.12) and the yawing moment equation

(Appendix A equation A.14). The thrust vectoring deflection input was modeled in this manner inside 'pEst' purposely to determine the effective thrust vectoring on the thrust.

The first parameter in Table 5.9 is the Side force Aerodynamic bias,  $C_{Y_0}$ .

The Dryden single-surface input produced the smallest Cramer-Rao bound of the three input techniques. The doublets Cramer-Rao bound value is only 0.5% greater than the Dryden single-surface input Cramer-Rao bound, but a 20% difference in angle of attack exists. Therefore, the Cramer-Rao bound for the Dryden single-surface input is expected to be much better than the true difference would suggest.  $C_{Y_\beta}$ , the change in side force due to a change in sideslip angle, follows in Table 5.9. The Dryden single-surface input has the smallest Cramer-Rao bound with the Klein optimal input Cramer-Rao bound 8.1% larger. Remember, the Klein input is at 20 degrees angle of attack versus the 25 degrees angle of attack for the Dryden single-surface input.

	20 Alpha		25 Alpha
	Klein OIM	Doublets	Dryden SSI
$C_{Y_0}$	5.53E-03	3.83E-03	3.81E-03
$C_{Y_\beta}$	1.60E-03	5.48E-04	1.47E-03
$C_{Y\delta_a}$	3.85E-03	1.96E-03	7.37E-04
$C_{Y\delta_r}$	2.34E-04	2.47E-04	4.01E-04
$C_{Y\delta_h}$	9.88E-03	5.03E-03	1.18E-03
$C_{\delta_{yv}}$	~	5.51E-03	8.21E-04

Table 5.9. Side Force Parameters Cramer-Rao Bounds  
at 20 & 25 Degrees Angle of Attack.

The change in side force with respect to a change in aileron deflection is  $C_{Y_{\delta_a}}$ . In Table 5.9, the Dryden single-surface input Cramer-Rao bound for  $C_{Y_{\delta_a}}$  is 62.4% better than the doublets Cramer-Rao bound.

$C_{Y_s}$  is the change in side force due to a change in rudder deflection. For this parameter, the Cramer-Rao bounds for the doublet input and the Klein optimal input are 5.3% different with the Klein input Cramer-Rao bound being smaller. The Klein input Cramer-Rao bound, shown in Table 5.9, is 41.6% less than the Dryden single-surface input. Therefore even though the Dryden single-surface input is at a higher angle of attack, the parameter from the Klein input in this case appears to be more accurate.

A change in side force with respect to a differential horizontal tail deflection is represented by  $C_{Y_d}$ . Table 5.9 shows that the Cramer-Rao bound for the Dryden single-surface input is the smallest by 88% over the Klein input and 76.5% over the doublet input.

The thrust vectoring parameter exists in both the side force equation and yawing moment equation inside 'pEst'. For the results,  $C_{\delta_{Yv}}$  is the amount of yaw deflection in the thrust for a given amount of deflection in the yaw vanes. Table 5.9 again shows that the Klein flights did not engage the research flight control system (RFCS) since no Cramer-Rao bound has been determined for the yaw vane parameter,  $C_{\delta_{Yv}}$ . The smallest Cramer-Rao bound for  $C_{\delta_{Yv}}$  came from the Dryden single-surface input with an 85.1% improvement over the doublet input.

Figure 5.7 shows the above results in an easy to interpret bar graph format. The figure has the side force parameters along the X-axis with the respective Cramer-Rao bounds on the Y-axis. Each parameter has three distinct Cramer-Rao bounds shown using different shades to represent the three different inputs compared. The figure reconfirms the fact that the Dryden single-surface input Cramer-Rao bounds are the smallest in each case, except for the  $C_{Y_s}$  parameter where the Klein input has the smallest Cramer-Rao bound. The Dryden input using the OBES to implement the input reduces a large amount of the correlation between the control surface inputs that exist in the piloted Klein and doublet inputs. There is an exception of high correlation seen in

the Dryden input between the rudder and yaw vane control surfaces when the yaw vane doublet is input.

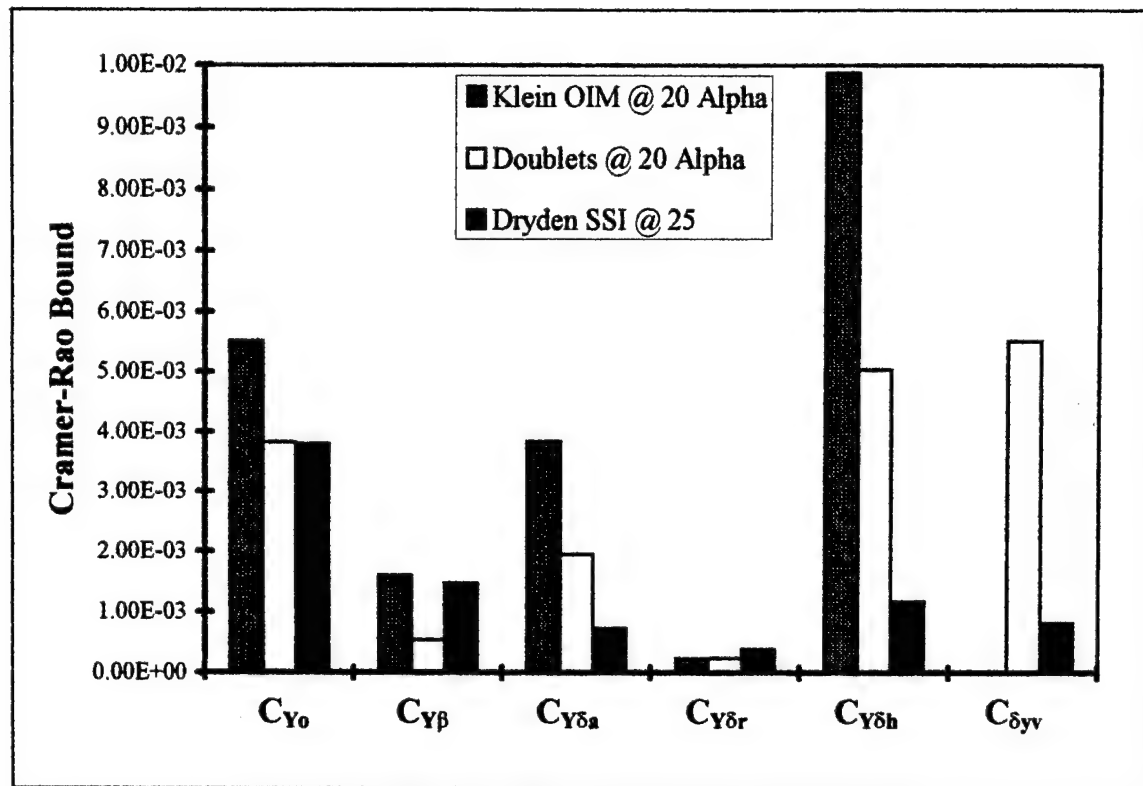


Figure 5.7. Side Force Parameters Cramer-Rao Bounds at 20 & 25 Degrees Angle of Attack.

#### b. Results for 30 Degrees Angle of Attack

The final results for the 30 degree angle of attack side force parameters Cramer-Rao bounds are found in Table 5.10. The parameters are listed in the far left column with their respective Cramer-Rao bounds listed across each row according to input type. For the 30 degree angle of attack flights, the Dryden single-surface input again produce the smallest Cramer-Rao bounds in all parameters except  $C_{Y_\delta}$ . The smallest Cramer-Rao bound for this parameter came from the Klein optimal input. The

Klein optimal input must have excited the system more effectively with the rudder deflections,  $\delta r$ , than did the Dryden single-surface input.

30 Alpha				
	Morelli OIM	Klein OIM	Doublets	Dryden SSI
$C_{Y_0}$	4.89E-03	8.98E-03	1.02E-02	4.41E-03
$C_{Y_\beta}$	2.59E-03	1.56E-03	4.26E-03	1.62E-03
$C_{Y_{\delta a}}$	8.51E-04	7.80E-03	2.03E-03	8.27E-04
$C_{Y_{\delta r}}$	1.04E-03	3.21E-04	1.40E-03	4.44E-04
$C_{Y_{\delta h}}$	7.44E-03	1.99E-02	5.73E-03	1.29E-03
$C_{\delta yv}$	3.98E-02	~~~	1.14E-02	8.25E-04

Table 5.10. Side Force Parameters Cramer-Rao Bounds at 30 Degrees Angle of Attack.

Figure 5.8 illustrates the 30 degree angle of attack side force parameters Cramer-Rao bounds using a bar graph style. The side force parameters are along the X-axis on the bottom of the figure with their Cramer-Rao bounds shown using separate bars for each input technique.

As mentioned in the introduction for the lateral-directional parameters, the Morelli input had a wrong sign for the aileron input. Although, this sign error prohibited the input from being optimal, the input had the correct side force. The fact that the input had the correct side force is significant since the Cramer-Rao bounds for  $C_{Y_0}$ ,  $C_{Y_{\delta a}}$ , and  $C_{Y_{\delta r}}$  from the Morelli input have a significant improvement over the Klein Cramer-Rao bounds for these same parameters. For the other two side force parameters that could be compared,  $C_{Y_\beta}$  and  $C_{Y_{\delta h}}$ , the Klein Cramer-Rao bounds and the Morelli Cramer-Rao bounds were similar. Therefore, Morelli optimal inputs may produce much better Cramer-Rao bounds if the correct aileron deflection is input.

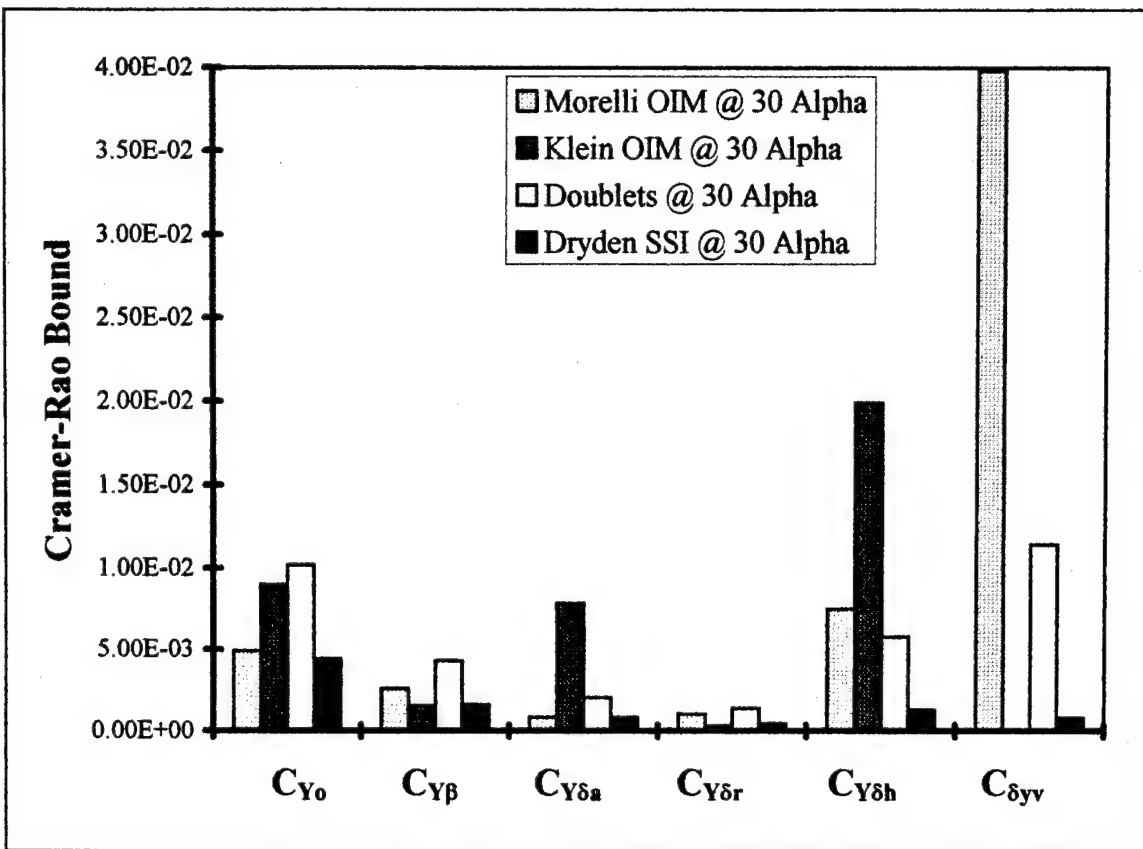


Figure 5.8. Side Force Parameters Cramer-Rao Bounds at 30 Degrees Angle of Attack.

## 2. I-Moment (rolling moment)

### a. Results for 20 and 25 Degrees Angle of Attack

The final results for the rolling moment parameters Cramer-Rao bounds for the 20 and 25 degree angle of attack flights are found in Table 5.11. The rolling moment parameters are the coefficients  $C_{I_0}$ ,  $C_{I_\beta}$ ,  $C_{I_p}$ ,  $C_{I_r}$ ,  $C_{I_{\delta a}}$ ,  $C_{I_{\delta r}}$ , and  $C_{I_{\delta h}}$  from the rolling moment equation (Appendix A equation A.13). These parameters are shown in the far left column with their respective Cramer-Rao bounds listed across the row for each separate input.

The aerodynamic bias for rolling moment,  $C_{I_0}$ , starts the entries for Table 5.11. The Dryden single-surface input produced the smallest Cramer-Rao bound for  $C_{I_0}$  of the three input techniques by an order of magnitude difference.

	20 Alpha		25 Alpha
	Klein OIM	Doublets	Dryden SSI
$C_{l\beta}$	1.73E-04	1.26E-04	3.42E-05
$C_{l\beta}$	2.29E-05	1.51E-05	1.89E-05
$C_{l\beta}$	4.75E-03	8.38E-03	5.44E-03
$C_{l\gamma}$	1.14E-02	1.18E-02	1.98E-02
$C_{l\delta_a}$	1.73E-04	1.08E-04	8.70E-06
$C_{l\delta_r}$	5.41E-06	6.12E-06	4.74E-06
$C_{l\delta_h}$	4.45E-04	2.85E-04	1.24E-05

Table 5.11. Rolling Moment Parameters Cramer-Rao Bounds at 20 & 25 Degrees Angle of Attack.

The next parameter listed in Table 5.11 is the coefficient for a change in rolling moment with respect to a change in sideslip angle,  $C_{l\beta}$ . The doublet Cramer-Rao bound for the  $C_{l\beta}$  parameter has a 20.1% improvement over the Dryden single-surface input Cramer-Rao bound. However, the angle of attack difference between the two inputs is 20%. Therefore, the two bounds for  $C_{l\beta}$  are approximately the same, and their corresponding parameters have similar accuracy.

$C_{l_p}$  is the parameter for a change in rolling moment with respect to a change in roll rate. The Cramer-Rao bound determined from the Klein optimal input for  $C_{l_p}$  shows a 12.7% improvement over the Dryden single-surface input Cramer-Rao bound. Again, the angle of attack difference is 20% between the two inputs; the Cramer-Rao bound from the Dryden single-surface input is better, and the determined  $C_{l_p}$  parameter is expected to be more accurate.

The next parameter in Table 5.11 is  $C_{l_r}$ .  $C_{l_r}$  is the change in rolling moment with respect to a change in yaw rate. The Cramer-Rao bound from the Klein optimal input has the smallest magnitude of the three inputs with a magnitude of

improvement over the Dryden single-surface input of 42.4%. This significant improvement discounts the angle of attack difference, thereby making the corresponding parameter for  $C_{I_r}$  from the Klein input the most accurate.

$C_{I_{\delta a}}$  is the change in rolling moment due to a change in the deflection of the aileron control surface. Table 5.11 shows that the Cramer-Rao bound for the Dryden single-surface input has better than an order of magnitude improvement over the Klein and doublet inputs.

$C_{I_{\delta r}}$  is the change in rolling moment due to a change in the rudder deflection control surface. In Table 5.11, the smallest Cramer-Rao bound for  $C_{I_{\delta r}}$  comes from the Dryden single-surface input. This bound has a 22.5% improvement over the doublet and a 12.4% improvement over the Klein input without even considering the angle of attack difference.

The last parameter listed in Table 5.11,  $C_{I_{\delta h}}$ , is the change in rolling moment due to a change in differential horizontal tail deflection. The values listed for this last parameter show, once again, that the Dryden single-surface input has greater than an order of magnitude improvement over the doublet and Klein inputs.

The summary for all the rolling moment parameters except  $C_{I_p}$  and  $C_{I_r}$  is shown in Figure 5.9. The two parameters  $C_{I_p}$  and  $C_{I_r}$  are not shown due to their large numerical magnitudes compared to the other Cramer-Rao bound magnitudes. The rolling moment parameters are listed across the bottom of Figure 5.9 with the Cramer-Rao bounds shown using a bar graph for each input type. Therefore, three Cramer-Rao bound bars exist for each parameter. For all five parameters shown, the Dryden single-surface input Cramer-Rao bounds are the smallest. Of the two remaining parameters, the Klein optimal input had the smallest Cramer-Rao bound in the  $C_{I_r}$  case, and the Klein optimal input and Dryden single-surface input Cramer-Rao bounds were approximately equal in

the last parameter  $C_{I_p}$ . Therefore, the rolling moment parameters from the Dryden single-surface input appear to be the most accurate.

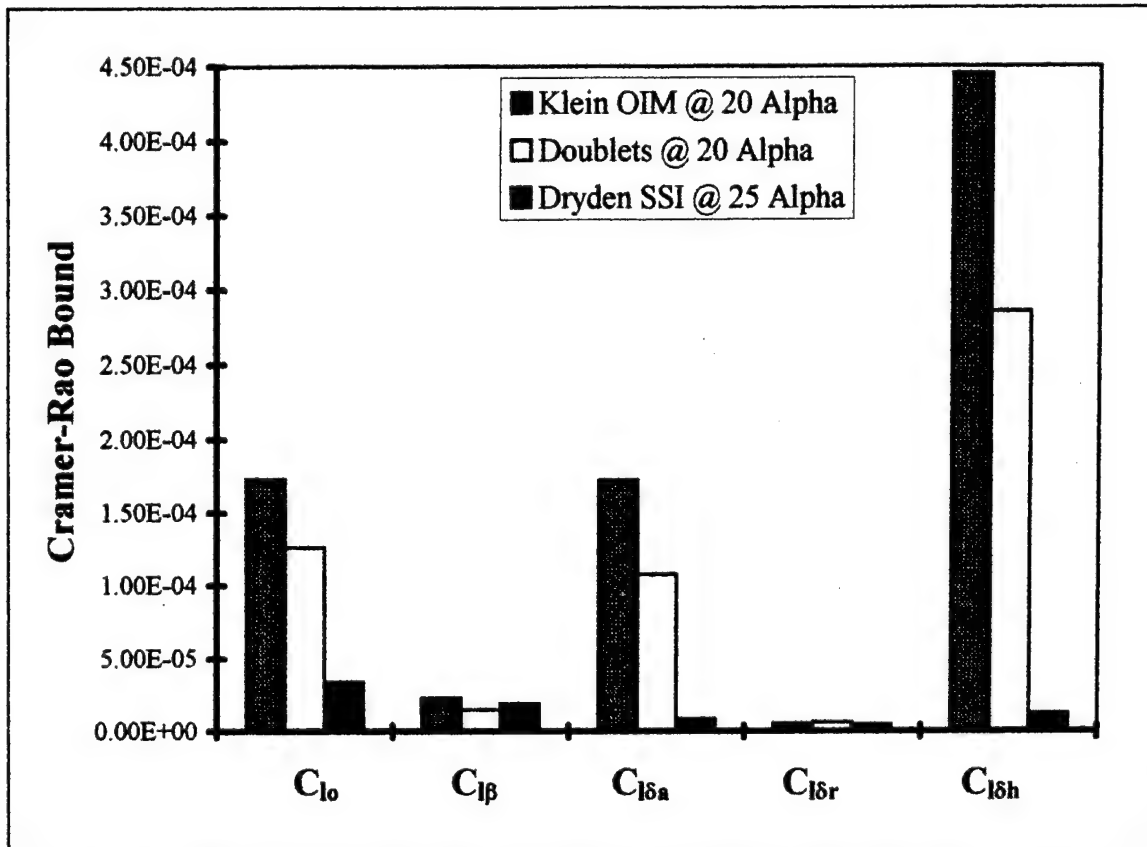


Figure 5.9. Rolling Moment Parameters Cramer-Rao Bounds at 20 & 25 Degrees Angle of Attack.

#### b. Results for 30 Degrees Angle of Attack

The final results for the rolling moment parameters Cramer-Rao bounds from the 30 degree angle of attack flights are shown in Table 5.12. The rolling moment parameters are listed in the far left column with their respective Cramer-Rao bounds listed across the row for each separate input. The 30 degree angle of attack lateral-directional cases included inputs from each type of input. Since all four input techniques were used for the 30 degree angle of attack flights, good comparisons were obtained.

	30 Alpha			
	Morelli OIM	Klein OIM	Doublets	Dryden SSI
$C_{l_0}$	1.10E-03	2.78E-04	8.50E-05	3.05E-05
$C_{l_p}$	1.23E-03	2.10E-05	5.60E-05	1.55E-05
$C_{l_p}$	0.4138	6.60E-03	1.13E-02	6.74E-03
$C_{l_r}$	0.9641	1.54E-02	3.00E-02	2.18E-02
$C_{l_{\delta a}}$	3.60E-04	2.98E-04	6.87E-05	8.22E-06
$C_{l_{\delta r}}$	3.70E-04	4.99E-06	1.94E-05	4.53E-06
$C_{l_{\delta h}}$	3.52E-03	7.59E-04	1.73E-04	1.26E-05

Table 5.12. Rolling Moment Parameters Cramer-Rao Bounds at 30 Degrees Angle of Attack.

Table 5.12 shows that five of seven Cramer-Rao bounds are smallest from the Dryden single-surface input techniques.  $C_{l_{\delta a}}$  and  $C_{l_{\delta h}}$  Cramer-Rao bounds are smaller by an order of magnitude over the doublet input Cramer-Rao bounds for the same two parameters. The two of seven Cramer-Rao bounds that were smaller from the Klein optimal input were for the parameters  $C_{l_p}$  and  $C_{l_r}$  which also had smaller Cramer-Rao bounds in the lower angle of attack flights as well.

Figure 5.10 shows a visual summary of the rolling moment parameters Cramer-Rao bounds at 30 degrees angle of attack. The two parameters  $C_{l_p}$  and  $C_{l_r}$  Cramer-Rao bounds are not included again for the same reason of being too large in comparison with the other parameters Cramer-Rao bounds. The rolling moment parameters are listed across the bottom of the figure, each of which has four separate Cramer-Rao bounds displayed above the parameter name. The result of the Dryden single-surface input Cramer-Rao bounds being the smallest is easily identifiable, which implies the parameters determined from the Dryden single-surface input are expected to be the most accurate.

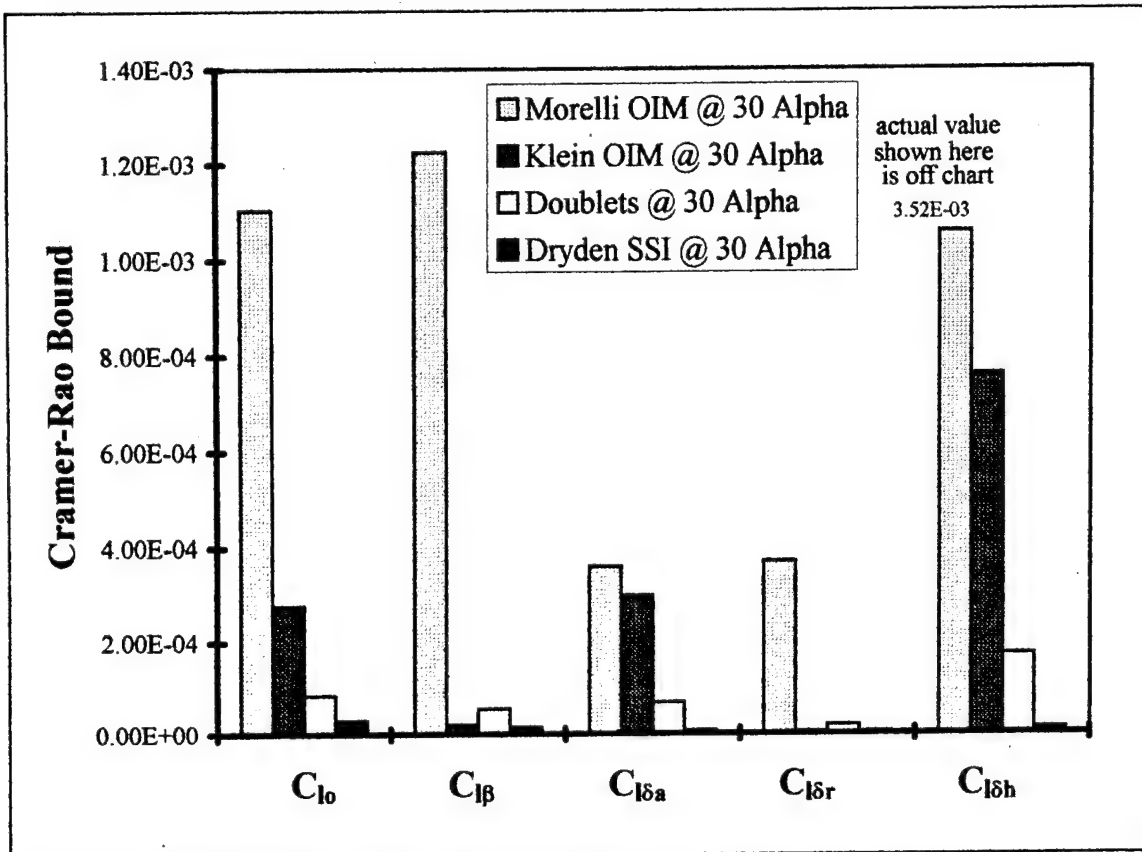


Figure 5.10. Rolling Moment Parameters Cramer-Rao Bounds at 30 Degrees Angle of Attack.

### 3. n-Moment (yawing)

#### a. Results for 20 and 25 Degrees Angle of Attack

The final results for the yawing moment parameters Cramer-Rao bounds for the 20 and 25 degree angle of attack flights can be seen in Table 5.13. The yawing moment parameters are the coefficients  $C_{n_0}$ ,  $C_{n_\beta}$ ,  $C_{n_p}$ ,  $C_{n_r}$ ,  $C_{n_{\delta_a}}$ ,  $C_{n_{\delta_r}}$ , and  $C_{n_{\delta_h}}$  from the yawing moment equation (Appendix A, equation A.14). The parameters are displayed in the left column with their corresponding Cramer-Rao bounds shown across the row for each type of input listed at the top of the table.

	20 Alpha		25 Alpha
	Klein OIM	Doublets	Dryden SSI
$C_{n_0}$	3.02E-04	1.62E-04	3.10E-05
$C_{n\beta}$	5.72E-05	3.26E-05	6.67E-05
$C_{n_p}$	1.15E-02	1.62E-02	1.43E-02
$C_{n_r}$	1.84E-02	1.84E-02	3.35E-02
$C_{n\delta_a}$	3.42E-04	1.46E-04	2.95E-05
$C_{n\delta_r}$	1.04E-05	2.19E-05	1.11E-05
$C_{n\delta_h}$	8.43E-04	3.87E-04	3.36E-05

Table 5.13. Yawing Moment Parameters Cramer-Rao Bounds at 20 & 25 Degrees Angle of Attack.

The first parameter in Table 5.13 is the aerodynamic bias for yawing moment,  $C_{n_0}$ . The Dryden single-surface input had the smallest Cramer-Rao bound for this parameter of the three input techniques compared.

The next parameter,  $C_{n\beta}$ , is the change in yawing moment due to a change in sideslip angle. The smallest Cramer-Rao bound for  $C_{n\beta}$  came from the doublet input which showed an improvement of 51.1% compared to Dryden's single-surface input and 43.0% compared to the Klein input.

$C_{n_p}$  is the change in yawing moment due to the change in roll rate. The Cramer-Rao bound for  $C_{n_p}$  from the Klein optimal input is 19.6% smaller than that from the Dryden single-surface input in Table 5.13. The percentage difference in angle of attack between the inputs is 20%. Therefore the two Cramer-Rao bounds are approximately equal, and their corresponding parameters are of the same accuracy.

Table 5.13 lists  $C_{n_r}$ , the change in yawing moment due to a change in yaw rate, next. The Cramer-Rao bounds for  $C_{n_r}$  from the doublet input and Klein

optimal input are exactly equal to the three significant digits shown. This bound has a 45.1% improvement over the Dryden single-surface input Cramer-Rao bound.

$C_{n_{\alpha}}$  is the change in yawing moment due to a change in the aileron deflection.  $C_{n_{\alpha}}$  follows  $C_{n_r}$  in Table 5.13. The smallest Cramer-Rao bound for  $C_{n_{\alpha}}$  came from the Dryden single-surface input technique. The bound was a 79.8% improvement over the doublet input Cramer-Rao bound, and better than an order of magnitude difference over the Klein Cramer-Rao bound.

$C_{n_{\delta r}}$  is the change in yawing moment due to a change in the rudder deflection. The Klein optimal input Cramer-Rao bound for  $C_{n_{\delta r}}$  is 6.3% smaller than the Dryden single-surface input Cramer-Rao bound, but the angle of attack difference is 20%. Therefore, the Dryden single-surface input Cramer-Rao bound is a smaller bound and has a more accurate corresponding parameter.

The final lateral-directional parameter listed in Table 5.13 is  $C_{n_{\delta h}}$  which is the change in yawing moment due to a change in the differential horizontal tail deflection. Again, the Cramer-Rao bound for  $C_{n_{\delta h}}$  from the Dryden single-surface input is more than an order of magnitude improvement from the doublets Cramer-Rao bound.

In summary, five of seven yawing moment parameters Cramer-Rao bounds were smallest for the Dryden single-surface input. One of the five,  $C_{n_p}$ , was approximately equal to the Klein optimal input Cramer-Rao bound. The final two parameters,  $C_{n_{\beta}}$  and  $C_{n_r}$ , had smaller Cramer-Rao bounds from the doublet input and Klein optimal input respectively. An interesting note is that  $C_{n_p}$  and  $C_{n_r}$  from the yawing moment parameters and  $C_{l_p}$  and  $C_{l_r}$  from the rolling moment parameters had smaller Cramer-Rao bounds produced from inputs other than the Dryden single-surface input.

The final summary written in the previous paragraph can be easily identified in Figure 5.11. The two rotational rate Cramer-Rao bounds for the parameters,  $C_{n_p}$  and  $C_{n_r}$ , are again not printed due to their larger magnitude in comparison to the remaining bounds. The yawing moment parameters are listed across the bottom of the figure with the three Cramer-Rao bounds, from each type of input, graphed using a bar graph format above the listed parameters.

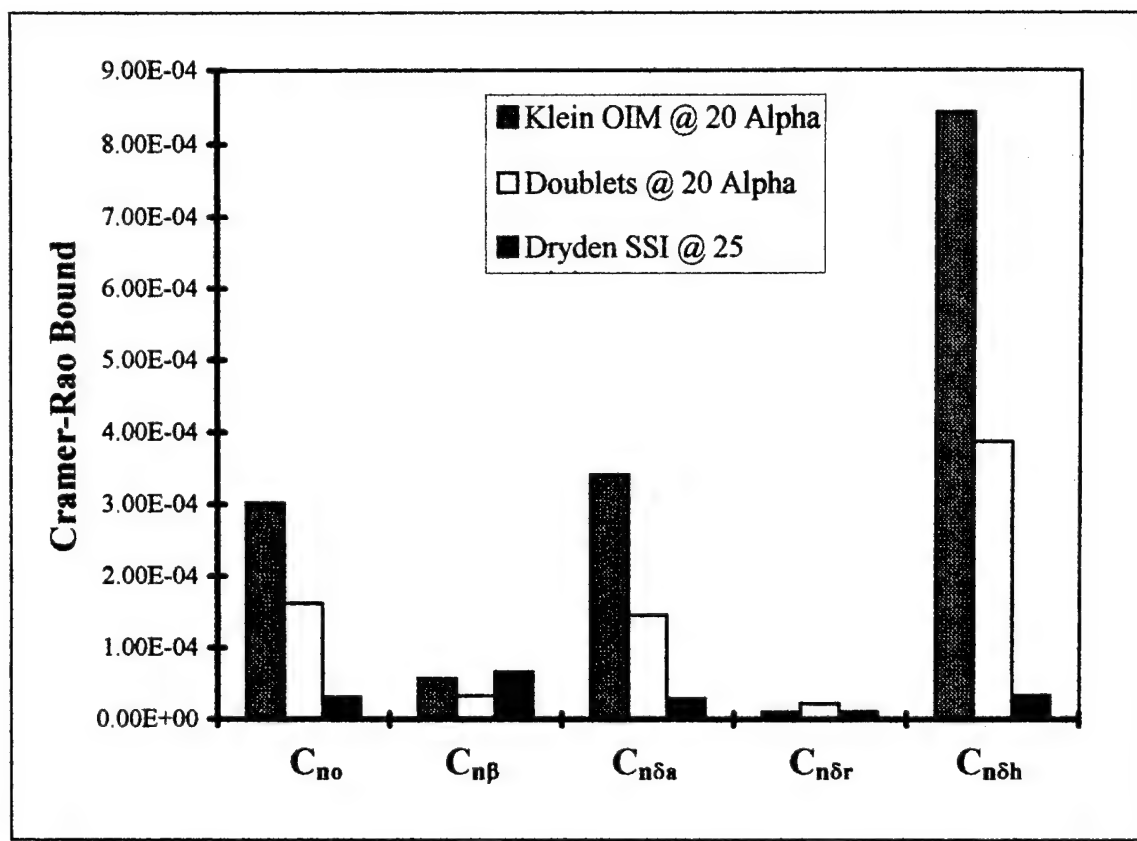


Figure 5.11. Yawing Moment Parameters Cramer-Rao Bounds at 20 & 25 Degrees Angle of Attack.

### b. Results for 30 Degrees Angle of Attack

The final results for the yawing moment parameters Cramer-Rao bounds from the 30 degree angle of attack are displayed in Table 5.14. The yawing moment parameters are listed on the left of the table with the corresponding Cramer-Rao bounds printed across each row according to the type of input listed at the top of the table.

	30 Alpha			
	Morelli OIM	Klein OIM	Doublets	Dryden SSI
$C_{n_0}$	1.57E-03	5.29E-04	2.60E-04	1.20E-05
$C_{n\beta}$	2.85E-03	6.41E-05	3.27E-04	6.81E-05
$C_{n_p}$	2.216	1.51E-02	4.27E-02	1.86E-02
$C_{n_r}$	1.297	2.10E-02	0.1134	3.27E-02
$C_{n\delta_a}$	7.68E-04	5.76E-04	2.04E-04	3.13E-05
$C_{n\delta_r}$	2.74E-04	1.14E-05	3.09E-04	1.10E-05
$C_{n\delta_h}$	1.55E-02	1.48E-03	4.17E-04	2.79E-05

Table 5.14. Yawing Moment Parameters Cramer-Rao Bounds at 30 Degrees Angle of Attack.

The results for the 30 degree angle of attack flights are very similar to those for the 20 and 25 degrees angle of attack flights. The aerodynamic bias,  $C_{n_0}$ , has the smallest Cramer-Rao bound from the Dryden single-surface input. The next three parameters,  $C_{n_\beta}$ ,  $C_{n_p}$ , and  $C_{n_r}$ , all have the smallest Cramer-Rao bounds from the Klein optimal input technique. The remaining three parameters have the smallest Cramer-Rao bounds from the Dryden single-surface input.

The 30 degrees angle of attack flights yawing moment parameters Cramer-Rao bounds excluding the rotational rate parameters,  $C_{n_p}$  and  $C_{n_r}$ , are shown in Figure 5.12. The results discussed in the previous paragraph are visually illustrated in the

figure. The yawing moment parameters are listed across the bottom of Figure 5.12 with the corresponding Cramer-Rao bound plots above each parameter. Each parameter has four bars, one bar for each type of input shown in the legend.

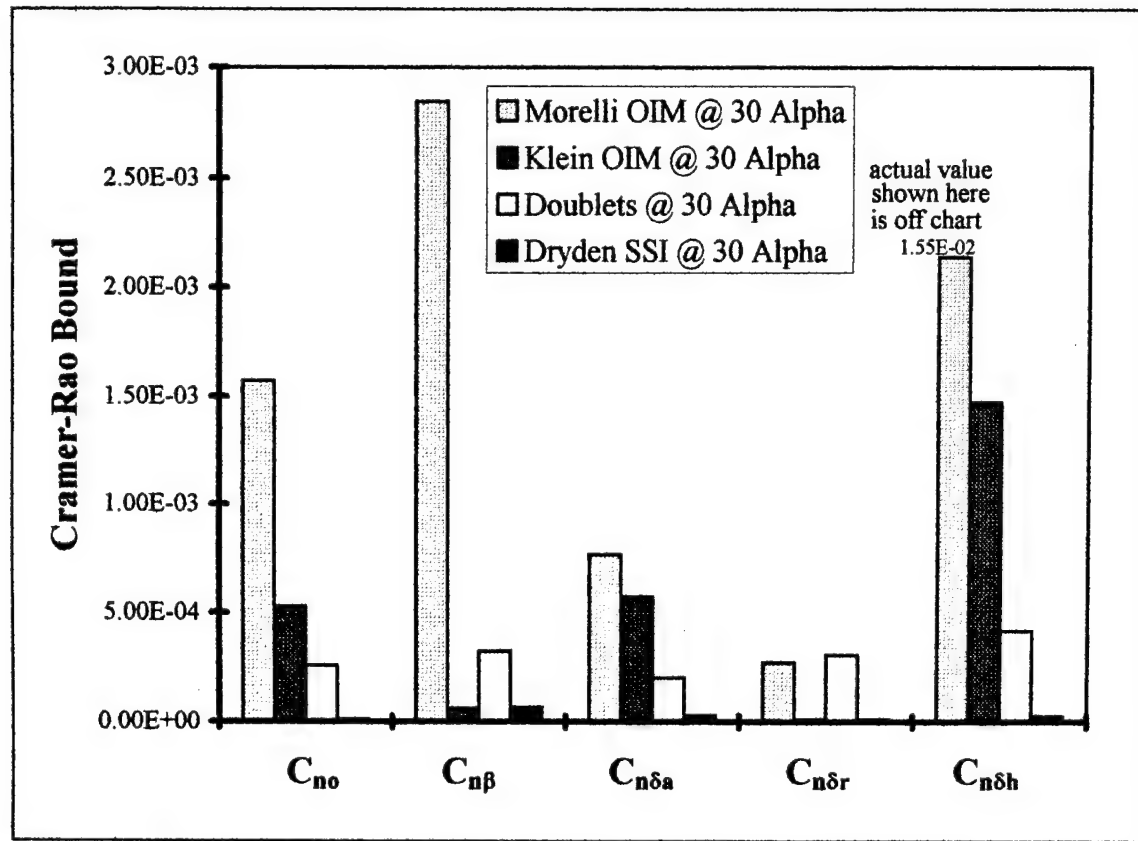


Figure 5.12. Yawing Moment Parameters Cramer-Rao Bounds at 30 Degrees Angle of Attack.

#### 4. Lateral-Directional Parameters Summary

In summary, the Cramer-Rao bounds for the rotational rate derivatives,  $C_{l_p}$ ,  $C_{l_r}$ ,  $C_{n_p}$ , and  $C_{n_r}$ , in both the 20 and 25 degrees angle of attack flights and the 30 degree angle of attack flights were smaller from inputs other than the Dryden single-surface input. Dryden single-surface inputs created the smallest Cramer-Rao bounds for all of the other parameters in the 30 degree angle of attack case and in 14 of 16 in the 20 and

25 degree cases. A reason may be due to the fact that the Dryden single-surface input technique does not excite the rolling and yawing rates enough. Another reason could be a coupling of the yawing rate and rolling rate responses canceling each other out making computation of the parameters difficult, which implies larger Cramer-Rao bounds.

### C. CORRELATION MATRICES

The correlation matrix was introduced in Section IV.E. Figure 5.13 displays the correlation matrix from the Dryden single-surface input flight number 166.3. The matrix is a square matrix with ones along the diagonal and whose rows and columns are defined by the parameters being determined. Analysis of the matrix will indicate where high correlation exists between two parameters which may establish and/or verify results. Figure 5.13 shows that there are only 16 entries, not including the diagonal ones, which have values larger than 0.7000. Elements of the matrix above this chosen value indicate that the two parameters corresponding to the row and column have high correlation. The information acquired by performing an analysis to find the high correlation between two parameters is trivial but helpful.

The approach for the analysis used for the results discussed here was to determine the root mean square and standard deviation of the correlation matrices corresponding to each input. The use of MATLAB, some macro files, and reference [19] enabled Table 5.15 to be produced (see Appendix C). Table 5.15 shows the root mean square and standard deviation for the correlation matrix that corresponds to the flight number and input type listed in the left two columns. The values for root mean square and standard deviation shown in Table 5.15 are for the longitudinal results of Section V.A. Smaller values for the root mean square and standard deviation of the correlation matrix indicate an overall lower correlation between the estimated parameters which define the rows and columns of the correlation matrix. Therefore, Table 5.15 shows that the

1.000	-0.4572	-0.1634	5.8296E-02	-0.2939	0.1348	1.3725E-02	-4.3482E-02	4.8975E-02	3.8775E-02
-0.4572	1.000	-0.2383	-0.3984	-0.1599	-0.0102E-02	0.1238	0.1003	-9.1962E-02	3.9620E-02
-0.1634	-0.2383	1.000	0.2775	-7.7853E-02	-0.1844	0.2664	0.8537E-02	-5.8882E-02	-0.1043
5.8296E-02	-0.3984	0.2775	1.000	7.2762E-02	0.5922E-02	6.3374E-02	-2.3977E-02	1.6358E-02	-2.1692E-02
-0.2939	-0.1599	-7.7853E-02	7.2762E-02	1.000	-0.1132	4.5624E-03	3.1111E-02	1.4099E-02	-3.0537E-03
0.1348	-7.0102E-02	0.2665	6.5952E-02	-0.1132	4.1527E-02	1.3276E-02	-2.3911E-02	-2.0052E-04	
1.3725E-02	-0.1238	0.1844	6.3374E-02	4.5624E-03	4.1527E-02	1.000	-0.6443	0.5210	-0.4505
-4.3482E-02	0.1003	2.8527E-02	-2.3977E-02	-3.1111E-02	0.3226E-02	-0.6443	1.000	-0.9773	0.4889
4.8975E-02	9.1962E-02	5.8482E-02	1.6358E-02	3.1409E-02	-2.2811E-02	0.5210	-0.9773	-0.4557	
3.8775E-02	3.9620E-02	-0.1043	-2.1692E-02	-3.0537E-02	-2.0022E-04	0.5055	0.6889	-0.4357	1.000
-1.9318E-03	7.3111E-02	-0.1044	-4.1113E-02	-1.3431E-02	-3.8744E-02	-0.7200	0.5086	-0.3196	0.3578
-3.1553E-03	-3.5631E-02	8.4500E-02	6.1118E-05	-4.1118E-05	-5.3255E-03	0.3887	-0.1654E-02	-6.9803E-02	-0.5881
1.3531E-02	3.5321E-02	-4.6169E-02	-3.3704E-02	-2.3942E-02	-2.6832E-03	0.4470	0.5428	-0.4815	0.5678
0.9197	-0.1516	-0.3205	-0.1019	-0.3503	0.1121	-0.1341	0.3215E-02	-8.4771E-02	0.1640
-0.8936	0.2666	0.3063	5.9156E-02	0.2871	0.1053	0.1727	-0.1168	-0.1106	-0.2138
-5.1507E-02	-0.1494	0.1931	0.4924	7.8802E-02	0.3898E-03	-8.5981E-02	0.3500	-0.3507	6.3670E-02
-0.2738	-0.1178	5.9398E-02	9.3877E-02	0.6886	-4.5946E-02	-0.2884	0.2921	-0.2003	2.4070E-02
7.6873E-02	0.1122	-0.1234	-4.2353E-02	-2.8792E-02	0.4336	0.2712E-02	0.3000	-0.3725	7.2360E-02
1.1739E-02	3.6550E-03	-8.3724E-03	-7.1526E-03	8.1058E-03	-2.3887E-03	-3.9555E-02	4.6947E-02	-5.8711E-02	-1.6143E-02
-0.8591	-5.7396E-02	0.3329	0.2232	0.4058	-0.1100	5.6556E-02	-7.3038E-03	-4.2301E-03	-6.6181E-02
correlation matrix continued									
-1.9318E-03	-3.4553E-03	1.3531E-02	0.9197	-0.8936	-5.1507E-02	-0.2738	7.6873E-02	1.1739E-02	-0.8591
7.3111E-02	-3.5631E-02	3.5321E-02	-0.1516	0.2666	-0.1494	-0.1178	0.1122	3.6550E-03	-5.7396E-02
-0.1044	6.4540E-02	4.6169E-02	-0.3205	0.3063	0.1931	5.9398E-02	-0.1234	-0.3724E-03	0.3359
-4.1113E-02	3.7166E-05	-3.3704E-02	-0.1019	5.9156E-02	0.4924	9.3877E-02	-0.4253E-02	-7.1526E-03	0.2232
-1.3431E-02	-4.1118E-02	2.3942E-02	-0.3503	0.2871	7.8802E-02	0.6886	-0.8792E-02	0.1098E-03	0.4088
-3.8744E-02	-5.3255E-03	6.6832E-03	-0.1211	-0.1073	0.3886E-03	-0.4946E-02	0.4336	-2.3887E-03	-0.1100
-0.7700	0.3387	-0.4470	-0.1341	-0.1727	-0.5981E-02	-0.2594	-0.5210E-02	-3.9555E-02	5.6956E-02
0.5086	-1.1654E-02	0.5428	9.3215E-02	-0.1168	0.3550	0.2321	0.3400	4.6947E-02	-0.8591
-0.3196	-6.9503E-02	-0.4815	-8.4771E-02	0.1106	-0.3597	-0.2003	-0.3725	-5.8711E-02	-7.3038E-03
0.3578	-0.5841	0.5678	0.1640	-0.2138	6.3620E-02	2.4070E-02	7.2360E-02	-0.2301E-03	-4.2301E-03
1.000	-0.3575	0.4924	4.5455E-02	-3.4538E-02	0.1434	0.2171	-0.1944E-02	-1.6143E-02	-6.6181E-02
-0.3575	1.000	-0.2732	-9.9333E-02	0.1388	-2.1770E-02	9.9606E-02	-7.2347E-02	0.2015	2.5301E-02
0.4924	-0.2732	1.000	2.1592E-02	-8.4583E-04	0.1167	0.1550	-3.7544E-02	-7.5124E-02	-3.6556E-02
4.5455E-02	-9.9333E-02	2.1592E-02	1.000	-0.9728	-0.1265	-0.2711	0.1928	-5.5916E-03	-9.4557
-3.4553E-02	0.1388	-8.4583E-04	-0.9728	1.000	0.1848	0.1624	-0.2031	1.9068E-02	0.8523
0.1434	-2.1770E-02	0.1167	-0.1265	0.1848	1.000	-0.1236	0.7092E-02	-1.9888E-02	0.1736
0.2171	9.9606E-02	0.1550	-0.2111	0.1624	-0.2031	0.1663	-0.1663	9.5567E-03	0.3656
-1.0744E-02	-7.7347E-02	0.1928	-0.1928	0.1928	-0.1928	1.000	-0.2291E-02	-0.1511	
-2.6433E-02	0.2015	-7.5124E-03	-5.5916E-03	1.9068E-02	-1.9888E-02	0.1736	-0.1511	1.000	-1.6019E-02
-4.0470E-02	2.5301E-02	-3.6556E-02	-0.9457	0.8523	0.1736	0.3656	-0.1511	-1.6019E-02	1.000

Figure 5.13. Correlation Matrix from Dryden Single-Surface Input.

Flight #	Input Type	AOA	Root Mean Square	Standard Deviation
116.7	Early Regular Doublets	30	0.4571	0.4543
165.2	Morelli Optimal Input Maneuver	30	0.4564	0.4537
166.3	Dryden Single Surface Inputs	30	0.3513	0.3496
156.1	Klein Optimal Input Maneuver *	25	0.3979	0.3969
167.1	Dryden Single Surface Inputs	25	0.3674	0.3662
116.5	Early Regular Doublets	20	0.4748	0.4745
153.2	Klein Optimal Input Maneuver *	20	0.4676	0.4678

Table 5.15. Longitudinal Flights Root Mean Squares & Standard Deviations.

Dryden single-surface input technique has the smallest root mean square and standard deviation in both the 20 and 25 degree angle of attack cases and the 30 degree angle of attack cases. This result just verifies earlier results determined in Sections V.A.1 through V.A.3.

Figure 5.14 is the correlation matrix from the doublet input flight number 116.7 at 30 degrees angle of attack. The figure shows 42 entries above 0.7000. The corresponding root mean square and standard deviation are larger than the values exhibited for the Dryden single-surface input already mentioned.

Table 5.16 displays the lateral-directional results for the root mean square and standard deviation of the respective correlation matrices. Again, the flight number and input type are shown in the left two columns. The respective angle of attack for the corresponding flight is then listed followed by the root mean square and standard deviation of the correlation matrix. The results from the 20 and 25 degrees angle of attack flights show that the root mean square from the doublet input (flight 116.6) is less than 0.5 % smaller than the root mean square from the Dryden input (flight 165.2) and the standard deviation for the doublet is less than 0.33 % smaller than the Dryden root

1.000	-0.6969	0.6117	0.5100	-0.4132	-4.7180E-02	-2.3090E-03	-2.7193E-03	-8.4142E-02	-5.5512E-02
-0.6969	1.000	-0.7710	-0.6223	0.7873	-2.8059E-02	3.2967E-02	-3.1109E-02	-2.6920E-02	-5.3299E-02
0.6117	-0.7710	1.000	0.7374	-0.795	-8.3076E-02	5.5701E-02	-6.8958E-02	-7.9666E-02	-8.4797E-02
0.5100	-0.6223	0.7374	1.000	-0.5296	-0.2215	0.1764	-0.2015	-0.2025	-0.2223
-0.4132	0.7873	-0.7595	-0.5296	1.000	-1.9844E-02	2.2537E-02	-2.2361E-02	-8.3288E-03	-1.9034E-02
-4.7180E-02	-2.8059E-02	-8.3076E-02	-0.2215	-1.9844E-02	1.000	-0.8517	0.9437	0.8421	0.9906
4.7193E-03	3.2967E-02	5.5701E-02	0.1764	2.2537E-02	-0.8517	1.000	-0.9759	-0.4577	-0.7984
-2.3090E-02	-3.1109E-02	-2.6920E-02	-0.2015	-8.3076E-02	0.9337	-0.9759	1.000	0.6365	0.9104
-8.4142E-02	-2.6920E-03	-7.9666E-02	-0.2025	-8.3076E-03	-0.8421	-0.4577	0.6365	0.1000	0.8894
-5.5512E-02	-2.3899E-02	-8.4797E-02	-0.2223	-1.9034E-02	0.9906	-0.7984	0.9104	0.8894	1.000
-7.3820E-03	-3.6593E-02	-5.8936E-02	-0.1772	-1.7379E-02	0.8379	-0.9867	0.9640	0.4426	0.7909
0.8495	-0.3584	0.2508	0.2349	-0.1083	-3.0534E-02	-2.4146E-02	4.4853E-03	-7.9563E-02	-3.4699E-02
-0.7398	0.3513	-0.1844	-0.1855	0.1267	-6.9764E-03	4.9525E-02	-3.6462E-02	4.5588E-02	-6.2000E-03
-1.8865E-03	1.5549E-02	9.9931E-02	0.2027	0.39620E-03	-0.1649	9.2020E-02	-0.1219	-0.1388	-0.1704
7.9230E-02	-6.6794E-03	-0.1761	0.1282	0.1390	-0.1645	0.1297	-0.1531	-0.1615	-0.1802
-1.0534E-02	2.5512E-02	-2.7285E-03	1.4551E-02	1.5410E-02	-0.1228	0.1228	-0.1176	-0.1716	-0.1486
-0.8950	0.3077	-0.3143	-0.2471	5.3649E-02	6.3266E-02	-1.2098E-02	3.4046E-02	9.9679E-02	7.1779E-02
correlation matrix continued									
-7.3890E-03	0.8495	-0.7398	-1.8865E-03	7.9730E-02	-1.0534E-02	-0.8950			
-3.6593E-02	-0.3584	0.3513	1.5249E-02	-6.6794E-03	2.5512E-02	0.3077			
-5.8936E-02	0.2508	-0.1844	9.9931E-02	-0.1761	-7.7285E-03	0.3143			
-0.1772	0.3549	-0.1855	0.2027	0.1282	1.4541E-02	0.2471			
-1.7379E-02	-0.1083	0.1267	3.9620E-03	0.1390	1.5410E-02	5.3649E-02			
0.8379	-3.0534E-02	6.9764E-03	-0.1649	-0.1645	-0.1228	6.3266E-02			
-0.9867	-2.4146E-02	4.9525E-02	9.2020E-02	0.1297	1.5048E-02	-1.2098E-02			
0.9610	4.4853E-03	-3.6462E-02	-0.1219	-0.1531	-6.1179E-02	3.4046E-02			
0.4426	-7.9583E-02	4.5588E-02	-0.1388	-0.1615	-0.1716	9.9679E-02			
0.7909	-3.4649E-02	-6.2000E-03	-0.1704	-0.1802	-0.1486	7.1779E-02			
1.000	1.5982E-03	1.000	-2.3702E-02	-0.1162	-0.1033	-6.9539E-02	1.8194E-02		
1.5982E-03	-0.9629	0.9629	-0.1987	-0.2781	3.9845E-03	-0.9101			
-2.3702E-02	-0.9629	1.000	0.3785	0.5031	-3.9845E-04	0.7717			
-0.1162	-0.1987	0.3785	1.000	0.6237	2.6288E-02	9.3066E-03			
-0.1033	-0.2781	0.5031	0.6237	1.000	1.6545E-02	1.000	-9.3381E-02	1.3641E-03	1.000
-6.9539E-02	3.9845E-03	-3.9984E-04	2.9288E-02	1.6545E-02	9.3066E-03	-9.3381E-02	1.3641E-03		
1.8194E-02	-0.9101	0.7717	9.3066E-03	-9.3381E-02	1.3641E-03				

Figure 5.14. Correlation Matrix from the Doublet Input.

mean square. However, the Dryden angle of attack is 20% larger which therefore implies the Dryden overall correlation between the parameters is lower (more favorable). The same result exists for the 30 degree angle of attack flights. However, for the higher angle of attack (30 degrees) there can be no dispute that the Dryden single-surface inputs have the smallest root mean squares and standard deviations of the four inputs compared.

Flight #	Maneuver	AOA	Root Mean Square	Standard Deviation
165.3	Morelli Optimal Input Maneuver	30	0.4513	0.4505
161.1	Klein Optimal Input Maneuver *	30	0.3746	0.3742
116.8	Early Regular Doublets	30	0.3404	0.3385
165.3	Dryden Single Surface Inputs	30	0.3099	0.3084
165.2	Dryden Single Surface Inputs	25	0.3419	0.3404
160.5	Klein Optimal Input Maneuver *	20	0.3556	0.3533
116.6	Early Regular Doublets	20	0.3402	0.3393

Table 5.16. Lateral-Directional Flights Root Mean Squares & Standard Deviations.

## VI. CONCLUSIONS AND RECOMMENDATIONS

### A. CONCLUSIONS

Four different input techniques were applied in the parameter estimation flights flown for the HARV. Using the parameter estimation program, 'pEst', parameter estimates and their respective Cramer-Rao bounds were determined for each technique. Comparison analysis was completed in Chapter V, and the following conclusions are based on the completed analysis.

- (1) Automated inputs using an On Board Exciter System (OBES) produce more accurate estimations. In general, the Dryden single-surface input using the OBES produced the smallest Cramer-Rao bounds which would imply more accurate parameter estimates.
- (2) Deflecting each control surface separately as in the OBES inputs significantly decreases the correlation between the input control surfaces.
- (3) From the findings in the side force results, Morelli optimal inputs may produce more accurate estimates if the aileron input sign error is corrected.
- (4) Root mean square and standard deviation calculations, using the correlation matrices from each input technique, enhance and verify the existing conclusion that the Dryden single-surface input technique is expected to produce the most accurate parameters.

### B. RECOMMENDATIONS

Based on the results and conclusions already stated, the following recommendations are given.

- (1) Redo the Morelli optimal input technique with the correct input for the aileron control surface deflections. Then reanalyze the newly computed Cramer-Rao bounds determined from the correct inputs.
- (2) Increase the yawing excitation in the lateral-directional cases of the Dryden single-surface input technique to improve the rotational rate derivatives.

(3) Finally, further study of parameter estimates using different weight factors inside the response weighting matrix (W) for each input technique. The analysis conducted for this thesis used the same weight settings for each technique studied.

## LIST OF REFERENCES

1. Rediess, Herman A., "An Overview of Parameter Estimation Techniques and Applications in Aircraft Flight Testing", Parameter Estimation Techniques and Applications in Aircraft Flight Testing, NASA Technical Note D-7647, April 1974.
2. Morelli, Eugene A., "Practical Input Optimization for Aircraft Parameter Estimation Experiments", NASA Contractor Report 191462, May 1993.
3. Kempel, Robert, "F-18 High Alpha Research Vehicle Description", Dryden Flight Research Center Internal Document.
4. Mehra, Raman K. and Stepner, David E., "Maximum Likelihood Identification and Optimal Input Design for Identifying Aircraft Stability and Control Derivatives", NASA Contractor Report 2200, March 1973.
5. Maine, Richard E. and Iliff, Kenneth W., "Application of Parameter Estimation to Aircraft Stability and Control", NASA Reference Publication 1168, June 1986.
6. Balakrishnan, A.V., "Communication Theory", McGraw-Hill, Inc., 1968.
7. Cramer, Harald, "Mathematical Methods of Statistics", Princeton University Press, 1966.
8. Goodwin, Graham C. and Payne, Robert L., "Dynamic System Identification, Experiment Design and Data Analysis", Academic Press, 1977.
9. Murray, James E. and Maine, Richard E., "pEst Version 2.1 User's Manual", NASA Technical Memorandum 88280, September 1987.
10. Maine, Richard E. and Iliff, Kenneth W., "Identification of Dynamic Systems, Theory and Formulation", NASA Reference Publication 1138, February 1985.
11. Dixon, L.C.W., "Nonlinear Optimization", Crane, Russak & Co., 1972.
12. Polak, E., "Computational Methods in Optimization: A Unified Approach", Academic Press, 1971.
13. Rao, S.S., "Optimization, Theory and Applications", Wiley Eastern Limited, 1979.

14. Press, William H., Flannery, Brian P., Teukolsky, Saul A., and Vetterling, William T., "Numerical Recipes, The Art of Scientific Computing", Cambridge University Press, 1986.
15. Maine, Richard E. and Iliff, Kenneth W., "The Theory and Practice of Estimating the Accuracy of Dynamic Flight-Determined Coefficients", NASA Reference Publication 1077, July 1981.
16. Chen, R.T.N., "Input Design for Aircraft Parameter Identification: Using Time-Optimal Control Formulation", AGARD-CP-172, paper 13.
17. Morelli, Eugene A. and Klein, Vladislav, "Optimal Input Design for Aircraft Parameter Estimation Using Dynamic Programming Principles", AIAA Paper No. 90 2801-CP, August 1990.
18. Dreyfus, S.E., "Dynamic Programming and the Calculus of Variations", Academic Press, 1965.
19. Beyer, William H., "CRC Standard Mathematical Tables: 25th Edition", CRC Press, 1981.
20. Roskam, Jan, "Airplane Flight Dynamics and Automatic Flight Controls", Roskam Aviation and Engineering Corporation, 1979.
21. Maine, Richard E., "User's Manual for GetFdas Version 0.89", NASA Dryden Flight Research Center, 24 February 1995. (unpublished)
22. Maine, Richard E., "Manual for GetData Version 3.1: A FORTRAN Utility Program for Time History Data", NASA Technical Memorandum 88288, October 1987.

## APPENDIX A. EQUATIONS OF MOTION

Derivation of the equations of motion followed the approach used in Roskam's text "Airplane Flight Dynamics and Automatic Flight Controls," reference [20]. The equations are a full six-degree-of-freedom nonlinear set of differential equations. The equations assume the following:

- (1) fixed aircraft geometry;
- (2) constant mass characteristics; and
- (3) a flat earth with constant acceleration.

No assumption is made of symmetry. Rotating-mass and propulsion effects are not included. The 'pEst' User's Manual [Ref. 9] can be referenced for further explanation on the equations of motion.

### STATE EQUATIONS

Equations (A.1) through (A.7) are the state equations used inside 'pEst' from reference [9]:

$$\begin{aligned}\dot{\alpha} &= q - \tan \beta (p \cos \alpha + r \sin \alpha) - \frac{\bar{q} s R}{m V \cos \beta} C_L \\ &+ \frac{g R}{V \cos \beta} (\cos \theta \cos \phi \cos \alpha + \sin \theta \sin \alpha)\end{aligned}\quad (\text{A.1})$$

$$\begin{aligned}\dot{\beta} &= p \sin \alpha - r \cos \alpha + \frac{\bar{q} s R}{m V} C_Y \\ &+ \frac{g R}{V} [\cos \beta \cos \theta \sin \phi - \sin \beta (\cos \theta \cos \phi \sin \alpha - \sin \theta \cos \alpha)]\end{aligned}\quad (\text{A.2})$$

$$I_x \dot{p} - I_{xy} \dot{q} - I_{xz} \dot{r} = \bar{q} s b C_I R + [q r (I_y - I_z) + (q^2 - r^2) I_{yz} + p q I_{xz} - p r I_{xy}] / R \quad (\text{A.3})$$

$$-I_{xy} \dot{p} + I_y \dot{q} - I_{yz} \dot{r} = \bar{q} s c C_m R + [p r (I_z - I_x) + (r^2 - p^2) I_{xz} + q r I_{xy} - p q I_{yz}] / R \quad (\text{A.4})$$

$$-I_{xz} \dot{p} - I_{yz} \dot{q} + I_z \dot{r} = \bar{q} s b C_n R + [p q (I_x - I_y) + (p^2 - q^2) I_{xy} + p r I_{yz} - q r I_{xz}] / R \quad (\text{A.5})$$

$$\dot{\theta} = q \cos \phi - r \sin \phi \quad (A.6)$$

$$\dot{\phi} = p + \tan \theta (r \cos \phi + q \sin \phi) \quad (A.7)$$

where the variables and coefficients are defined as

$b$	reference span,
$c$	reference chord,
$C_L$	coefficient of lift,
$C_Y$	coefficient of lateral force,
$C_I$	coefficient of rolling moment,
$C_m$	coefficient of pitching moment,
$C_n$	coefficient of yawing moment,
$g$	gravitational acceleration,
$I_x, I_y, I_z$	moments of inertia,
$I_{xy}, I_{xz}, I_{yz}$	cross products of inertia,
$m$	mass,
$p$	roll rate,
$q$	pitch rate,
$\bar{q}$	dynamic pressure,
$r$	yaw rate,
$R$	conversion factor (57.2958),
$s$	reference area,
$V$	total velocity,
$\alpha$	angle of attack,
$\beta$	angle of sideslip,
$\theta$	pitch attitude, and
$\phi$	roll attitude.

## TOTAL FORCE AND MOMENT COEFFICIENTS

The total force and total moment coefficients, defined in the 'pEst' program from reference [9], are used in the state equations (equations (A.1) - (A.7)) to obtain the parameter estimation results in this thesis. The following total force and total moment equations, shown as equations (A.8) - (A.14), include user modifications to the generic default equations of reference [9] to account for the user desired control surface inputs defined in Section II.B.1. Coefficients on the right hand side of equations (A.9) through (A.14) are the parameters to be determined by 'pEst'. The addition of thrust vectoring is accounted for in the normal force equation (A.10), lateral force equation (A.12), pitching

moment equation (A.11), and yawing moment equation (A.14). The effects of thrust vectoring on the axial force and rolling moment are assumed to be negligible. Thrust vectoring coefficients  $C_{\deltapv}$  and  $C_{\deltayv}$  are individual parameters to determine the effects of the thrust vectoring inputs,  $\deltapv$  and  $\deltayv$ , on the longitudinal response and lateral-directional response respectively.

### 1. Longitudinal Equations

$$C_L = C_N \cos \alpha - C_A \sin \alpha \quad (A.8)$$

$$C_A = C_{A0} + C_{A\alpha} \alpha + \frac{c}{2VR} C_{Aq} q + C_{A\delta e} \delta e + C_{A\delta def} \delta def + C_{A\delta as} \delta as \quad (A.9)$$

$$C_N = C_{N0} + C_{N\alpha} \alpha + \frac{c}{2VR} C_{Nq} q + C_{N\delta e} \delta e + C_{N\delta def} \delta def + C_{N\delta as} \delta as + \frac{T}{\bar{q}s} C_{\deltapv} \deltapv \quad (A.10)$$

$$C_m = C_{m0} + C_{m\alpha} \alpha + \frac{c}{2VR} C_{mq} q + C_{m\delta e} \delta e + C_{m\delta def} \delta def + C_{m\delta as} \delta as - \frac{Tl}{\bar{q}sc} C_{\deltapv} \deltapv \quad (A.11)$$

### 2. Lateral-Directional Equations

$$C_Y = C_{Y0} + C_{Y\beta} \beta + \frac{b}{2VR} (C_{Yp} p + C_{Yr} r) + C_{Y\delta a} \delta a + C_{Y\delta r} \delta r + C_{Y\delta h} \delta h - \frac{T}{\bar{q}s} C_{\deltayv} \deltayv \quad (A.12)$$

$$C_l = C_{l0} + C_{l\beta} \beta + \frac{b}{2VR} (C_{lp} p + C_{lr} r) + C_{l\delta a} \delta a + C_{l\delta r} \delta r + C_{l\delta h} \delta h \quad (A.13)$$

$$C_n = C_{n0} + C_{n\beta} \beta + \frac{b}{2VR} (C_{np} p + C_{nr} r) + C_{n\delta a} \delta a + C_{n\delta r} \delta r + C_{n\delta h} \delta h + \frac{Tl}{\bar{q}sb} C_{\deltayv} \deltayv \quad (A.14)$$

where the variables and parameters are defined as

$C_A$	coefficient of axial force,
$C_N$	coefficient of normal force,
$\delta a$	aileron deflection,
$\delta as$	simultaneous aileron deflection,
$\delta e$	elevator deflection,
$\delta h$	differential horizontal tail deflection,
$\delta pv$	thrust vectoring pitch vanes deflection,
$\delta r$	rudder deflection,
$\delta def$	trailing edge flaps deflection,

$\delta_{YV}$	thrust vectoring yaw vanes deflection,
$C_{A_0}, C_{A_\alpha}, C_{A_q}, C_{A_{\delta\epsilon}},$ $C_{A_{\delta\text{def}}}, C_{A_{\delta\text{as}}}$	axial force parameters,
$C_{N_0}, C_{N_\alpha}, C_{N_q}, C_{N_{\delta\epsilon}},$ $C_{N_{\delta\text{def}}}, C_{N_{\delta\text{as}}}$	normal force parameters,
$C_{Y_0}, C_{Y_\beta}, C_{Y_p}, C_{Y_r},$ $C_{Y_{\delta\alpha}}, C_{Y_{\delta\beta}}, C_{Y_{\delta\gamma}}$	lateral force parameters,
$C_{l_0}, C_{l_\beta}, C_{l_p}, C_{l_r},$ $C_{l_{\delta\alpha}}, C_{l_{\delta\beta}}, C_{l_{\delta\gamma}}$	rolling moment parameters,
$C_{m_0}, C_{m_\alpha}, C_{m_q}, C_{m_{\delta\epsilon}},$ $C_{m_{\delta\text{def}}}, C_{m_{\delta\text{as}}}$	pitching moment parameters,
$C_{n_0}, C_{n_\beta}, C_{n_p}, C_{n_r},$ $C_{n_{\delta\alpha}}, C_{n_{\delta\beta}}, C_{n_{\delta\gamma}}$	yawing moment parameters, and
$C_{\delta pV}, C_{\delta YV}$	thrust vectoring parameters.

All the parameters are defined in the following section.

## PARAMETERS / STABILITY & CONTROL DERIVATIVES

The ‘pEst’ program defines stability and control derivatives as parameters. Derivatives symbolize a change in an aerodynamic force or moment coefficient induced by a change in a state or control surface input. All parameters inside ‘pEst’ are nondimensionalized. Nondimensional parameters are not affected by changes in dynamic pressure, and take into consideration aircraft size, speed and surrounding air density. Rotational rate ( $p, q, r$ ) derivatives have units of inverse radians, and angle of attack ( $\alpha$ ), sideslip angle ( $\beta$ ), and control derivatives have units of inverse degrees. The derivatives are divided into longitudinal derivatives and lateral-directional derivatives. Table A.1 is a list of the longitudinal derivatives and Table A.2 is a list of the lateral-directional derivatives estimated in this thesis. A change in the force or moment listed across the top of the table is induced by a change in the state or control listed on the left of the table. Example:  $C_{A_\alpha}$  is the derivative for a change in the axial force induced by a

change in the angle-of-attack. All the derivatives except the aerodynamic bias coefficients listed in Table A.1 and Table A.2 can be interpreted by following the approach used in the example for  $C_{A_\alpha}$ . The bias coefficients are constants that exist in the force or moment when all the states and control inputs are zero.

State or Control	Force or Moment		
	Axial Force	Normal Force	Pitching Moment
Aerodynamic Bias	$C_{A_0}$	$C_{N_0}$	$C_{m_0}$
Angle of Attack	$C_{A_\alpha}$	$C_{N_\alpha}$	$C_{m_\alpha}$
Pitch Rate	$C_{A_q}$	$C_{N_q}$	$C_{m_q}$
Elevator Deflection	$C_{A_{\delta e}}$	$C_{N_{\delta e}}$	$C_{m_{\delta e}}$
Trailing Edge Flap Deflection	$C_{A_{\delta ef}}$	$C_{N_{\delta ef}}$	$C_{m_{\delta ef}}$
Simultaneous Aileron Deflection	$C_{A_{\delta as}}$	$C_{N_{\delta as}}$	$C_{m_{\delta as}}$
Thrust Vectoring Pitch Vane Deflection		$C_{\delta p v}$	$C_{\delta p v}$

Table A.1. Longitudinal Stability & Control Derivatives.

State or Control	Force or Moment		
	Lateral Force	Rolling Moment	Yawing Moment
Aerodynamic Bias	$C_{Y_0}$	$C_{l_0}$	$C_{n_0}$
Angle of Sideslip	$C_{Y_\beta}$	$C_{l_\beta}$	$C_{n_\beta}$
Roll Rate	$C_{Y_p}$	$C_{l_p}$	$C_{n_p}$
Yaw Rate	$C_{Y_r}$	$C_{l_r}$	$C_{n_r}$
Aileron Deflection	$C_{Y_{\delta a}}$	$C_{l_{\delta a}}$	$C_{n_{\delta a}}$
Rudder Deflection	$C_{Y_{\delta r}}$	$C_{l_{\delta r}}$	$C_{n_{\delta r}}$
Differential Horizontal Tail Deflection	$C_{Y_{\delta h}}$	$C_{l_{\delta h}}$	$C_{n_{\delta h}}$
Thrust Vectoring Yaw Vane Deflection	$C_{\delta yv}$		$C_{\delta yv}$

Table A.2. Lateral-Directional Stability & Control Derivatives.

## APPENDIX B. COMPUTER SOFTWARE

### GetFdas

‘GetFdas’ replaced ‘GetData’ as the flight data access system at NASA Dryden but did not replace all of the options available on ‘GetData’. Therefore, both data systems are needed for the signals desired in this thesis. The following is the file used to retrieve time history data from one of the HARV flights. *Italics* is used to indicate commands. For more information on the commands of ‘GetFdas’ see reference [21].

```
project f186
flight flt0165
parameter pcc qc rmc aar aap aay pdot qdot rdot &
phic thetac psiangc udot vdot wdot vtrue1 qbar hp minf &
axcgc aycgc azcgc alpha beta dep dap drp dhl drl dal dtfl dlfli dlflo &
dhr drr dar dtfr dlfri dlfro ax10c ax11c ax12c bx10c bx11c bx12c &
dsb wt cg xcg ycg zcg ix iy iz ixz iexnlrc iexnlle iexnhrc iexnhlc &
ax24c ax25c av59c av60c av28c av29c icarrc icarriic av01c av02c zrengm &
ax32f ax21 ax22
write meas165.3 cmp3
time 09:50:30:0-09:50:45:0 dt=.05
quit
```

## GetData

The following is the listed file that was used to generate the measured time history data files used inside ‘pEst’. *Italics* is used to indicate a command. Note how some of the signals are generated by using arithmetical operators on other signals. An example is the first comment line which shows:

```
dyv = .25*ax11c-.25*ax12c+.25*bx12c-.25*bx11c
```

where dyv is the thrust vectoring yaw vane deflection control input, ax11c is vane 2, ax12c is vane 3, bx11c is vane 5, and bx12c is vane 6 (see Figure 2.3 for vane position). A list and definition of all the time history signals available from the HARV flights follows this file. For more information on the commands of ‘GetData’ see reference [22].

```
-- dyv=.25*ax11c-.25*ax12c+.25*bx12c-.25*bx11c &
-- dpvl=.5*ax10c-.25*ax11c-.25*ax12c &
-- dpvr=.5*bx10c-.25*bx11c-.25*bx12c &
-- dpv='dpvl'+dpvr' &
-- obes = ax32f
signals &
p='pcc', q='qc', r='rmc' &
pdota='aar', qdota='aap', rdota='aay' &
pdot, qdot, rdot &
phi = 'phic', theta = 'thetac', psi='psiangc' &
udot, vdot, wdot &
v='vtrue1' &
qbar, alt = 'hp', mach= 'minf' &
ax = 'axcgc', ay='aycgc', an= 'azcgc' &
alpha, beta &
dep,dap,drp &
dhl,drl,dal,dtfl,dlfli,dlflo &
dhr,drr,dar,dtfr,dlfri,dlfro &
ax10c,ax11c,ax12c,bx10c,bx11c,bx12c &
obes = ax32f &
De = .5*'dhl'+.5*'dhr' &
Dtef = .5*'dtfl'+.5*'dtfr' &
Dlef = .25*'dlfli'+.25*'dlflo'+.25*'dlfri'+.25*'dlfro' &
Das= .5*'dal'+.5*'dar' &
dpvl=.5*ax10c-.25*ax11c-.25*ax12c' &
dpvr=.5*bx10c-.25*bx11c-.25*bx12c' &
dSB = 'dsb' &
Da = .5*'dal'-.5*'dar' &
```

```

Dr = .5*'drl'+.5*'drr' &
Dh = .5*'dhl'- .5*'dhr' &
Dyv=.25*'ax11c'-.25*'ax12c'+.25*'bx12c'- .25*'bx11c' &
wt,           cg &
xcg,          ycg,          zcg &
ix,           iy,           iz,           ixz &
erpmrf = 'iexnlrc', erpmrf = 'iexnlc' &
erpmrc = 'iexnhrc', erpmrc = 'iexnhlc' &
plal = ax24c, plar = ax25c &
a8l = av59c, a8r = av60c &
nprl = av28c, nprr = av29c &
fgl = icarrc &
fgr = icarric &
Thrust = icarrc+icarric &
vane1 = 11.64*ax10c-10. &
vane2 = 11.64*ax11c-10. &
vane3 = 11.64*ax12c-10. &
vane4 = 11.64*bx10c-10. &
vane5 = 11.64*bx11c-10. &
vane6 = 11.64*bx12c-10. &
pcom = av01c &
ycom = av02c &
rfcs = zrengm
write temp.file cmp3
copy
write
read temp.file
sigs +del pcc, qc, rmc &
aar, aap, aay &
phic, thetac, psiangc &
vtrue1 &
hp, minf &
axcgc, aycgc, azcgc &
dsb &
iexnlrc, iexnlc &
iexnhrc, iexnhlc &
ax21c, ax22c, ax24c, ax25c &
av59c, av60c &
av28c, av29c &
icarrc, icarric, av01c, av02c, zrengm

sigs +all
sigs +add Dpv='dpvl'+'dpvr'

```

## CURRENT FILE

The *current* file is one of the files ‘pEst’ needs to begin parameter estimation. This file is a status file used to start the iterative ‘pEst’ process and store the computed final results when the solution converges. The file lists all the variable names used inside ‘pEst’ and values associated with each variable. The variables used in ‘pEst’ are grouped into one of the following categories: parameters (*param*), constant (*const*), *flag*, *state*, *output*, *input*, and *extra*. The constants (*const*), inputs (*input*), and extras (*extra*) are all listed with their name and value. Flags (*flag*) are listed with their name and status. The final three variables have multiple column entries as follows:

Parameters (*param*) have six columns each of which signify

- (1) parameter name,
- (2) initial value (entered by user),
- (3) current value (computed by ‘pEst’),
- (4) status of parameter (F = do not estimate the param, T = estimate the param),
- (5) Cramer-Rao bound, and
- (6) change in estimated parameter value from the prior iterate.

Only five of the columns are used for storing values. This is due to the fact that either a Cramer-Rao bound (5) or a change from the prior iterate (6) can be stored but not both.

States (*state*) have three columns which denote

- (1) state name,
- (2) status of state (F = inactive, T = active), and
- (3) integration limit (maximum number of integrations ‘pEst’ will perform).

Outputs (*output*) have four columns which express

- (1) output name,
- (2) current value,
- (3) status of output (F = do not determine the output, T = determine the output),
- (4) output weight factor (mentioned in Section II.B.3).

Included in the *current* file are 8 options at the bottom of the file. Three of these options which have been mentioned in the thesis are the minimization technique (*min*), convergence tolerance (*bound*) and message level (*msgLevel*). Minimization techniques and convergence tolerance are discussed in Section II.C, but the message level setting is

how the correlation matrix is calculated. The default value for the message level is 50, however, if the value of 57 is used, the final information listed on the screen when a solution converges will be a correlation matrix for the determined parameters. For further information on the reamining options in a *current* file see reference [9].

The *current* file from Morelli's lateral-directional input flight 0165 is listed below. The lateral-directional parameters that are being estimated all have final values and Cramer-Rao bounds stored. No longitudinal parameters are active. The states which are active are  $\beta$ ,  $p$ ,  $r$ , and  $\phi$ . The active output responses are  $\beta$ ,  $p$ ,  $r$ ,  $\phi$ , and  $a_y$  with the corresponding weight factors of 3, 1, 3, 1, and 30 respectively. At the bottom of the file, the minimization method (*min*) set is Levenberg-Marquardt method; the convergence tolerance (*bound*) is 0.0001; and the message level (*msgLevel*) is 57.

```

version pest-current 2.3 19 May 95 14:41:05
title
param cNorm0 0. 0. F 0. 0.
param cNorma 0.1000000000 0.1000000000 F 0. 0.
param cNorma2 0. 0. F 0. 0.
param cNormAdot 0. 0. F 0. 0.
param cNormq 0. 0. F 0. 0.
param cNormde 0.5000000000E-020.5000000000E-02 F 0. 0.
param cNormde2 0. 0. F 0. 0.
param cNormdtef 0. 0. F 0. 0.
param cNormdlef 0. 0. F 0. 0.
param cNormdas 0. 0. F 0. 0.
param cdpv 0. 0. F 0. 0.
param cm0 0. 0. F 0. 0.
param cma -.1000000000E-01-.1000000000E-01 F 0. 0.
param cma2 0. 0. F 0. 0.
param cmAdot 0. 0. F 0. 0.
param cmq -20.00000000 -20.00000000 F 0. 0.
param cmde -.2000000000E-01-.2000000000E-01 F 0. 0.
param cmde2 0. 0. F 0. 0.
param cmdtef 0. 0. F 0. 0.
param cmdlef 0. 0. F 0. 0.
param cmddas 0. 0. F 0. 0.
param ca0 0. 0. F 0. 0.
param caa 0. 0. F 0. 0.
param caa2 0. 0. F 0. 0.
param caAdot 0. 0. F 0. 0.
param caq 0. 0. F 0. 0.
param cade 0. 0. F 0. 0.

```

param	cade2	0.	0.	F	0.	0.
param	cadtef	0.	0.	F	0.	0.
param	cadlef	0.	0.	F	0.	0.
param	cadas	0.	0.	F	0.	0.
param	v0	0.	0.	F	0.	0.
param	alpha0	0.	0.	F	0.	0.
param	q0	0.	0.	F	0.	0.
param	theta0	0.	0.	F	0.	0.
param	vBias	0.	0.	F	0.	0.
param	alphaBias	0.	0.	F	0.	0.
param	qBias	0.	0.	F	0.	0.
param	thetaBias	0.	0.	F	0.	0.
param	anBias	0.	0.	F	0.	0.
param	axBias	0.	0.	F	0.	0.
param	qdotBias	0.	0.	F	0.	0.
param	ka	1.000000000	1.000000000	F	0.	0.
param	xa	0.	38.1540000	F	0.	0.
param	ya	0.	-2900000000E-01	F	0.	0.
param	za	0.	8.625000000	F	0.	0.
param	xan	0.	31.25400000	F	0.	0.
param	yan	0.	-2570000000	F	0.	0.
param	zan	0.	6.866000000	F	0.	0.
param	xax	0.	31.40830000	F	0.	0.
param	yax	0.	-1200000000	F	0.	0.
param	zax	0.	6.937000000	F	0.	0.
param	xv	0.	0.	F	0.	0.
param	yv	0.	0.	F	0.	0.
param	zv	0.	0.	F	0.	0.
param	cy0	0.	0.2410703836E-01	T0.4442360235E-02	0.	0.
param	cyb	0.	-1000000000E-01	-1.1077728552E-01	T0.2373714384E-02	0.
param	cyb3	0.	0.	F	0.	0.
param	cyBdot	0.	0.	F	0.	0.
param	cyp	0.	0.	F	0.	0.
param	cyr	0.	0.	F	0.	0.
param	cyda	0.	0.1071487091E-02	T0.9286630925E-03	0.	0.
param	cydr	0.	0.1000000000E-020	0.2263515833E-02	T0.8164648425E-03	0.
param	cydh	0.	-1704861987E-01	T0.4512779227E-02	0.	0.
param	cdyv	0.	0.1144260542	T0.3505295696E-02	0.	0.
param	cl0	0.	0.1745970396E-02	T0.7712230077E-04	0.	0.
param	clb	0.	-5000000000E-03	-3.3925895284E-02	T0.1379716351E-03	0.
param	clb3	0.	0.	F	0.	0.
param	clBdot	0.	0.	F	0.	0.
param	clp	0.	-4000000000	-1.922954035	T0.1057070890	0.
param	clr	0.	0.1000000000	1.212002858	T0.1013771934	0.
param	clda	0.	0.1000000000E-020	0.1924929127E-02	T0.6899108398E-04	0.
param	cldr	0.	0.	0.2198417997E-04	T0.3082761152E-04	0.
param	cldh	0.	0.	-6332569780E-02	T0.4661939590E-03	0.
param	cn0	0.	0.	-2489798458E-03	T0.6609757153E-04	0.
param	cnb	0.	0.1000000000E-020	0.1010098092E-02	T0.2331640454E-03	0.
param	cnb3	0.	0.	F	0.	0.
param	cnBdot	0.	0.	F	0.	0.

param	cnp	-.5000000000E-01	0.2729208735	T0.1825492898	0.
param	cnr	-.1000000000	0.2479798146E-01	T0.1250727317	0.
param	cnda	0.	-.7788211063E-03	T0.1177913933E-03	0.
param	cndr	0.	-.9502179372E-03	T0.3096009139E-04	0.
param	cndh	0.	0.4322383884E-03	T0.7725628457E-03	0.
param	beta0	0.	0.	F	0.
param	p0	0.	0.	F	0.
param	r0	0.	0.	F	0.
param	phi0	0.	0.	F	0.
param	betaBias	0.	0.	F	0.
param	pBias	0.	0.2556021392	T0.3922314561E-01	0.
param	rBias	0.	0.	F	0.
param	phiBias	0.	0.	F	0.
param	ayBias	0.	-.1849230623E-01	T0.2534586545E-02	0.
param	pdotBias	0.	0.	F	0.
param	rdotBias	0.	0.	F	0.
param	kb	1.000000000	1.000000000	F	0.
param	xb	0.	38.15400000	F	0.
param	yb	0.	-.2900000000E-01	F	0.
param	zb	0.	8.625000000	F	0.
param	xay	0.	31.42900000	F	0.
param	yay	0.	0.7670000000E-01	F	0.
param	zay	0.	6.820500000	F	0.
param	gAlpha	0.	0.	F	0.
param	gQ	0.	0.	F	0.
param	gBeta	0.	0.	F	0.
param	gP	0.	0.	F	0.
param	gR	0.	0.	F	0.
const	avg_qbar	47.02747530			
const	avg_mach	0.2666246943			
const	avg_v	284.2670250			
const	avg_alpha	29.72887257			
const	avg_theta	18.58412101			
const	avg_beta	0.5474186908			
const	avg_phi	0.1565727122			
const	mass	1082.620000			
const	ix	22930.00000			
const	iy	174370.0000			
const	iz	189500.0000			
const	ixy	0.			
const	ixz	-2100.000000			
const	iyz	0.			
const	area	400.000000			
const	span	37.42000000			
const	chord	11.52300000			
const	xcg	38.37900000			
const	ycg	0.7000000000E-01			
const	zcg	8.567000000			

flag	use_avg_qbar	F
flag	use_avg_mach	F
flag	use_avg_v	T
flag	use_avg_alpha	F
flag	use_avg_theta	F
flag	use_avg_beta	F
flag	use_avg_phi	F
state	v	F 1000000.000
state	alpha	F 10000.00000
state	q	F 10000.00000
state	theta	F 10000.00000
state	beta	T 10000.00000
state	p	T 10000.00000
state	r	T 10000.00000
state	phi	T 10000.00000
output	v	284.2670250 F 3.000000000
output	alpha	29.72887257 F 3.000000000
output	q	0.1307874338 F 8.000000000
output	theta	18.58412101 F 5.000000000
output	an	0.9638850611 F 15.000000000
output	ax	0.3519499773 F 15.000000000
output	qdot	0.2724290153E-02 F 0.
output	beta	0.5474186908 T 3.000000000
output	p	-.3746172042E-01 T 1.000000000
output	r	0.1000962146E-01 T 3.000000000
output	phi	0.1565727122 T 1.000000000
output	ay	-.6316484124E-02 T 30.000000000
output	pdot	0.1749462342 F 0.
output	rdot	-.1203947057E-01 F 0.
input	de	-4.224211654
input	dtef	0.6636709350E-01
input	dlef	31.00014934
input	das	1.130543045
input	dpv	0.6881730417E-02
input	da	-.7097900126
input	dr	1.088417355
input	dh	-.1749955382
input	dyv	0.1595552986E-03
extra	qbar	47.02747530
extra	mach	0.2666246943
extra	thrust	10972.55911
extra	alt	20779.52061
maneuver	09.50.50.000	09.51.13.000
window	09.50.50.000	09.51.13.000

```
option integ      Runge-Kutta-4
option min       Lev-Marq      T
option line       0.           0.
option gradMeth   single-sided
option gradDelt   0.1000000000E-06
option bound      0.1000000000E-03
option msgLevel    57
option apFact      0.
```



## **APPENDIX C. ROOT MEAN SQUARE & STANDARD DEVIATION**

The root mean square and standard deviation of the correlation matrix were computed using a simple MATLAB macro file and formulas retrieved from reference [19]. Once the correlation matrix was computed by 'pEst', the matrix was copied into the macro file so that the root mean square and standard deviation could be determined. A sample program is shown here.



## INITIAL DISTRIBUTION LIST

1. Defense Technical Information Center ..... 2  
Cameron Station  
Alexandria, Virginia 22304-6145
2. Library, Code 52 ..... 2  
Naval Postgraduate School  
Monterey, California 93943-5101
3. Chairman, Code AA ..... 1  
Department of Aeronautics and Astronautics  
Naval Postgraduate School  
Monterey, California 93943-5000
4. Professor Richard M. Howard, Code AA/Ho ..... 2  
Department of Aeronautics and Astronautics  
Naval Postgraduate School  
Monterey, California 93943-5000
5. Mr. Albion H. Bowers ..... 2  
Mail Stop D-2033  
NASA Dryden Flight Research Center  
P.O. Box 273  
Edwards, California 93523
6. Mr. Brent R. Cobleigh ..... 1  
Mail Stop D-2033  
NASA Dryden Flight Research Center  
P.O. Box 273  
Edwards, California 93523
7. LT Russell J. Gates ..... 1  
1166 Hickory Nut Dr.  
California, Maryland 20619